

# **Electric Thermal Energy Storage based on Packed Beds for Renewable Energy Integration**

Vom Promotionsausschuss der  
Technischen Universität Hamburg  
zur Erlangung des akademischen Grades

**Doktor-Ingenieur**

genehmigte Dissertation

von

**Michael von der Heyde**

aus Kiel

2022

1. Gutachter: Prof. Dr.-Ing. Gerhard Schmitz  
2. Gutachter: Prof. Dr.-Ing. Stefan Will  
Prüfungsvorsitzender: Prof. Dr.-Ing. Alfons Kather

Tag der mündlichen Prüfung: 26. 01. 2022

DOI: <https://doi.org/10.15480/882.4165>  
URN: <urn:nbn:de:gbv:830-882.0172904>

*The text is licensed under the Creative Commons Attribution 4.0 (CC BY 4.0) license. This means that it may be reproduced, distributed and made publicly available, even commercially, provided that the author, the source of the text and the above-mentioned license are always mentioned. The exact wording of the license can be accessed at <https://creativecommons.org/licenses/by/4.0/legalcode>.*

# Acknowledgments

This thesis is based on scientific work at the Institute of Engineering Thermodynamics at Hamburg University of Technology for the joint research project Future Energy Solution in collaboration with Siemens Gamesa Renewable Energy and Hamburg Energie GmbH. The project was funded by Germany's Sixth Energy Research Program, which is gratefully acknowledged. Being part of the project was a strong enrichment to me and I highly appreciate the interesting insights and discussions, as well as the support of all project partners by providing background information and measured data.

I am very grateful for the support, trust and encouragement of my advisor Prof. Dr.-Ing. Gerhard Schmitz, who granted every freedom at daily work to dive into the research area with my own focus and established excellent working conditions at the institute. I also want to thank Prof. Dr.-Ing Stefan Will for being the second reviewer of the thesis and Prof. Dr.-Ing. Alfons Kather for taking over the chairmanship of the examination board.

All colleagues at the institute contributed to a great working atmosphere and I appreciate the support, interesting discussions and wonderful times we spend together at breaks. I especially want to thank Lisa Andresen for the initial work on the project and for motivating me to join it.

Many students have contributed to the research project through their thesis or as research assistant. Their commitment, ideas and feedback is highly appreciated.

Last but not least I want to thank my wife Jasmin for the strong backing during the thesis writing and for making our life as it is, as well as our two sons, Enno and Jonas, who motivate us everyday with their happiness and confidence in the future.

Hamburg, February 22, 2022



# Summary

Energy storage allows to balance electricity generation from wind and solar energy with the energy demand over time. The discharged energy can substitute fossil fuel combustion in times of low wind or solar energy availability in order to reduce CO<sub>2</sub>-emissions. But energy storage is subject to cost, energy losses and environmental footprint. A mix of various storage technologies according to their capital cost and efficiency as well as an enhanced integration of energy sectors is likely to be part of the optimal solution to wind and solar energy integration.

Carnot Batteries convert electricity to heat at charge, store thermal energy and reconvert heat to electricity at discharge upon demand. A particular Carnot Battery concept named Electric Thermal Energy Storage is investigated in this work. It uses electric heating of air at charge, a packed bed of crushed rock for low-cost high-temperature thermal energy storage and a heat recovery steam generator to provide steam for a turbine or other consumers at discharge.

This work is based on numerical simulation of the storage concept on three scales, which are **1.** dynamic system simulation in *Modelica* for the energy-based evaluation of the storage concept, **2.** three-dimensional CFD simulation to further investigate the heat and mass transport in the packed-bed storage and **3.** particle-resolved CFD simulation to derive correlations for the heat and mass transfer on the particle scale. Measured data from a 130 MWh<sub>th</sub> demonstration plant in Hamburg, Germany, has been used for validation of the models.

The energy-based efficiency of steam supply upon demand according to simulation results is 78 to 96 %, depending on the way of system integration, operational schedule and design. It has to be multiplied to the water-steam cycle efficiency to complement an electric energy storage round-trip efficiency. As the packed-bed storage outlet temperatures on the hot and cold side must be kept in a limited range and a thermocline occupies a share of the packed-bed volume, the storage has a limited depth of charge and discharge. According to simulation results, the ratio of usable to nominal storage capacity is at 63 to 83 %.



# Contents

Glossary	vii
List of Figures	xiii
List of Tables	xv
<b>1 Introduction</b>	<b>1</b>
<b>2 Background</b>	<b>7</b>
2.1 First and Second Law of Thermodynamics . . . . .	7
2.2 Quantities to Evaluate Energy Storage Systems . . . . .	9
2.3 Review on Electric Energy Storage . . . . .	15
2.4 Carnot Batteries . . . . .	18
2.5 Review on High-Temperature Thermal Energy Storage . . . . .	22
2.6 Packed-Bed Thermal Energy Storage . . . . .	24
2.6.1 Design . . . . .	27
2.6.2 Modeling . . . . .	30
2.7 System Simulation with <i>Modelica</i> . . . . .	45
<b>3 Electric Thermal Energy Storage</b>	<b>47</b>
3.1 System Layout . . . . .	47
3.2 Operation . . . . .	49
3.3 Applications . . . . .	51
3.4 State of the Art . . . . .	53
3.5 Efficiency Definition . . . . .	54
3.6 Usable Capacity Ratio . . . . .	57
3.7 Classification of Air Cycle Energy Losses . . . . .	60
<b>4 Simulation Method</b>	<b>63</b>
4.1 Overview on Multi-Scale Simulation . . . . .	63
4.2 System Simulation . . . . .	65
4.2.1 Application Case Models . . . . .	67
4.2.2 Air Cycle Model . . . . .	68

4.2.3	One-Dimensional Model of Packed-Bed Storage . . . . .	72
4.2.4	Further Air Cycle Component Models . . . . .	78
4.3	Porous-Media CFD Simulation . . . . .	83
4.3.1	Modeling of Porous Medium . . . . .	84
4.3.2	Initial and Boundary Conditions . . . . .	85
4.3.3	Temporal and Spatial Discretization . . . . .	87
4.3.4	Post Processing . . . . .	89
4.4	Particle-Resolved CFD Simulation . . . . .	89
4.4.1	Generation of Packed Bed Surface . . . . .	92
4.4.2	Modeling of Fluid Flow and Heat Transfer . . . . .	95
4.4.3	Boundary Conditions . . . . .	97
4.4.4	Spatial Discretization . . . . .	99
4.4.5	Post Processing . . . . .	100
<b>5</b>	<b>Model Validation</b>	<b>107</b>
5.1	Particle-Resolved CFD Simulation . . . . .	108
5.2	One- and Three-Dimensional Packed-Bed Storage Models . . . . .	112
5.3	Heat Recovery Steam Generator and Fan Models . . . . .	118
<b>6</b>	<b>Results</b>	<b>121</b>
6.1	Definition of Test Cases . . . . .	121
6.2	Packed-Bed Properties at Horizontal Flow . . . . .	126
6.3	Selection of Particle Size and Storage Aspect Ratio . . . . .	131
6.4	Selection of Storage Outlet Temperature Deviation Tolerance . . . . .	134
6.5	Selection of Packed-Bed Storage Thermal Insulation Thickness . . . . .	136
6.6	Comparison of One- and Three-Dimensional Storage Models . . . . .	137
6.7	Comparison of Air Cycle Performance for the Test Cases . . . . .	141
<b>7</b>	<b>Conclusion</b>	<b>147</b>
	<b>Bibliography</b>	<b>153</b>
	<b>Appendix</b>	<b>173</b>

# Glossary

Marked (\*) symbols possess a mass-specific variant in which the symbol is written in lowercase and the unit is extended by  $\text{kg}^{-1}$ .

## Symbols

Roman	Description	Unit
$A$	Area	$\text{m}^2$
$a$	Area per Volume	$\text{m}^2/\text{m}^3$
$B$	Constant	–
$Bi$	Biot Number	–
$C$	Cost	€
$c_e$	Cost per Energy Unit	€/MWh
$c_F$	Inertial Coefficient	–
$Co$	Courant Number	–
$c_p$	Cost per Power Unit	€/MW
$C_p$	Isobaric Specific Heat Capacity*	J/K
$C_v$	Isochoric Specific Heat Capacity*	J/K
$d_{32}$	Sauter Mean Diameter	m
$d$	Diameter	m
$d_h$	Hydraulic Diameter	m
$d_v$	Volume Equivalent Diameter	m
$E$	Energy*	J
$Eu$	Euler Number	–
$E_X$	Exergy*	J

$f$	Body Force	$\text{N/m}^3$
$F_E$	Exchange Factor	–
$F$	Force	$\text{N}$
$f$	Frequency	$1/\text{s}$
$H$	Enthalpy*	$\text{J}$
$i$	Index	–
$J$	Moment of Inertia	$\text{kg m}^2$
$K$	Permeability	$\text{m}^2$
$k$	Ratio of Thermal Conductivities	–
$m$	Mass	$\text{kg}$
$n$	Count	–
Nu	Nusselt Number	–
$p$	Pressure	$\text{Pa}$
Pr	Prandtl Number	–
$Q$	Heat	$\text{J}$
Ra	Rayleigh Number	–
Re	Reynolds Number	–
$r$	Interest Rate	–
$r$	Radius	$\text{m}$
$R$	Specific Gas Constant	$\text{J}/(\text{kg K})$
$S$	Entropy*	$\text{J/K}$
$T$	Temperature	$\text{K}$
$t$	Time	$\text{s}$
$U$	Internal Energy*	$\text{J}$
$v$	Velocity	$\text{m/s}$
$V$	Volume	$\text{m}^3$
$W$	Work	$\text{J}$
$x$	First Cartesian Coordinate (length)	$\text{m}$
$y$	Second Cartesian Coordinate (width)	$\text{m}$
$z$	Third Cartesian Coordinate (height)	$\text{m}$

<b>Greek</b>	<b>Description</b>	<b>Unit</b>
$\alpha$	Heat Transfer Coefficient	W/(m <sup>2</sup> K)
$\varepsilon$	Porosity	–
$\zeta$	Exergetic Efficiency	–
$\eta$	Efficiency	–
$\kappa$	Ratio of Specific Heats	–
$\lambda$	Thermal Conductivity	W/(m K)
$\mu$	Dynamic Viscosity	Pa s
$\rho$	Density	kg/m <sup>3</sup>
$\sigma$	Standard Deviation	–
$\tau$	Time Constant	s
$\varphi$	Usable Capacity Ratio	–
$\chi$	Aspect Ratio	–
$\psi$	Sphericity	–
$\omega$	Angular Velocity	1/s
$\varepsilon$	Emissivity	–
$\vartheta$	Temperature	°C

<b>Other</b>	<b>Description</b>	<b>Unit</b>
$ \square $	Absolute Value of $\square$	$\square$
$\bar{\square}$	Arithmetic Mean of $\square$	$\square$
$d\square$	Derivative of $\square$	$\square$
$\Delta\square$	Difference of $\square$	$\square$
$\dot{\square}$	Flow Rate of $\square$	$\square/s$
<b>I</b>	Identity Matrix	–
$\partial\square$	Partial Derivative of $\square$	$\square$
$\nabla\square$	Vector of partial derivatives of $\square$	$\square$
<b>x</b>	Cross Product	–
<b>y</b>	Vector	$\square$

# Numbers

Symbol	Description	Phys. Qtt.
$e$	Euler's number	$\approx 2.72$
$g$	Standard Gravity	$\approx 9.81 \text{ m/s}^2$
$\pi$	Pi	$\approx 3.14$
$\sigma$	Stefan-Boltzmann Constant	$\approx 5.67 \times 10^{-8} \text{ W/(m}^2 \text{ K}^4)$

# Subscripts

<b>o</b>	At Stagnant Fluid	<b>max</b>	Maximum
<b>a</b>	Annual	<b>mech</b>	Mechanical
<b>ac</b>	Air Cycle	<b>min</b>	Minimum
<b>air</b>	Air	<b>mix</b>	Mixing
<b>ap</b>	Approach Point	<b>net</b>	Net Value
<b>bed</b>	Packed Bed	<b>nom</b>	Nominal
<b>c</b>	Charge	<b>o&amp;m</b>	Operation And Maintenance
<b>cap</b>	Capital	<b>out</b>	Outlet
<b>cond</b>	Conduction	<b>p</b>	Particle
<b>contact</b>	Contact	<b>p2h</b>	Power to Heat
<b>cross</b>	Cross Direction	<b>p2p</b>	Power to Power
<b>cs</b>	Cold Side	<b>poly</b>	Polytropic
<b>d</b>	Discharge	<b>pp</b>	Pinch Point
<b>e</b>	Energy	<b>rad</b>	Radiation
<b>efc</b>	Equivalent Full Cycles	<b>ref</b>	Reference
<b>eff</b>	Effective Properties	<b>rel</b>	Relative
<b>eh</b>	Electric Heater	<b>rev</b>	Reversible
<b>el</b>	Electric	<b>s</b>	Storage
<b>env</b>	Environment	<b>sat</b>	Saturation
<b>f</b>	Fluid	<b>sby</b>	Standby
<b>fan</b>	Fan	<b>sc</b>	Steam Cycle
<b>fw</b>	Feed Water	<b>sd</b>	Self Discharge
<b>h</b>	Hold	<b>set</b>	Setpoint
<b>hs</b>	Hot Side	<b>sg</b>	Steam Generator
<b>I</b>	Series Connection	<b>steam</b>	Steam
<b>II</b>	Parallel Connection	<b>stop</b>	Stop
<b>in</b>	Inlet	<b>surf</b>	Surface
<b>irr</b>	Irreversible	<b>th</b>	Thermal
<b>loss</b>	Loss	<b>w</b>	Wall

# Abbreviations

<b>Notation</b>	<b>Description</b>
CAES	Compressed Air Energy Storage
CFD	Computational Fluid Dynamics
COP	Coefficient of Performance
CRF	Capital Recovery Factor
CSP	Concentrated Solar Power
DEM	Discrete Element Method
EES	Electric Energy Storage
ETC	Effective Thermal Conductivity
ETES	Electric Thermal Energy Storage
HRSG	Heat Recovery Steam Generator
HT	Heat Transfer
LCOS	Levelized Cost of Storage
MAE	Mean Absolute Error
MEAS	Measurement
P <sub>2</sub> H	Power-to-Heat
P <sub>2</sub> P	Power-to-Power
PD	Pressure Drop
PHPES	Power Heat Power Energy Storage
PTES	Pumped Thermal Energy Storage
PV	Photovoltaics
RCV	Representative Computational Volume
SDR	Self Discharge Rate
SIM	Simulation
SOC	State of Charge
TES	Thermal Energy Storage
VRE	Variable Renewable Electricity
WEC	Wind Energy Converter

# List of Figures

2.1	Energy Flow Chart for a General Energy Storage System . . .	10
2.2	Comparison of PHPES and PTES General Concepts . . . . .	19
2.3	Heat Pump and Heat Engine Efficiency for PTES . . . . .	21
2.4	Illustration of Packed-Bed TES . . . . .	24
2.5	Flow Directions in Packed-Bed TES . . . . .	28
2.6	Packed-Bed Aspect Ratio Examples . . . . .	29
2.7	Modes of Heat Transport in Packed Beds . . . . .	37
2.8	ETC Model According to Krischer . . . . .	43
3.1	Flow Chart for ETES Concept . . . . .	48
3.2	Characteristic Packed-Bed Temperature Distribution . . . . .	50
3.3	Overview on Application Cases for ETES . . . . .	52
3.4	ETES demonstration plant in Hamburg-Altenwerder, Germany	54
3.5	Illustration of Usable Capacity Ratio . . . . .	59
4.1	Overview on Multi-Scale Workflow . . . . .	64
4.2	<i>Modelica</i> Diagram: ETES System Integration . . . . .	68
4.3	<i>Modelica</i> Diagram: Air Cycle . . . . .	70
4.4	<i>Modelica</i> Diagram: State Graph Controller . . . . .	72
4.5	<i>Modelica</i> Diagram: Packed-Bed Storage . . . . .	72
4.6	Mesh Independence Study for One-Dimensional Model . . . .	75
4.7	Heat Recovery Steam Generator Temperature Profile . . . . .	81
4.8	Boundary Conditions for Porous-Media CFD . . . . .	86
4.9	Static Pressure Profile at Hot and Cold Side Boundary . . . .	87
4.10	Mesh Independence Study for Porous-Media CFD . . . . .	88
4.11	Overview on DEM-CFD Workflow . . . . .	90
4.12	Trend of Packed-Bed Porosity with Particle Injection Velocity .	91
4.13	Sensitivity of Porosity on Number of Available Particle Shapes	91
4.14	Sensitivity of Pressure Gradient on RCV Size . . . . .	91
4.15	Velocity of Particles at Packing Process . . . . .	94
4.16	Multi-Sphere Approximated Particle Shape . . . . .	94
4.17	Particle Size Distribution Used at Validation . . . . .	95

4.18	Variation of Porosity with Size Distribution Width . . . . .	95
4.19	Overview on Particle-Resolved CFD Boundary Conditions . . . . .	98
4.20	Mesh Independence Study for Particle-Resolved CFD . . . . .	101
4.21	Dispersion of Results for Repeated Simulation . . . . .	105
5.1	Validation of DEM-CFD Workflow: Monodisperse Spheres . . . . .	109
5.2	Validation of DEM-CFD Workflow: Crushed Rock . . . . .	110
5.3	Pictures of Packed-Bed Storage Units used for Validation . . . . .	112
5.4	Validation of Packed-Bed Models: Test Site . . . . .	114
5.5	Validation of Packed-Bed Models: Demo Plant Charge . . . . .	115
5.6	Validation of Packed-Bed Models: Demo Plant Hold . . . . .	117
5.7	Comparison of HRSG Model with Manufacturer’s Specification . . . . .	118
5.8	Comparison of Fan Model with Manufacturer’s Specification . . . . .	119
6.1	Operational Schedules Based on Wind and Solar Variability . . . . .	125
6.2	Exemplary Sections of Temperature and Velocity Field . . . . .	128
6.3	Effect of Packing Direction on Packed Bed Properties . . . . .	128
6.4	1D Model Sensitivity to Packed-Bed Correlations . . . . .	130
6.5	Variation of Particle Size and Storage Aspect Ratio . . . . .	132
6.6	Variation of Storage Outlet Temperature Deviation Tolerance . . . . .	135
6.7	Variation of Packed-Bed Storage Insulation Thickness . . . . .	136
6.8	Comparison of 1D and 3D Packed-Bed Models . . . . .	138
6.9	State of Charge at 1D-3D Comparison . . . . .	138
6.10	Packed-Bed Temperature Field on Symmetry Plane . . . . .	139
6.11	Efficiency and Usable Capacity Ratio for Test Cases . . . . .	141
6.12	Air Cycle Energy Losses for Test Cases . . . . .	143
A.1	State of Charge for Tested Operational Schedules . . . . .	175

# List of Tables

2.1	Exemplary Nominal Packed-Bed Volumetric Energy Densities	25
2.2	Operating Conditions of Rock-Bed Experiments . . . . .	26
4.1	Thermodynamic Storage Material Properties . . . . .	76
4.2	Boundary Conditions in Porous-Media CFD . . . . .	86
4.3	Computational Requirements of DEM-CFD Workflow . . . . .	93
4.4	Mechanical Storage Material Properties . . . . .	95
4.5	Mesh Parameters for Particle-Resolved CFD . . . . .	100
6.1	Operating Temperatures For Test Cases . . . . .	122
6.2	Packed-Bed Properties at Horizontal Flow . . . . .	127
A.1	Parameters of the Air-Cycle System Simulation Model . . . . .	173



# Chapter 1

## Introduction

The atmospheric CO<sub>2</sub>-concentration has grown significantly since the beginning of the industrial era [165]. A majority of experts identifies this as the main cause for the mean earth temperature increase according to the greenhouse effect, observable since the mid 20th century [141]. Further temperature increase may cause severe and unpredictable consequences for many regions of the earth. As fossil fuel combustion is the main source of CO<sub>2</sub>-emissions [141], its replacement with sustainable energy in the electricity, heat and mobility sectors as fast as possible is an essential contribution to mitigate the climate change.

Wind Energy Converter (WEC) and Photovoltaics (PV) are the fastest growing technologies for electricity generation, accounting for around 73 % of the worldwide added capacity in 2020 [89]. According to Memmler et al. [123], their specific greenhouse-gas emissions in CO<sub>2</sub>-equivalents are 67 kg/MWh for PV and 11 kg/MWh for onshore WEC, whereas Germany's hard coal power plants are at 870 kg/MWh. Furthermore, the levelized cost of electricity generation for these technologies has decreased significantly, reaching 40 to 60 €/MWh for ground-mounted large-scale PV and 40 to 80 €/MWh for onshore WEC in Germany in 2018 [99].

A major disadvantage of WEC and PV is the restricted availability of wind and solar energy in time. The variation can be seasonal, diurnal or weather-dependent and in general does not match with the variation of electricity

demand. In Germany, PV achieves 800 to 1020 and onshore WEC 1400 to 3200 full load hours per year [95]. The reader may refer to websites of system operators or network agencies such as the California Independent System Operator [32] and German Federal Network Agency [66] to see time series data of electricity generation from wind and solar energy. In consequence, electricity from WEC and PV is referred to as Variable Renewable Electricity (VRE) in the following. WEC and PV furthermore have a high land use and their rural placement increases the demand for energy transport.

The electricity generation has to meet the demand at all times, as the electricity grid itself has a low ability to store energy. The flexibility measures to balance generation and demand in the electricity sector are

1. load-following generators,
2. grid expansion to level out local imbalances,
3. demand side management and
4. Electric Energy Storage (EES).

Hot or cold reserve of fossil-fueled power plants have been the main source of flexibility in the past, as fossil fuel can be stored on site and used to generate electricity upon need. Lower VRE shares on the electricity consumption can be integrated using these load-following fossil-fueled power plants as backup, even though it has negative consequences for the economics and machinery of these plants [159]. But the availability of wind and solar energy is still restricted to times of electricity generation from PV and WEC in this case.

Further reduction of CO<sub>2</sub>-emissions through higher shares of VRE requires the other means of flexibility in the electricity grid in order to avoid curtailment of VRE at some times and fossil-fueled electricity generation at others [46, 192]. Besides grid expansion and demand side management, an increasing need for EES is projected in many scenarios, such as 11.89 to 15.72 GWh in 2030 by the International Renewable Energy Agency [87]. But EES has been rarely implemented so far, due to its high costs and energy conversion losses. The worldwide storage capacity in 2017 is estimated at 4.67 GWh [87], which is only about 0.2% of the generated electricity.

An enhanced integration of the electricity sector with the heat and mobility sectors is another flexibility measure to increase the overall share of VRE on

the final energy demand, as it enables

1. the replacement of fossil fuel with VRE as primary energy source in these sectors in order to reduce their CO<sub>2</sub> emissions and
2. an possibly more economic or efficient utilization of VRE and avoidance of VRE curtailment.

The conversion of electric power to heat can be implemented with direct electric heaters or heat pumps. The mobility sector may use VRE stored in batteries or as chemical energy carriers. But the additional electricity demand has to be transported within the electricity grid and especially has to coincide with times of VRE availability in order to reduce the overall CO<sub>2</sub>-emissions without requiring further flexibility in the electricity sector. Consequently, energy storage in the heat and mobility sector is needed as well. Advantageously, Thermal Energy Storage (TES) is normally cheaper than EES and mobile applications require energy storage anyways. Integrated energy sectors in general require a holistic view on the energy system to optimize the overall efficiency.

As the available EES technologies are either restricted by geographical prerequisites, costly per storage capacity or have a limited efficiency, there is an ongoing search for technology improvement or novel storage technologies. In this manner, Carnot Batteries, which convert electric energy to thermal energy at charge, store thermal energy and convert it back to electricity at discharge, gain significant interest recently. This interest led to an International Energy Agency technology collaboration program on Carnot Batteries in 2019 [85].

In the joint research project *Future Energy Solution* a specific Carnot Battery concept called Electric Thermal Energy Storage (ETES) is investigated. It is based on direct electric heating of air at charge, which then flows through a high-temperature packed-bed TES. A blower is used to circulate the air. Electricity can be generated at discharge from the stored heat with a conventional water-steam cycle. Optionally, the steam can also be used for other purpose. Project partners are Siemens Gamesa Renewable Energy, Hamburg Energie GmbH and Hamburg University of Technology. The project is funded by Germany's Sixth Energy Research Program. Goals of the project are

- further technology development and construction of a demonstration

plant with a thermal storage capacity of  $130 \text{ MWh}_{\text{th}}$ , which is operated up to  $750^\circ\text{C}$ ,

- operation and market integration of the demonstration plant and analysis of future economic perspectives as well as
- development of simulation tools for design optimization and evaluation of the storage technology.

## Content of This Work

The performance of the ETES technology has not been evaluated in literature yet taking into account irregular operation, as necessary for VRE and load balancing, and the transient thermal behavior of the packed-bed storage. But the time-variant temperature field inside the packed bed has a strong impact on the overall system performance. The packed-bed storage component is furthermore beyond the state of art, as

- it is operated at high temperatures,
- a horizontal air flow direction is chosen for economic reasons,
- the economically necessary scale is large,
- the application requires an irregular operation and
- it is operated in a closed cycle.

This thesis presents dynamic system simulation models in *Modelica* for the energy-based evaluation of ETES units with different designs and operational schedules. The operational schedules include electricity price and VRE generation data based schedules as well as cyclic schedules according to characteristic wind and solar energy fluctuation. All relevant energy loss mechanisms of ETES units are taken into account. The developed component models are included in version 1.4 of the open-source *TransiEnt* library [71]. Computational Fluid Dynamics (CFD) simulation of large-scale horizontal-flow packed-beds is further applied to investigate the effect of natural convection and temperature-induced density and thus flow field variations on the temperature field. The relevant packed-bed properties, such as the local pressure gradient and particle-to-fluid heat transfer coefficient, are derived from particle-resolved CFD simulation in order to reduce the dependency on costly experiments.

The packed-bed models are validated with experimental data from the demonstrator plant in Hamburg-Altenwerder and a second packed-bed storage unit in Hamburg-Bergedorf, both build by Siemens Gamesa Renewable Energy. The particle-resolved CFD simulations are validated with correlations from literature.

The structure of this thesis is as follows. In Chapter 2 the relevant background on energy storage systems, especially on Carnot Batteries and high-temperature packed-bed TES is reviewed, along with the necessary background on the modeling of packed-bed TES. Chapter 3 introduces the ETES concept. The developed system simulation and CFD models are outlined in Chapter 4, followed by their validation results in Chapter 5. In Chapter 6, simulation results for the ETES unit performance at a selection of designs and operational schedules are shown. The results are used to compare the ETES concept with other storage options in the concluding Chapter 7.



# Chapter 2

## Background

This chapter covers the relevant background for the thesis. At first the characteristic quantities to evaluate energy storage systems are defined. The state of art in EES is reviewed, in order to benchmark the ETES performance, followed by an introduction to the general concept of Carnot Batteries in order to reveal the specific ETES advantages and disadvantages compared to other Carnot Battery concepts. An overview on high-temperature TES is also given, with an emphasis on the advantages and design challenges of packed-bed TES, as the ETES concept relies on this specific TES technology. Finally, the equations needed to model packed-bed TES are introduced to provide a basis for Chapter 4 and the programming language *Modelica* is briefly described.

### 2.1 First and Second Law of Thermodynamics

As the First and Second Law of Thermodynamics are frequently used in following sections, they are introduced here. The First Law for an open and unsteady system may be written as

$$\frac{\partial E}{\partial t} = \frac{\partial E_{\text{kin}}}{\partial t} + \frac{\partial E_{\text{pot}}}{\partial t} + \frac{\partial U}{\partial t} = \dot{W} + \dot{Q} + \sum_{i=1}^n \dot{m}_i \left( \frac{h_i}{\rho_i} + \frac{1}{2} v_i^2 + g z_i \right). \quad [2.1]$$

The energy of a system is the sum of its kinetic and potential energy  $E_{\text{kin}}$  and  $E_{\text{pot}}$ , as well as its internal energy  $U$ . Internal energy may be further classified as thermal, chemical, nuclear or internal magnetic and electric field energy. Based on the first law, a system's energy can only be changed by flow of work  $\dot{W}$ , heat  $\dot{Q}$  or matter  $\dot{m}$ , which can carry enthalpy  $h$ , kinetic or potential energy, across the system boundaries.

The Second Law for the same system is

$$\frac{\partial S}{\partial t} = \frac{\dot{Q}_{\text{rev}}}{T} + \sum_{i=1}^n \dot{m}_i s_i + \dot{S}_{\text{irr}} \quad \text{with} \quad \dot{S}_{\text{irr}} \geq 0. \quad [2.2]$$

Based on the Second Law, energy may be divided into exergy and anergy. Work is exergy, its conversion to other energy forms is not restricted by the Second Law, as it does not change the system's entropy. Heat on the other hand contains an exergy and anergy part. Its conversion to work is limited by the efficiency of the Carnot Process

$$\eta_{\text{carnot}} = 1 - \frac{T_{\text{env}}}{T}, \quad [2.3]$$

depending on the temperature  $T$ , at which the heat is provided, and the temperature of the environment  $T_{\text{env}}$ . Many text books may be used for further reading, such as Schmitz [158].

## 2.2 Quantities to Evaluate Energy Storage Systems

The evaluation and comparison of different energy storage systems require consistently defined characteristic quantities. A selection, as relevant to this work, is defined on a general basis in this section to provide a solid basis for the later discussion of different technologies. More characteristic quantities may be found in the book by Sterner et al. [171].

The optimal placement, sizing and operation or dispatch of energy storage systems is subject of intense research [43]. The applied optimization techniques, such as mixed integer linear programs [78], rely on these characteristic quantities as well in order to mathematically describe energy storage systems in a simplified way.

An energy storage system is defined here as technical plant serving the purpose to shift the availability of energy in time. The operation of energy storage systems therefore consists of charge, discharge and hold modes.

According to Equation 2.1 energy can be stored as kinetic, potential or internal energy. As the required energy form to charge and discharge can be different from the energy form of storage, an energy conversion process for charge and discharge may be necessary. But, each energy conversion is subject to losses. The energy form of charge and discharge itself can be different as well, in which case the energy storage system serves the integration of energy sectors as cross-sector storage unit. Energy storage systems are either classified according to the form of stored energy, such as mechanical, chemical or thermal energy storage, or according to the form of charged or discharged energy, such as EES.

Figure 2.1 shows a schematic overview on a general energy storage system. The stored energy is denoted as  $E^s$ . Work, heat or energy transport by flow of matter are denoted as  $\dot{E}$ . Whereas the energy conversion losses  $\dot{E}_{c,loss}$  and  $\dot{E}_{d,loss}$  only occur at charge or discharge, the storage unit loss remains at hold. It is therefore referred to as self discharge loss  $\dot{E}_{sd}$ . Examples are heat transfer to the environment for thermal energy storage or friction loss in the case of flywheel energy storage. Additional work or heat may be needed to keep the operational readiness of an energy storage system, which generally does not contribute to the stored energy. This demand is referred to as standby

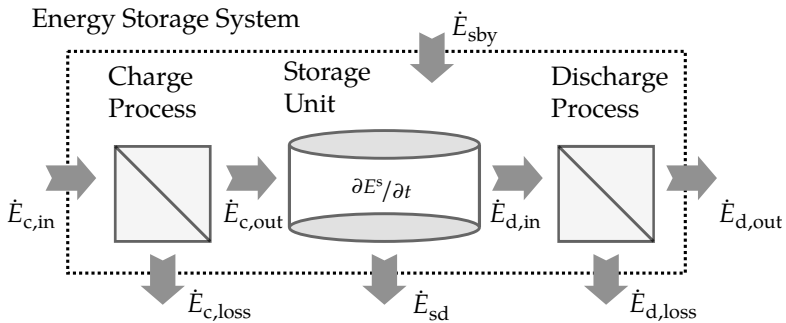


**Figure 2.1 /** Energy storage system comprising a storage unit as well as a charge and discharge process.

losses  $\dot{E}_{sby}$ . Common examples are electric energy demand for lighting, safety measures or the control system.

The efficiency of energy storage systems may either be defined

- with respect to energy flow values at the nominal operating point or
- based on integrated energy flow over an representative observation time period.

In this work an energy-based evaluation is preferred, as self-discharge and standby losses, eventual part-load operation or a dependency of the conversion losses on the state of charge are inherently taken into account. A flywheel energy storage for example may be highly efficient at charge and discharge based on nominal power values, but unusable for long hold operation due to its high self-discharge rate.

An energy-based evaluation requires the definition of an observation time period and operational schedule, which should be reported together with any results in order to allow comparison with values of other authors. A related source of error is a difference in stored energy at the beginning and end of the observation time period. It can be misleading when comparing different experimental results and should therefore be kept as small as possible. This can be done by either choosing a long observation time period to minimize it's influence or by choosing the start and end of each experiment in a very

similar state.

Instead of energy, exergy or exergy flow rates may be used to evaluate energy storage systems, which leads to the definition of an exergetic efficiency. Exergy as measure is especially useful for energy storage systems, if the energy form of discharge is work, in which case the exergetic efficiency indicates the storage system loss mechanism more precisely than energetic efficiencies [98, 178].

The variables, as shown in Figure 2.1, are used in the following to define the characteristic quantities for the evaluation of energy storage systems.

### Technical Quantities

The energy-based round-trip efficiency of a storage system is defined with the energy input and usable output as

$$\eta = \frac{E_{d,out}}{E_{c,in} + E_{sby}}. \quad [2.4]$$

The storage capacity is defined by the difference of the minimum and maximum boundary values for the stored energy  $E^s$  as

$$\Delta E^s = E_{max}^s - E_{min}^s. \quad [2.5]$$

It limits the amount of energy that can be charged or discharged in one operation cycle. But the minimum and maximum boundary values can change over time for several storage technologies, such as lithium-ion batteries or single-tank thermal energy storage. Thus, it is useful to define an invariant nominal storage capacity  $\Delta E_{nom}^s$ , which leads to a limited depth of charge or discharge for these technologies in return. For the case of packed-bed TES a possible definition of an invariant nominal thermal storage capacity can be found in Equation 3.9. A usable capacity ratio  $\varphi$  can be defined accordingly as

$$\varphi = \frac{\Delta E^s}{\Delta E_{\text{nom}}^s}. \quad [2.6]$$

The State of Charge (SOC) relates the currently stored energy to the nominal storage capacity

$$\text{SOC} = \frac{E^s - E_{\text{ref}}^s}{\Delta E_{\text{nom}}^s}. \quad [2.7]$$

A reference state  $E_{\text{ref}}^s$  is used for the definition here instead of the minimum value, due to the minimum values variability. The nominal storage capacity is also used to define the self discharge loss as Self Discharge Rate (SDR) over the observation time period  $\Delta t$  as

$$\text{SDR} = \frac{E_{\text{sd}}}{\Delta t \Delta E_{\text{nom}}^s}. \quad [2.8]$$

An energy density may be defined for an energy storage system as volumetric ( $\text{J}/\text{m}^3$ ) or gravimetric value ( $\text{J}/\text{kg}$ ). For stationary energy storage systems the volumetric density is important, as it defines the spacial requirement for the storage unit. Mobile applications on the other hand generally require high gravimetric densities in order to limit the vehicle mass.

The nominal rate of charge for an energy storage system  $\dot{E}_{\text{c,nom}}$  is used to define the nominal charge time as

$$\Delta t_{\text{c,nom}} = \frac{\Delta E_{\text{nom}}^s}{\dot{E}_{\text{c,nom}}}. \quad [2.9]$$

The nominal discharge time is defined accordingly and is in many cases equal, for example if the same machinery is used for the charge and discharge processes. The nominal charge or discharge time is also referred to as energy-to-power ratio. It may vary significantly according to the energy storage application case and can be for example seconds in the case of ancillary services for

the electricity grid or several months in the case of seasonal thermal energy storage.

Load changes of the charge and discharge process are often subject to technical restrictions. The power gradient or ramp rate for charge  $\partial \dot{E}_c / \partial t$  and discharge  $\partial \dot{E}_d / \partial t$  or the start-up or shut-down times can be used as measure.

## Economic Quantities

In order to quantify the energy turnover of a storage system in an observation time period the number of equivalent full cycles can be used. It is defined here as the ratio of energy input to the nominal storage capacity to make it less dependent on the storage efficiency

$$n_{\text{efc}} = \frac{E_{c,\text{in}} + E_{\text{sby}}}{\Delta E_{\text{nom}}^{\text{s}}} . \quad [2.10]$$

The number of equivalent full cycles depends at least on the energy storage application case and the usable capacity ratio.

To compare the cost of different energy storage technologies, the Levelized Cost of Storage (LCOS) may be used, which is the overall energy storage system cost divided by the amount of discharged energy. Capital cost  $C_{\text{cap}}$ , operation & maintenance cost  $C_{\text{o\&em}}$  and energy cost  $C_e$  are taken into consideration in this work. The consideration of energy cost is not handled consistently in literature. It is taken into account by Jülch [94], but neglected by Abdon et al. [1].

The capital cost of energy storage systems is often defined relative to the installed storage capacity (\$/MWh) or power (\$/MW) in literature. But in general, it is a function of both, installed power and storage capacity, and thus to the energy-to-power ratio or nominal charge and discharge time, which has to be considered when comparing the capital cost of different energy storage plants

$$C_{\text{cap}} = f(c_e, \Delta E_{\text{nom}}^S, c_p, \dot{E}_{\text{nom}}). \quad [2.11]$$

The capital cost can be related to the observation time period by means of a Capital Recovery Factor (CRF). For an observation time period of one year it can be determined from the interest rate  $r$  and service life in years  $n_a$  as

$$\text{CRF} = \frac{(1+r)^{n_a} r}{(1+r)^{n_a} - 1}. \quad [2.12]$$

The energy cost can be expressed by means of the mean energy price at charge  $\bar{c}_{e_c}$  and hold operation  $\bar{c}_{e_h}$  as

$$C_e = \bar{c}_{e_c} E_{c,\text{in}} + \bar{c}_{e_h} E_{s\text{by}}. \quad [2.13]$$

Neglecting the energy cost for standby demand and by means of Equations 2.4 and 2.10 the LCOS for an observation period of one year can be written as

$$\text{LCOS} = \frac{\text{CRF} C_{\text{cap}} + C_{\text{o\&m}}}{\eta n_{\text{efc}} \Delta E_{\text{nom}}^S} + \frac{\bar{c}_{e_c}}{\eta}. \quad [2.14]$$

In this form, the LCOS can be used to demonstrate the importance of the efficiency and number of equivalent full cycles on the economics of energy storage systems.

The capital cost for a storage system is divided by the number of equivalent full cycles. In consequence, the relevance of the capital cost increases at low numbers of equivalent full cycles.

The mean energy price at charge is divided by the efficiency, as more energy has to be purchased for a less efficient storage system in order to discharge the same amount of energy. Consequently, the relevance of the efficiency on the LCOS decreases for low mean energy prices at charge. But as the efficiency is an important factor in a storage unit's marginal cost, it is also relevant to the

merit order of storage dispatch.

## Environmental Footprint

Besides the technical and economic quantities, the environmental footprint should be taken into consideration when evaluating energy storage systems. Possible measures are resource depletion, global warming potential or land use. For the assessment the full life cycle must be taken into account, which includes production, transport, use phase and recycling or disposal. Examples are provided by Immendoerfer et al. [84], comparing the environmental footprint of pumped hydro energy storage and batteries, and Scharrer et al. [154] for a Carnot Battery concept including geothermal heat supply.

## 2.3 Review on Electric Energy Storage

EES can serve various applications in the electricity sector, such as

1. balancing of VRE and demand,
2. ancillary services such as frequency and voltage control,
3. peak load shaving,
4. transmission investment deferral or
5. uninterrupted power supply.

Balancing of VRE generation and electricity load leads to a high demand for energy storage capacity. But it also poses high requirements towards the EES capital cost, as the number of equivalent full cycles per year can be relatively low, according to the characteristic fluctuations of wind and solar energy availability and electricity load. Higher numbers of equivalent full cycles can be achieved for example when providing ancillary services, but the required storage capacity is much more limited.

Each EES application leads to different requirements towards the nominal charge and discharge time or energy to power ratio. According to Abdon et al. [1], EES applications may be classified as short ( $\approx 0.01$  h), medium ( $\approx 4.5$  h)

and long term ( $\approx 2160$  h). Different EES technologies are suitable for different energy to power ratios and number of full cycles according to their capacity- and power-specific capital cost and efficiency. An overview on the typical energy to power ratios of several EES technologies can be found as Ragone chart in the book of Sterner et al. [171].

A comparison of system cost for different EES technologies has been done by Jülch [94]. A mix of energy storage technologies according to each specific strengths is likely to be most economic, as shown for example by Schmidt et al. [157].

Some frequently discussed EES technologies are briefly introduced in the following.

**Pumped hydro energy storage** is the most common large-scale EES technology today. It accounts for 96 % of the worldwide storage capacity according to [87]. The round-trip efficiency is relatively high at 75 to 85 % and the service life is larger than 40 years [43]. But it is restricted to sites offering geographical elevation differences [149] and has a high land use as the volumetric energy density is relatively low. For an elevation difference of 540 m the energy density is  $1.5 \text{ kWh/m}^3$  [171].

**Compressed Air Energy Storage (CAES)** stores energy as pressure increase in an air volume, which increases the exergy fraction of the internal energy. The first plant was commissioned in 1978 in Huntorf, Germany, a second in 1991 in McIntosh, USA. Both plants use natural gas to heat the air before expansion at discharge. Adiabatic CAES uses TES to increase the round-trip efficiency, values around 70 % are expected [169]. A first experiment on adiabatic CAES has been published by Wang et al. [188]. CAES also requires geographical prerequisites in the form of large natural caverns. The volumetric energy density is in the range of 5 to  $20 \text{ kWh/m}^3$  for pressures of 50 to 100 bar [169]. A range of 400 to 800 \$/kW is estimated for the capital cost by Chen et al. [35].

**Flywheels** store energy as kinetic energy of a rotating mass. The energy density is around  $20 \text{ kWh/m}^3$  for a steel flywheel at 5000 rpm. The maximum speed of available units is 100 000 rpm [131]. Major drawback is the self discharge due to friction losses. In an example provided by Ibrahim et al. [83] the self discharge rate is at 55 % per day.

**Electrochemical energy storage** includes several different battery technologies, but lithium-ion batteries accounted for nearly 90 % of the worldwide large-scale battery storage additions in 2017 according to [88]. Lithium-ion batteries benefit from innovations in the mobility sector [86] leading to significant cost reductions, but are still costly for grid-scale energy storage. In 2018 the installed storage capacity of large-scale battery storage systems in Germany was 550 MWh with an accumulated power of 400 MW, mainly providing ancillary services [62]. A production cost in the range of 75 to 1130 \$/kWh is projected at a production capacity of 1 TWh per year by Schmidt et al. [157]. Resource limitations to lithium may restrict a cost reduction [36]. Lithium-ion batteries have a limited cycle life. Their efficiency is in the range of 85 to 90 % [43]. The volumetric energy density is around  $0.3 \text{ MWh/m}^3$  [171].

**Hydrogen** can be generated from water by electrolysis and used as chemical energy storage medium. It can be stored, fed into the natural gas grid up to a limited mass fraction, further transformed to synthetic methane or used for other purpose. Fuel cells or gas turbines can be used to regenerate electricity. The volumetric energy density is high, being  $0.4 \text{ MWh/m}^3$  for hydrogen and  $1.2 \text{ MWh/m}^3$  for methane at 200 bar [171]. The uninstalled system cost for a proton exchange membrane technology electrolyzer is 230 \$/kW at a production capacity of 100 GW per year according to Mayyas et al. [120]. The capacity-specific storage capital cost on the other hand is low. Main challenge is to increase the efficiency of the conversion processes [28]. According to Das et al. [43], the round-trip efficiency is in the range of 25 to 58 % for a  $\text{H}_2$  storage system with a fuel cell for electricity generation.

## 2.4 Carnot Batteries

Carnot Batteries convert electric energy to thermal energy at charge, store the thermal energy and convert it back to electricity at discharge. According to Steinmann [169], Carnot Batteries can be categorized as thermo-mechanical energy storage along with CAES. Carnot Batteries are seen as promising EES technology for balancing of VRE and demand according to their general advantages of

- site independence,
- scalability to large units in the 100 MW range,
- independent scaling of nominal charge and discharge power as well as storage capacity,
- low capacity-specific capital cost,
- long life expectancy and
- relatively high volumetric energy density, leading to a limited land-use.

Due to the interim thermal energy storing, Carnot Batteries are inherently able to get integrated in thermal energy networks as well. In this way, they can support the integration of the electricity and heat sectors. Possible options are

1. the intake of low-temperature heat at charge to improve the efficiency or provide cooling [153],
2. an output of low-carbon heat from VRE upon thermal demand or
3. cogeneration of heat and power at discharge in order to increase the overall energy utilization rate.

The charge process can either be electric heating or a heat pump cycle [170], leading to very different system characteristics. Therefore, Carnot Batteries are further classified as Power Heat Power Energy Storage (PHPES) in the first case and Pumped Thermal Energy Storage (PTES) in the second, according to Steinmann [169]. Carnot Batteries further consist of at least one TES unit and a heat engine as discharge process. Figure 2.2 illustrates both concepts.

A TES unit is used in most PTES concepts as low-temperature thermal reservoir instead of the environment, as the temperature level of a low-temperature TES

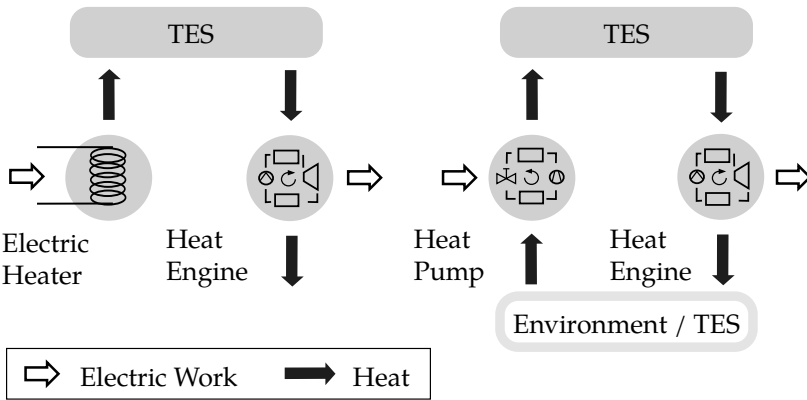


**Figure 2.2 /** Comparison of the PHPES (left side) and PTES (right side) concepts. For PTES a low-temperature TES can be used instead of the environment, in which case the environment may also work as upper-temperature thermal reservoir.

can be fitted to the process and it provides further storage capacity. But it is not generally necessary. When using a TES below ambient temperature, as for example in the case of cryogenic energy storage [79], it is also possible to replace the upper-temperature TES with the environment.

In order to discuss the differences between the PHPES and PTES concept in this section, the power-based efficiency for a heat engine  $\eta$  and Coefficient of Performance (COP) for a heat pump are used

$$\eta = \frac{|\dot{W}_{\text{out}}|}{\dot{Q}_{\text{in}}} \quad \text{and} \quad \text{COP} = \frac{|\dot{Q}_{\text{out}}|}{\dot{W}_{\text{in}}}. \quad [2.15]$$

Additionally, an exergetic efficiency  $\zeta$  is introduced, which is defined as

$$\zeta = \frac{|\dot{E}_{X,\text{out}}|}{\dot{E}_{X,\text{in}}}, \quad [2.16]$$

and quantifies the quality of both processes according to the Second Law of Thermodynamics.

As the heat output of an electric heater is limited by the electric work input according to the First Law of Thermodynamics and the conversion of heat to electric work in a heat engine is limited by the Carnot efficiency, as shown in Equation 2.3, the round-trip efficiency of a PHPES system is also restricted by the Carnot efficiency. Consequently, a thermodynamic cycle with a high upper temperature level should be used for discharge and thus high-temperature TES is substantial for PHPES systems in order to increase the round-trip efficiency.

PTES systems on the other hand use a heat pump cycle at charge. The upper limit for the heat pump COP according to the Second Law of Thermodynamics is

$$\text{COP}_{\text{carnot}} = \frac{T}{T - T_{\text{env}}} \quad [2.17]$$

Figure 2.3 shows the heat engine efficiency  $\eta$  and heat pump COP for a PTES system with the environment as low-temperature thermal reservoir as function of the exergetic efficiency for these processes and the thermodynamic mean temperature at heat transfer to and from the TES.

It can be seen, that the PTES round-trip efficiency is

$$\eta \cdot \text{COP} = 1 \quad \text{for} \quad \zeta = 1 \quad [2.18]$$

at any TES temperature level, as the Carnot efficiency limit of the heat engine is compensated by the ideal heat pump coefficient of performance. Consequently, PTES system can reach higher efficiencies compared to PHPES systems and may utilize TES with lower temperatures. However, a TES temperature level closer to the environment leads to an increase of required thermal storage capacity, as the exergy content is lower.

The efficiency advantage of heat pump utilization in comparison to direct electric heating is reduced with increasing storage temperatures. For example, at a thermodynamic mean temperature of heat transfer to and from the TES of 400 °C, the heat pump exergetic efficiency must be above 0.59 in order to even

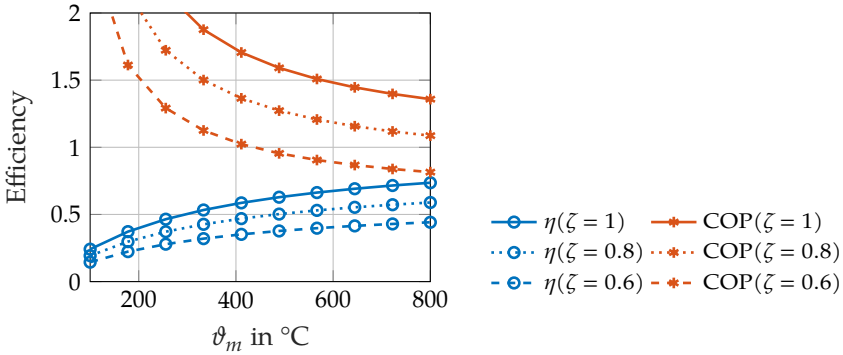


**Figure 2.3** / Heat engine efficiency  $\eta$  and heat pump coefficient of performance COP for a PTES system as function of the exergetic efficiency  $\zeta$  for both processes and the thermodynamic mean temperature at heat transfer to and from the upper temperature TES  $\vartheta_m$ . The environment is used as low-temperature thermal reservoir with a thermodynamic mean temperature of heat transfer to and from the environment at  $\vartheta_{m,\text{env}} = 10^\circ\text{C}$ .

reach a COP > 1.

In exchange for the efficiency advantage, PTES systems are generally more complex than PHPES, as the temperature levels of the heat pump, TES and heat engine have to match in order to minimize exergy losses associated with temperature differences at heat transfer. Therefore, PTES systems may require several storage units at different temperature levels, or combinations of latent and sensible heat storage. Some PTES concepts furthermore rely on compressors with higher operating temperatures compared to the current state of art [169], leading to a lower level of technology readiness.

A selection of recent PTES concepts described in the scientific literature are

- Desrues et al. [47] use two regenerators as TES and a closed Brayton cycle,
- Howes [81] use packed-bed TES and reciprocating compressor and expansion unit,
- Mercangöz et al. [124] use hot water and ice storage and a transcritical CO<sub>2</sub> cycle,
- Steinmann [168] use a combination of sensible and latent TES, a conven-

tional steam cycle for discharge and a multistage ammonia and steam compression cycle at charge,

- Morgan et al. [128] use liquid air as storage medium, an air liquefier for charge and a Rankine cycle for discharge,
- Laughlin [110] use molten salt and cryogenic TES and a closed Brayton cycle and
- Eppinger et al. [54] use pressurized hot water TES and an organic Rankine cycle.

A further overview on Carnot Batteries is given by Dumont et al. [53]. The simulated efficiencies for several high-temperature PTES concepts are compared by Steinmann et al. [170].

## 2.5 Review on High-Temperature Thermal Energy Storage

The storage temperature is a key figure to TES. Whereas temperatures below 100 °C are generally sufficient for space heating, many heat engines and industrial processes require higher temperatures. The common TES technology for space heating is sensible heat storage in water [18], especially due to its low cost. In accordance with Gasia et al. [65], high-temperature TES is defined as above 150 °C.

High-temperature TES has been developed primarily for Concentrated Solar Power (CSP). CSP plants store thermal energy to allow a load-following power plant operation, with the main goal to also generate electricity during the night. Other applications for high-temperature TES include adiabatic CAES, waste heat recovery, power to heat for industrial processes or flexibilization of thermal power plants.

Thermal energy can be stored in the form of sensible and latent heat or by means of a reversible thermochemical reaction [68].

Sensible and latent TES are subject to self-discharge via heat transfer to the environment. The rate of heat transfer depends on the storage temperature

and surface area. Thermal insulation can be used to diminish the heat transfer, it's thickness is only restricted by the cost and spacial requirement for it. Larger storage units have lower specific heat losses at the same thermal insulation effort, as the surface area of a body grows weaker with size than volume. Consequently, the capacity-specific cost of thermal energy storage generally decreases with the size of the storage unit.

**Sensible heat storage** is based on a storage material temperature increase. The energy density therefore depends on the achievable temperature difference. Molten salt in separate tanks for the hot and cold salt are a state-of-the-art sensible high-temperature TES technology for CSP [59, 112]. But the restricted operating range for molten salt due to its freezing point of 120 to 220 °C and decomposition temperatures of 450 to 585 °C [112], its corrosive nature and a relatively high price of 28 \$/kWh<sub>th</sub> for a two-tank molten salt system [112] encourage the search for alternative technologies. In comparison with molten salt, many solid materials are resistant to higher temperatures and have 90 to 95 % lower cost per heat capacity [169]. On the other hand, solid storage material is generally not pumpable, thus a heat transfer fluid for charge and discharge is required. Regenerators, such as hot blast stoves in the steel industry, store thermal energy for short time periods. Novel high-temperature TES concepts for longer storage duration, which are based on solid storage materials include custom-developed concrete with tubes inserted for the heat transfer fluid [80], stacked bricks [104, 201], steel blocks [113] or packed beds of various storage material, further reviewed below.

**Latent heat storage** with phase change materials offers the advantage of heat transfer at nearly constant temperature and 5 to 14 times higher volumetric storage capacities in comparison to sensible heat storage according to Wei et al. [191]. Nevertheless, phase change materials for temperatures above 300 °C are not technically mature [191], even though hundreds of storage materials based on inorganic salts or metal alloys have been proposed [96]. A novel phase change material for high temperatures used by a company named *1414 Degrees* [45] is silicone.

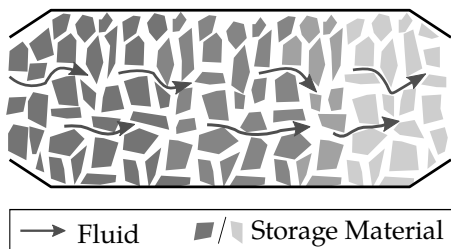


**Figure 2.4 /** Illustration of a packed-bed thermal energy storage unit at charge. The grayscale indicates different temperatures.

**Thermochemical energy storage** offers 5 to 10 times higher volumetric storage capacities in comparison to latent and sensible heat storage according to Pardo et al. [143]. But so far only laboratory and pilot experiments have been done [143] and the complexity as well as cost of the technologies hinders the application [3]. A recent example for high-temperature thermochemical energy storage is nano-encapsulated salt, developed by SaltX [151], in combination with water.

## 2.6 Packed-Bed Thermal Energy Storage

Packed beds can be used as arrangement for particulate solid thermal energy storage material. Furthermore, it is proposed for fluids encapsulated in small solid containments, as for example by Oró et al. [139]. The heat transfer fluid flows through the packed-bed pores and is in direct contact with the solid material or fluid containment. Figure 2.4 illustrates a packed-bed storage unit.

Due to the large surface area of the storage material, the thermal resistance between heat transfer fluid and storage material is low and any temperature differences between them inside the packed bed quickly dissolve. This leads to the formation of a thermocline in the packed bed, when charging and discharging the TES in opposite flow direction with distinct inlet temperatures. The thermocline moves with the fluid flow in charge or discharge direction at a slower speed, which depends on the heat capacity of the storage material and heat transfer fluid. As the thermocline separates the hot and cold part of the storage, a single storage unit is generally sufficient, but it limits the usable capacity ratio in return.

**Table 2.1** / Exemplary nominal volumetric energy densities  $\Delta E_{\text{nom}}^s/V_{\text{bed}}$  for packed-bed thermal energy storage at  $\Delta T = 500$  K, as well as the storage material density  $\rho$ , heat capacity  $c_v$  at  $400^\circ\text{C}$  and packed-bed porosity  $\varepsilon$ .

Material	$\rho$ $\frac{\text{kg}}{\text{m}^3}$	$c_v$ $\frac{\text{J}}{\text{kg K}}$	$\varepsilon$ -	$\frac{\Delta E_{\text{nom}}^s}{V_{\text{bed}}}$ $\frac{\text{MWh}_{\text{th}}}{\text{m}^3}$	Reference
Crushed Diabase	2750	960	0.45	0.2	Soprani et al. [166]
Pebbles	2700	1000	0.340	0.25	Zanganeh et al. [198]
Alumina Spheres	3950	1100	0.375	0.38	Anderson et al. [10]
Steel Slag	2850	960	0.4	0.23	Cabello et al. [30]

Predominately gases are used as heat transfer fluids in high-temperature packed-bed TES to avoid phase change in the operating range. Air offers the advantages of environmental harmlessness in case of leakage or intentional venting and low cost. Liquids, such as molten salt [142], thermal oil [29] or liquid metal [108], have higher densities and therefore allow lower volume flow rates. But as for molten salts, the operating range of thermal oil is limited. For synthetic thermal oil, the limit is around  $400^\circ\text{C}$  [18]. Naturally, a heat transfer fluid already present in the target application is generally preferred.

Various solid storage materials have been proposed in the literature for high-temperature packed-bed TES, such as natural rock [8, 135, 166, 198], silica sand [142, 155],  $\alpha$ -alumina spheres [10, 14, 34], steel slag [30, 101, 140], ceramic pebbles [97] or perforated concrete blocks [103]. Table 2.1 shows exemplary volumetric energy densities for some of the named materials at a temperature spread of  $500^\circ\text{C}$ .

Rock is an attractive solid storage material for large-scale stationary TES thanks to low cost and high availability. Allen et al. [5] estimate the system capital costs at 4 to 8  $\$/\text{kWh}_{\text{th}}$  for a storage unit with a power of  $100 \text{ MW}_{\text{th}}$ . However, the rocks have to endure repeated thermal cycling without fragmentation and the compressive strength must be high to bear the overlying rock pile. The mechanical stability of rocks is therefore an important indicator for the suitability as high-temperature packed-bed TES material. Furthermore, many rock types show degrading heat capacity and thermal conductivity at thermal cycling. A heat capacity reduction of 20 to 30% has been determined by Pedersen et al.

**Table 2.2** / Porosity  $\varepsilon$ , rock diameter  $d_p$ , maximum temperature  $\vartheta_{\max}$  and superficial air velocity  $v_{\text{air}}$  of the listed experimental setups for rock-bed TES with air as heat transfer fluid.

Rock Type	$\varepsilon$	$d_p$ mm	$\vartheta_{\max}$ °C	$v_{\text{air}}$ m/s	Reference
Pebbles	0.33 – 0.37	30	650	0.1 – 0.3	Zanganeh et al. [198]
Dolerite	0.45	53 – 73	530	0.1 – 0.7	Allen et al. [8]
Basalt	0.4	10 – 100	380	0.15 – 1	Odenthal et al. [135]
Diabase	0.45	16 – 22	600	0.01 – 0.09	Marongiu et al. [117]

[144] after repeated heating. Nevertheless, various rock materials have been found suitable in the literature [9, 20, 26, 132, 175].

An early large-scale rock-bed TES has been built in 1986 for the Solar One CSP plant in California, United States [60]. Recent experimental setups reported in the scientific literature using rock as the storage material and air as the heat transfer fluid are:

- Zanganeh et al. [197] built two vertical-flow pebble-bed storage units with a thermal storage capacity of approx. 6.5 MWh<sub>th</sub> and 100 MWh<sub>th</sub>.
- Allen et al. [8] tested a vertical-flow packed bed with a thermal storage capacity of approx. 0.4 MWh<sub>th</sub>.
- Odenthal et al. [135] investigated a packed bed with horizontal air flow direction, but later replaced the packed bed with bricks [136].
- Soprani et al. [166] built a horizontal-flow packed-bed storage unit with a thermal storage capacity of 0.45 MWh<sub>th</sub>.

Table 2.2 shows the operating conditions as well as the porosity and rock diameters of the listed experimental setups. It should be noted, that the maximum temperature used in the published experimental setups does not necessarily correspond to general temperature limits for these rock types.

### 2.6.1 Design

The design of packed-bed TES has to deal with several challenges. First of all, an uneven flow distribution in the packed-bed storage must be avoided, as storage material is bypassed at charge or discharge and the thermal storage capacity of the packed bed is reduced. Reasons for uneven flow can be a void space above the packed-bed inside the storage containment due to the thermal expansion of the packed-bed, porosity variations or abrupt changes of the flow cross area. The thermal expansion of basalt and granite was found to be at 0.8 and 3.2% respectively when heated from 0 to 1000 °C by Hartlieb et al. [75]. A characteristic porosity reduction is in the vicinity of rigid walls for spherical particles.

The mechanical stability of the particles and packed-bed containment has to be ensured, especially with respect to thermal cycling. The containment may thermally expand and contract, leading to a densification of the packed bed and possibly high forces [52, 152]. Furthermore, the particles may perform small relative movements after their thermal expansion. Consequently, the tolerable mechanical forces on the particles and containment limits the allowable packed-bed height. A limit of 5 to 9 m has been calculated for example by Dreißigacker [51]. A limit of 16 m is set by Pacheco et al. [142].

The flow of heat transfer fluid through the packed bed leads to a pressure and associated pumping loss. Furthermore, the heat transfer modes in the packed bed besides advection, which lead to a leveling of thermal gradients and thus thermal destratification, must be minimized, as they reduce the usable storage capacity.

In order to deal with these challenges, several design options are available. One is the main flow direction inside the packed bed. It can be axial in either horizontal or vertical direction, radial or a mixture of these. Figure 2.5 shows the basic flow directions proposed for packed-bed TES in literature.

A vertical flow leads to better thermal stratification, if the charging is done from the top, but leads to more constructional effort for the support structure [135]. Especially the heat transfer fluid inlet from the bottom is elaborate for large-scale units, due to the high storage material weight. A possible design solution is the insertion of a vertical duct in the packed bed, as proposed by

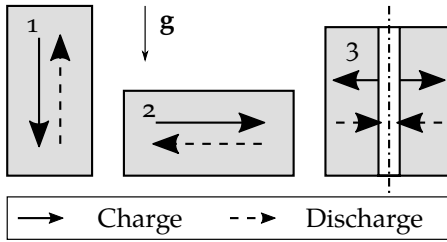


**Figure 2.5 /** Flow directions proposed for packed-bed TES: vertical (1), horizontal (2) and radial (3).

Allen et al. [5]. At horizontal flow, natural convection may lead to additional thermal destratification and thus a lower usable capacity ratio, especially for long hold periods. The effect can be reduced by smaller sized particles, higher air velocities or optimized flow control [117]. Embedded horizontal impermeable layers were also found to suppress the natural convection impact [166].

At radial flow, the charging direction may be either from the inside or outside of the packed bed. The former option promises less heat losses, as the packed-bed outside remains relatively cold. The second option offers lower air velocities in the hot outer packed bed [8, 109]. A lower air velocity in the hot part of the packed bed is beneficial, as it compensates the effect of low air density in order to reduce the overall pressure loss. McTigue et al. [121] found, that radial-flow packed-bed TES achieve similar efficiencies compared to axial flow, but at a lower usable capacity ratio and therefore higher cost, as the large share of outer storage material is only exposed to a small temperature variation.

At axial flow, the aspect ratio of the packed bed is an important design parameter. It is defined in this work with the length of the packed bed in main flow direction  $\Delta x_{\text{bed}}$  and a characteristic cross area  $A_{\text{bed,cross}}$  as

$$\chi = \frac{\Delta x_{\text{bed}}}{\sqrt{A_{\text{bed,cross}}}} . \quad [2.19]$$

The effect of the aspect ratio on the performance has been investigated by several authors [33, 118, 125]. High aspect ratios lead to high mean air velocities at equal mass flow rates according to the low cross area, which increases the pressure loss along with the increased length. On the other hand, low aspect

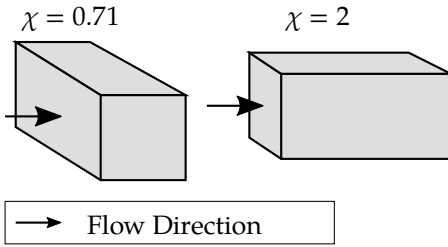


**Figure 2.6 /** Examples for rectangular axial-flow packed-beds with different aspect ratio according to Equation 2.19.

ratios decrease the usable capacity ratio, as the large cross area increases the internal heat transfer. An example for a packed-bed design with a very low aspect ratio is given by Schlipf et al. [155], connecting multiple thin packed-bed sections in parallel. The aspect ratio also effects the constructional effort for the air in- and outlet of the packed bed, which should be designed to achieve an even flow distribution at the packed-bed entrance. Figure 2.6 shows two axial-flow packed beds with different aspect ratios as example.

A variation of the packed-bed cross area along the main flow direction has been investigated by Zanganeh et al. [198]. A vertical-flow packed bed with a conical shape and a larger diameter at the upper hot end has been used in their experimental setups to reduce the normal force on the walls by guiding the rocks upwards at thermal expansion. However, it was found later by Marti et al. [118], that a smaller cross section at the hot end would lead to higher exergetic efficiency due to the reduced heat loss.

The sensitivity of the packed-bed performance on the particle size has been investigated by various authors as well [117, 118, 164]. Smaller particles significantly increase the packed-bed pressure loss, but offer several benefits to the usable capacity ratio, such as

1. an increase of the particle surface area per volume, leading to a higher volumetric particle-to-fluid heat transfer coefficient and thus steeper thermoclines,
2. a reduction of the intra-particle thermal resistance effect on the particle-to-fluid heat transfer coefficient,
3. a reduction of the effect of radiant internal heat transfer in the packed bed, which becomes more important than conduction at temperatures above 150 °C for air-rock beds according to Zanganeh et al. [198], as radiation can travel further for larger pore spaces and

4. less advective mixing due to the packed-bed pores tortuosity.

Broader particle size distributions decrease the porosity compared to mono-sized particles [107], with a positive effect on the nominal thermal storage capacity. On the other hand, the porosity strongly affects the packed-bed pressure loss. For example, at a porosity of 0.4, a deviation of 1 % in porosity causes a deviation of 4 % in pressure loss according to Achenbach [2].

In segmented packed beds, the air is only flowing through a small portion of the bed, bypassing the other. The segmentation thus reduces the pressure loss and diminishes internal heat flow [24, 121]. For example, a pressure loss reduction of 1 to 4 % has been determined by McTigue et al. [121]. But the efficiency gain comes at the cost of additional flow control fittings.

## 2.6.2 Modeling

For packed beds of a much larger size than the particle size, the macroscopic behavior, such as the flow and temperature field, can be modeled by means of a continuously distributed porous medium. In this way, it is not necessary to resolve the irregular structure of packed bed pores, which significantly reduces the complexity. The respective models are referred to as porous-media models and are generally composed of a porous medium continuity equation, momentum and energy balance.

Numerical simulation with the finite volume method is often used to investigate packed-bed macroscopic behavior. The main intention is to analyze storage units larger than state of the art, thus reducing the cost for experiments, to perform design optimization or investigate system integration. Models may be categorized as one-, two- or three-dimensional.

1. One-dimensional models are only discretized in the main flow direction of the heat transfer fluid and used by most authors. Examples are the models described by Barton [16] and Hänchen et al. [74].
2. Two-dimensional models can account for gradients in lateral direction for symmetrical packed beds, such as cylinders. Two examples, namely the  $\alpha_W$  and  $\Lambda_r(r)$  model are presented in the *VDI Heat Atlas* [13, section Mh].

3. Three-dimensional models offer the highest flexibility to describe the temperature and flow field in packed beds, but are computationally most expensive. Many CFD codes are able to model porous media. CFD codes have been used for example by Zavattoni et al. [199] and Cascetta et al. [34].

The physical conditions at particle scale are accounted for as effective packed-bed properties in the porous-media models. The most relevant packed-bed properties in the case of TES are the

1. porosity,
2. particle surface area per unit volume,
3. local heat transfer fluid pressure gradient,
4. particle-to-fluid heat transfer coefficient,
5. effective thermal conductivity at stagnant fluid and
6. packed-bed-to-wall heat transfer coefficient.

These packed-bed properties are generally derived from experimental results. But according to the large number of influential quantities, such as

- particle shape,
- particles size distribution,
- material properties and
- packing process,

the correlations have a limited applicability [7]. Furthermore, the material properties for natural rocks may vary from quarry to quarry or even within one quarry.

An overview on the modeling of rock beds, including many empirical correlations for the packed-bed properties is given by Esence et al. [59]. For more details, the reader may refer to Nield et al. [133] or Lemos [111]. Many widely used packed-bed correlations are also collected in the *VDI Heat Atlas* [13].

In the following, the packed-bed properties are introduced. Furthermore, the porous-medium balance equations for mass, momentum and energy are defined along with the relevant dimensionless numbers. According to the targeted packed-bed TES application within the ETES concept, a gaseous

heat transfer fluid is generally assumed. The fluid velocity and therefore also the Mach number in the packed bed is generally small, as the pressure drop and associated fan work is a significant loss mechanism for packed-bed TES. In consequence, the flow can be modeled as incompressible, meaning the partial derivative of density with respect to pressure is small. Nevertheless, the fluid density is still variable according to the large temperature variation. The particles are assumed as stationary, rigid, non-porous themselves and polydisperse. Their shape may be irregular.

## Porosity

The most important porous-medium property is the porosity, which defines the local volumetric share of fluid in the packed bed

$$\varepsilon = \frac{V_f}{V_{\text{bed}}} . \quad [2.20]$$

The porosity may vary across the packed bed, which may lead to an uneven flow distribution as the flow will avoid packed-bed areas of lower porosity.

The porosity increases significantly in the vicinity of rigid walls for spherical particles, as they are in direct contact with the wall at a few points only. The porosity increase is lower for non-spherical particles. Furthermore, the porosity in beds of non-spherical particles levels in less than a distance of one particle diameter from the wall according to Giese [67]. Measured porosity variation in the vicinity of walls for spheres and irregular particle shapes are shown in the *VDI Heat Atlas* [13, section Mh]. The effect on the overall pressure loss can be neglected for large-scale packed beds, a limit of  $d_{\text{bed}}/d_p > 40$  is given by Meier et al. [122].

Beneath the particle size distribution, surface roughness and shape, the porosity depends on the densification of the packed bed, which can be increased up to a certain limit by mechanical processes, such as shaking. Packed beds of monodisperse spheres have a porosity of 0.36 to 0.38 in a dense state and 0.4 to 0.42 in a loose state [13, section Mh]. Cyclic thermal expansion may also lead to packed bed densification.

## Particle Size and Surface Area

The size of irregularly shaped particles is generally defined using equivalent diameters. In this thesis the diameter of a sphere with the particles volume

$$d_v = \sqrt[3]{\frac{6}{\pi} V_p} \quad [2.21]$$

is used. The sphericity of a particle is defined according to Wadell [183] as the ratio of the volume-equivalent spheres surface to the particles surface

$$\psi = \frac{\pi^{\frac{1}{3}} (6V_p)^{\frac{2}{3}}}{A_p}. \quad [2.22]$$

It can thus be used along with the volume-equivalent diameter to quantify the surface of a single irregularly shaped particle. For a polydisperse set of particles, the mean volume equivalent diameter is defined here using the overall particle volume and count as

$$\bar{d}_v = \sqrt[3]{\frac{6 \sum V_p}{\pi n_p}}. \quad [2.23]$$

In analogy to Equation 2.22, a mean sphericity can be defined for a set of particles as well

$$\bar{\psi} = \frac{n_p \pi^{\frac{1}{3}} \left(6 \frac{\sum V_p}{n_p}\right)^{\frac{2}{3}}}{\sum A_p}. \quad [2.24]$$

It can be interpreted as the ratio of the surface of a set of monodisperse spheres with the same number and overall volume as the particle set to the particles set overall surface. It should be noted that the mean sphericity, as defined in

Equation 2.24, does not solely depend on the particles shape, but also on the particle size distribution.

Using the given definitions, the particles surface per unit volume for polydisperse and irregularly shaped particles can be calculated as

$$a_{\text{bed}} = \frac{6(1 - \varepsilon)}{\bar{\psi} \bar{d}_v}. \quad [2.25]$$

Other widely used definitions for the particle size are the Sauter mean diameter, which is the diameter of a sphere with the same ratio of surface to volume as the particle,

$$d_{32} = \frac{6(1 - \varepsilon)}{a_{\text{bed}}}, \quad [2.26]$$

and the packed-bed hydraulic diameter, which refers to the flow channels in the packed bed

$$d_h = \frac{4\varepsilon}{a_{\text{bed}}}. \quad [2.27]$$

## Fluid Flow

The fluid velocity in porous media can be defined in two different ways. The superficial or seepage velocity is the average velocity per packed-bed volume and denoted as  $\mathbf{v}$  in this work. It is smaller than the mean pore velocity by the factor of porosity. With the superficial velocity, the continuity equation for fluid flow in a porous medium is

$$\varepsilon \frac{\partial \rho_f}{\partial t} + \nabla \cdot (\rho_f \mathbf{v}) = 0. \quad [2.28]$$

In order to differentiate flow regimes, the dimensionless Reynolds number can be used. It relates inertial to viscous forces in fluid flow and is defined for a porous medium in this work by means of the hydraulic diameter and mean pore velocity  $|\mathbf{v}|/\varepsilon$  as

$$\text{Re} = \frac{\rho|\mathbf{v}|d_h}{\mu\varepsilon}. \quad [2.29]$$

At low Reynolds numbers the pressure loss in porous media is proportional to the flow rate, as primarily revealed by Darcy [42]. For higher Reynolds numbers, the influence of inertial forces on the fluid flow increases and an additional body force proportional to the kinetic energy of the flow may be added. This term is referred to as Forchheimer correction, it is valid for fully turbulent flow according to Herwig et al. [77]. Consequently, the pressure gradient  $\nabla p$  is often modeled as

$$\nabla p = -\frac{\mu_f}{K}\mathbf{v} - \rho_f \frac{c_F}{\sqrt{K}}|\mathbf{v}|\mathbf{v}, \quad [2.30]$$

using the permeability  $K$  and inertial coefficient  $c_F$ . For very high Reynolds numbers an increasing deviation from this approach can be detected [2], but such conditions are avoided for packed-bed thermal energy storage, due to the corresponding high pressure and pumping loss. Popular choices for the permeability and inertial coefficient are the expressions

$$K = \frac{\varepsilon^3 d_{32}^2}{150(1-\varepsilon)^2} \quad \text{and} \quad c_F = \frac{1.75}{\sqrt{150\varepsilon^3}}, \quad [2.31]$$

determined experimentally by Ergun [57]. These terms were adopted by several authors in order to improve the correlation quality for certain particle shapes or size distributions, such as Allen et al. [8] and Macdonald et al. [115] for crushed rocks and Brauer [27] for mono-disperse spheres.

To model the fluid flow through a porous-medium, the right side of Equation 2.30 may be added as an additional body force to the free-flow momentum

balance [163]. An exemplary equation according to Nield et al. [133, page 17] is

$$\frac{\rho_f}{\varepsilon} \left[ \frac{\partial \mathbf{v}}{\partial t} + (\mathbf{v} \cdot \nabla) \frac{\mathbf{v}}{\varepsilon} \right] = -\nabla p \mathbf{I} + \frac{\mu_f}{\varepsilon} \nabla^2 \mathbf{v} + \rho_f \mathbf{g} - f_{\text{bed}} \quad \text{with} \quad [2.32]$$

$$f_{\text{bed}} = \frac{\mu_f}{K} \mathbf{v} + \rho_f \frac{c_F}{\sqrt{K}} |\mathbf{v}| \mathbf{v}.$$

The Euler number is used as dimensionless expression for the packed-bed body force in this work

$$\text{Eu} = f_{\text{bed}} \frac{d_h \varepsilon^2}{\frac{\rho}{2} v^2}. \quad [2.33]$$

Turbulence has a minor influence on the flow through the packed-bed pores, due to the narrow flow channels. But it is still relevant, especially with increasing velocity. Still, turbulence is generally not included in the macroscopic porous-media momentum balance, as the effect of the turbulence is already accounted for within the packed-bed body force.

## Heat Transport

An overview on the various modes of heat transport in packed beds is given in Figure 2.7. The advective heat transport may be due to forced or natural convection. As the packed bed is modeled as a continuous porous medium, advection in the model is not affected by the pore structure. To account for the fluid mixing effect due to the packed-bed tortuosity and associated heat transport, advective mixing is added as transport mechanism. Solid heat conduction in the containment or insulation material may also contribute to the overall heat transport.

In order to model the macroscopic packed-bed heat transport, all transport modes other than advection are modeled as proportional to the temperature

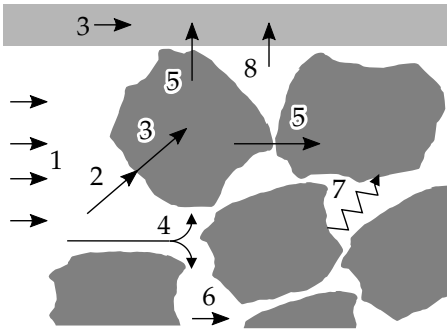


**Figure 2.7 /** Modes of heat transport in packed beds: advection (1), particle-to-fluid heat transfer (2), solid conduction (3), advective mixing (4), contact conduction (5), fluid conduction (6), radiation (7) and fluid-to-wall heat transfer (8).

gradient in analogy to heat transfer in solid material and accordance with Fourier's Law

$$\dot{Q}_{\text{cond}} = -\lambda A \nabla T. \quad [2.34]$$

The resulting packed-bed thermal conductivity is referred to as Effective Thermal Conductivity (ETC), as it is not a material property.

The intra-particle thermal resistance can be accounted for alongside with the convective heat transfer from the fluid to the particle surface in a lumped capacitance approach by means of an effective particle-to-fluid heat transfer coefficient. Alternatively, a separate dynamic energy balance for the intra-particle temperature field may be used, but this approach is generally restricted to regularly shaped particles. Xu et al. [194] found good accordance for the lumped capacitance approach with an analytical solution for several particle shapes.

### Packed Bed Energy Balance

With the effective thermal conductivity and lumped capacitance approach, the temperature distribution in packed beds can be modeled by means of an energy balance with distinct local mean temperatures for the particle and fluid part of the packed bed  $T_p$  and  $T_f$  as

$$\begin{aligned}
(1 - \varepsilon)\rho_p \frac{\partial u_p}{\partial t} &= \alpha_{\text{eff}} a_{\text{bed}} (T_p - T_f) + \nabla \cdot (\lambda_{\text{eff}} \nabla T_p) \\
\varepsilon \rho_f \frac{\partial u_f}{\partial t} + \rho_f \mathbf{v} \cdot \nabla h_f &= -\alpha_{\text{eff}} a_{\text{bed}} (T_p - T_f) + \alpha_{\text{bed-w}} a_w (T_w - T_f).
\end{aligned} \tag{2.35}$$

This model is also referred to as two-equation model. The packed-bed-to-wall heat transfer only appears at the respective boundaries. The assignment of the ETC and packed-bed-to-wall heat transfer to the particle or fluid energy balance is not conclusive, but may play an inferior role, due to the large volume-specific particle surface and therefore particle-to-fluid heat transfer [59].

Due to the large particle surface, the temperature difference between the particles and fluid is generally small, which requires small time steps in numerical simulation to avoid instabilities for the two-equation model. Therefore a one-equation model, which does not differentiate between particle and fluid temperature but uses a local mean bed temperature  $T_{\text{bed}}$ , is an alternative. The energy balance for the one-equation model is

$$\begin{aligned}
\frac{\partial(\rho u)_{\text{bed}}}{\partial t} + \rho_f c_{pf} \mathbf{v} \cdot \nabla T_{\text{bed}} &= \nabla \cdot (\lambda_{\text{eff}} \nabla T_{\text{bed}}) + \alpha_{\text{bed-w}} a_w (T_w - T_{\text{bed}}) \\
\text{with } (\rho u)_{\text{bed}} &= (\varepsilon \rho_f c_{vf} + (1 - \varepsilon) \rho_p c_{vp}) T_{\text{bed}}.
\end{aligned} \tag{2.36}$$

The approach is generally valid for very small temperature differences and is therefore also referred to as local thermal equilibrium approach. The applicability of the assumption has been evaluated by La Pitot de Beaujardiere et al. [105]. They concluded, that in the range of their boundary conditions the one-equation model is a reasonable simplification with minor effect on the packed-bed performance but substantial computational cost savings. Ismail et al. [90] found, that their one-equation model needs 11% of the two-equation models computational time. But it must be noted, that the applicability for large particle sizes and high fluid velocities is unclear, even when using the corrective approach of Vortmeyer et al. [182], as further described in Section 2.6.2.

## Effective Particle-to-Fluid Heat Transfer Coefficient

The particle-to-fluid heat transfer coefficient is defined with the difference of the local mean particle surface and fluid temperature

$$\alpha_{p-f} = \frac{1}{a_{\text{bed}} V} \frac{\dot{Q}}{\bar{T}_{p,\text{surf}} - \bar{T}_f}. \quad [2.37]$$

The Nusselt number may be used as dimensionless quantity for the particle-to-fluid heat transfer coefficient. It is defined in this work as

$$\text{Nu}_{p-f} = \frac{\alpha_{p-f} d_h}{\lambda_f}. \quad [2.38]$$

Various empirical correlations are reported in the literature for the particle-to-fluid heat transfer coefficient in dimensionless form, generally relating the Nusselt number to the Reynolds and Prandtl numbers. An exemplary correlation by Wakao et al. [184] is

$$\text{Nu} = 2 + 1.1 \text{Re}^{0.6} \text{Pr}^{\frac{1}{3}} \quad [2.39]$$

Further correlations have been developed by Gnielinski [69] or Coutier et al. [40]. It has to be noted, that different definitions for the heat transfer coefficient are used, for example by means of the logarithmic mean temperature difference.

The Prandtl number consists solely of fluid properties and relates the momentum to thermal diffusivity. It is defined as

$$\text{Pr} = \frac{\mu_f c_{vf}}{\lambda_f}. \quad [2.40]$$

The effective particle-to-fluid heat transfer coefficient  $\alpha_{\text{eff}}$ , as used in Equa-

tion 2.35, is defined using the local mean temperature of the particle and fluid fraction in an packed bed control volume  $V$

$$\alpha_{\text{eff}} = \frac{1}{a_{\text{bed}} V} \frac{\dot{Q}}{\bar{T}_p - \bar{T}_f}. \quad [2.41]$$

It thus incorporates the effect on the intra-particle thermal resistance according to the lumped capacitance approach. Its relevance is generally quantified by the Biot number, which is defined here using the Sauter mean diameter  $d_{32}$  as

$$\text{Bi} = \frac{\alpha_{p-f} d_{32}}{\lambda_p}. \quad [2.42]$$

In order to relate the effective and particle-to-fluid heat transfer coefficient, a correlation for the ratio of both coefficients  $\alpha_{\text{eff}}/\alpha_{p-f}$  can be used. Such a correlation according to Stuke [172] is

$$\frac{\alpha_{\text{eff}}}{\alpha_{p-f}} = \left(1 + \frac{1}{B} \text{Bi}\right)^{-1}. \quad [2.43]$$

The constant  $B$  depends on the particle shape and is 10, 8, and 6 for spheres, cylinders and slabs [59, 194].

## Effective Thermal Conductivity

The ratio of a thermal conductivity to the fluid thermal conductivity  $k$  is used in the following to work with dimensionless values

$$k = \frac{\lambda}{\lambda_f}. \quad [2.44]$$

The ETC can be modeled as superposition of an conductivity at stagnant fluid and a contribution due to advective mixing, which only occurs at fluid flow

$$k_{\text{eff}} = k_{\text{eff},o} + k_{\text{eff},\text{mix}} \cdot \quad [2.45]$$

The flow-related ETC is non-isotropic, it has to be differentiated at least between the flow direction and others. The dependency of the ETC on the fluid flow has been described for example by Yagi et al. [196]. Several modeling approaches are compared by Alazmi et al. [4]. The simplest model is a proportionality to the Peclet number, which is the product of the Reynolds and Prandtl numbers

$$k_{\text{eff},\text{mix}} = \frac{1}{B} \text{Re Pr} \cdot \quad [2.46]$$

Different constants  $B$  for directions perpendicular to the flow have been determined by Bauer [17] for large packed beds and different particle shapes as shown in the *VDI Heat Atlas* [13, section Mh]. The values 2 and 10 are determined by Wakao et al. [185] for the flow and perpendicular direction respectively [59].

Following the derivation of Vortmeyer et al. [182], the flow-related part of the ETC in the one-equation model in flow direction may be replaced with another term, which is a result of their comparison of the one- and two-equation models. Among other assumptions, an equality of the second derivative of the local particle and fluid temperature is required for the derivation, but not an equality of the temperatures themselves. The advantage is that the new term accounts for the particle-to-fluid heat transfer effect in the one equation model, which is relevant to the temperature field for large temperature gradients and increasing particle sizes. The dimensionless ETC in flow direction according to Vortmeyer et al. [182] is

$$k_{\text{eff},\text{mix}} = \frac{v^2 \rho^2 c_p^2}{\alpha_{\text{eff}} a_{\text{bed}} \lambda_f} \cdot \quad [2.47]$$

The ETC at stagnant fluid  $k_{\text{eff},o}$  incorporates the heat transfer modes of fluid and solid conduction as well as contact conduction and radiation as shown in Figure 2.7. According to van Antwerpen et al. [181], it can be modeled as superposition of a heat conduction and radiation contribution as

$$k_{\text{eff},o} = k_{\text{eff},\text{cond}} + k_{\text{eff},\text{rad}}. \quad [2.48]$$

For the conduction part, the simple approach of a parallel or series connection of the particle and fluid thermal conductivity is often used as upper and lower limit. The particle and fluid thermal conductivity is weighted by the porosity, particle size has no influence. The ETC for a series connection is defined as

$$k_{\text{eff},\text{cond},I} = \left( \varepsilon + \frac{1 - \varepsilon}{k_p} \right)^{-1}, \quad [2.49]$$

and for a parallel connection as

$$k_{\text{eff},\text{cond},II} = \varepsilon + (1 - \varepsilon)k_p. \quad [2.50]$$

Following the approach of Krischer [100] the ETC due to heat conduction may be modeled as superposition of a series and parallel connection

$$k_{\text{eff},\text{cond}} = \left( \frac{B}{k_{\text{eff},\text{cond},I}} + \frac{1 - B}{k_{\text{eff},\text{cond},II}} \right)^{-1}. \quad [2.51]$$

The approach is visualized in Figure 2.8. A value of 0.2 is proposed for the constant  $B$  by Krischer [100].

In order to model the radiant heat transfer according to Fourier's Law only the first derivative with respect to temperature is used. A general form according to [181] is

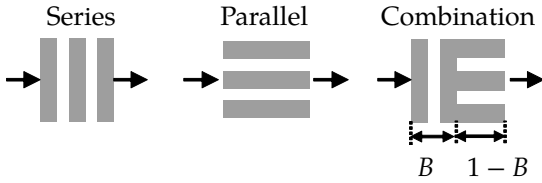


**Figure 2.8 /** Effective thermal conductivity model according to Krischer [100].

$$k_{\text{eff,rad}} = \frac{4F_E(\epsilon, \epsilon, \dots)\sigma T^3 d_{32}}{\lambda_f}. \quad [2.52]$$

The radiation exchange factor  $F_E$  depends at least on the particles emissivity  $\epsilon$  and packed bed porosity [181]. The radiant heat transfer is linearly dependent on the particle size, as radiation may travel further for larger pore spaces. The radiation furthermore leads to a temperature dependency of the ETC.

Widely used correlations for the ETC at stagnant fluid which also account for radiation have been developed by Zehner et al. [200] and Yagi et al. [195].

### Packed-Bed-to-Wall Heat Transfer Coefficient

The packed-bed-to-wall heat transfer coefficient is defined as

$$\alpha_{\text{bed-w}} = \frac{1}{A_w} \frac{\dot{Q}}{\bar{T}_w - \bar{T}_{\text{bed}}}. \quad [2.53]$$

The value of the mean bed temperature  $\bar{T}_{\text{bed}}$  depends on the model spatial discretization. Using two- or three-dimensional packed-bed models, the packed-bed temperature can be resolved up to the wall. Therefore, only a thermal contact resistance directly at the wall remains. It is generally given as correlation of the Nusselt number at stagnant fluid  $\text{Nu}_{w,0}$  and a contribution related to fluid flow depending on the Reynolds and Prandtl numbers [13, section Mg]

$$\text{Nu}_w = \text{Nu}_{w,0} + B_1 \text{Re}^{B_2} \text{Pr}^{B_3}. \quad [2.54]$$

An exemplary correlation has been determined by Nilles [134], further correlations are collected in [59].

In a one-dimensional model on the other hand, only a single mean temperature per flow cross section is determined. Consequently, the temperature profile towards the wall must be accounted for using an additional heat transfer resistance due to the heat transport through the packed bed to the wall  $\alpha_{\text{bed}}$ . The resistances can be superpositioned according to the *VDI Heat Atlas* [13] as

$$\frac{1}{\alpha_{\text{bed-w}}} = \frac{1}{\alpha_w} + \frac{1}{\alpha_{\text{bed}}}. \quad [2.55]$$

But, as the temperature field in packed-bed TES changes significantly over time according to the operation of the storage, this is a dynamic problem and thus no simple correlation can be defined.

Advantageously, packed-bed TES are generally thermally well insulated. In consequence, the difference of the inner insulation surface and packed-bed temperature is small compared to the temperature difference across the thermal insulation.

## Natural Convection

For packed beds with a vertical flow direction and charged from the top, as mainly proposed in literature for TES, natural convection is of low relevance, as the gravity and temperature gradient are unidirectional. For horizontal-flow packed beds, natural convection can be relevant, as it can lead to an upwards advective heat transport and thus an additional vertical temperature profile in the packed bed. The effect is especially critical at long hold operations and in the vicinity of the in- and outlet.

In experiments with a small horizontal-flow packed-bed TES, as reported by Soprani et al. [166], heat tends to accumulate in the upper part of the storage, eventually leaving hot pockets at discharge. Thus, the depth of discharge and usable storage capacity is reduced.

Nevertheless, the advective heat transport due to natural convection in packed beds is limited by the difference in specific heat capacity of the storage material and heat transfer fluid, which is generally large for rock beds with gaseous heat transfer fluid.

Natural convection can be directly accounted for in three-dimensional models of packed beds by means of the gravitational body force, as shown in Equation 2.32. For one-dimensional models in other than the direction of gravity, an additional model for the effect of natural convection is necessary.

The Rayleigh number may be used to characterize the impact of natural convection. It is defined according to Nield et al. [133, page 223] using the thermal expansion coefficient of ideal gas  $1/T$  as

$$\text{Ra}_{\text{bed}} = \frac{-g\rho_f^2\Delta T\Delta zKc_{pf}}{T\mu\lambda_{\text{eff},o}}. \quad [2.56]$$

A model for natural-convection driven horizontal-flow through a packed-bed subjected to an end-to-end temperature difference has been derived by Bejan et al. [22, 23]. A similar model has been proposed by Prenzel [146].

## 2.7 System Simulation with *Modelica*

*Modelica* is an object-oriented and equation-based programming language for the modeling of complex physical and technical systems, owned by the non-profit *Modelica* Association [126]. The real-world system is represented in *Modelica* as a set of differential-algebraic equations, thus dynamic behavior is inherently taken into account. Discrete variables are incorporated by means of event generation. From the equation system a C-code can be automatically generated, which is referred to as model translation. The required solving

algorithm comes with the simulation environment. The C-code can then be used to calculate the evolution of all state variables over time. *Dymola*<sup>®</sup>, owned by Dassault Systemes [44], and its variable time step solver *Sdi rk34hw* was used for the results in this work. An alternative open-source simulation environment is *OpenModelica* [138].

The equations in *Modelica* can be defined non-causal, which means without differentiation between known and unknown variables. It must only be assured, that the number of unknowns and equations match. Furthermore, a model can be composed of sub-model instances, which are linked by interfaces, referred to as connectors in *Modelica*. Connectors are termed physical, if they contain the same number of flow and effort variables. Sub-models and their interconnections can also be displayed graphically, thus visualizing the structure of the model. Further introductory material on *Modelica* is listed on the homepage of the *Modelica* Association [126].

A benefit of standardized interfaces is the replaceability of sub-models. This feature is useful when adopting the level of detail for parts of the overall model to the simulation task. The combination of object-orientation, non-causality and standardized physical interface definitions enables a high reusability of *Modelica* code. Consequently, models can be collected in libraries and shared with other users.

# Chapter 3

## Electric Thermal Energy Storage

In this chapter the ETES system layout and operation principles are explained. Furthermore, an overview on the possible ETES application cases in energy systems with a high share of VRE is given and the state-of-art is outlined. Two important key figures, namely the energy-based ETES efficiency and the packed-bed storage usable capacity ratio, are defined as these will be used to judge the ETES performance for different application cases and unit sizes in Chapter 6. Additionally, the energy losses are listed in order to improve the insight.

### 3.1 System Layout

ETES is a Carnot Battery concept using a packed bed as high-temperature TES, direct electric heating for charge and a conventional water-steam cycle for discharge. Figure 3.1 shows the flow chart of the ETES system. It can be divided into an air cycle and a water-steam cycle.

At charge, air is heated in the electric heater and then flows through the packed bed, directly transferring heat to the storage material. A fan is used to move the air in the closed cycle against the flow resistance of the system.

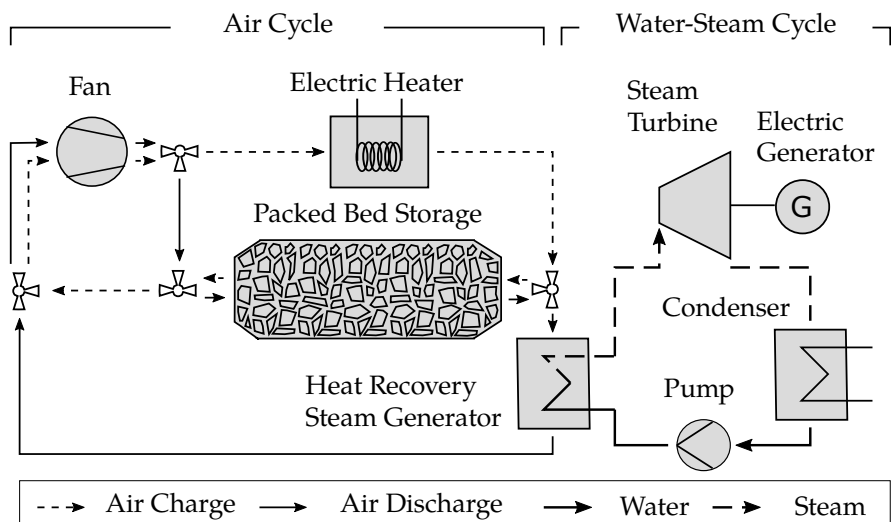


**Figure 3.1 /** Flow chart for Electric Thermal Energy Storage concept.

In order to supply steam to the turbine and generate electricity at discharge, air is moved through the packed-bed storage in opposite flow direction. Passing through the packed-bed pores, the air heats up and subsequently flows to the Heat Recovery Steam Generator (HRSG), where heat is transferred from the air cycle to the water-steam cycle. The HRSG is thus the link between both cycles.

The water-steam cycle is shown here in its most basic configuration. Other water-steam cycle configurations including steam reheating or multiple pressure levels for evaporation are generally feasible in order to improve the efficiency, as the heat is supplied at a higher thermodynamic mean temperature. Feedwater pre-heating with bleed steam also increases the mean temperature of heat supply. However, in the ETES system this might also lead to higher HRSG air outlet and packed-bed storage inlet temperatures at discharge, as the feed water is needed to cool the air. A higher packed-bed storage inlet temperature has a negative effect on the usable storage capacity and air cycle efficiency.

The heat transfer fluid in the packed bed is separate from the heat transfer fluid used in the heat engine cycle. Therefore, the pressure level of the packed-bed

storage can be close to ambient pressure and no pressure resistant containment is necessary, which significantly reduces the storage cost.

The air cycle is closed. Nevertheless, some air has to be exchanged with the environment continuously through vents. This can be explained with the temperature dependency of the enclosed air density. As parts of the ETES system, such as the packed bed or pipe sections, are heated, air has to be released from the system in order to keep the pressure level constant and vice versa, as discussed in more detail by Wang et al. [187].

The achievable ramp rates for the charge and discharge power of the ETES system differ. The heater and fan electric power can be varied from zero to the nominal value in minutes, depending on the specific design. The fan must still run after the heater has been switched off to prevent overheating. On the other hand, the water-steam cycle requires preheating, as large thermal gradients in thick-walled parts are to be avoided [159]. Depending on the HRSG design, the startup may therefore take up to several hours.

## 3.2 Operation

The packed-bed TES in the ETES system is charged and discharged in opposite flow direction with distinct temperatures. These are referred to as nominal charge and discharge temperature  $T_{\text{nom},c}$  and  $T_{\text{nom},d}$ . Consequently, a thermocline evolves in the packed bed and the outlet temperature of the storage can be kept constant for a large portion of the charge and discharge duration. The charge or discharge operation of the TES is stopped as soon as the TES outlet temperature reaches a defined deviation  $\Delta T_c$  or  $\Delta T_d$  from the nominal temperature. The packed-bed storage therefore has a fixed hot and cold side, independent of the current flow direction. Figure 3.2 shows exemplary mean temperatures in the packed bed along the main flow direction at three different points in time.

An operation of the packed-bed TES between the nominal charge and discharge temperature without tolerating a deviation at the respective heat storage outlet for charge or discharge is not possible. Reason is that the thermocline thickness  $\Delta x_{\text{thermocline}}$  grows with time due to packed-bed internal heat transfer, also

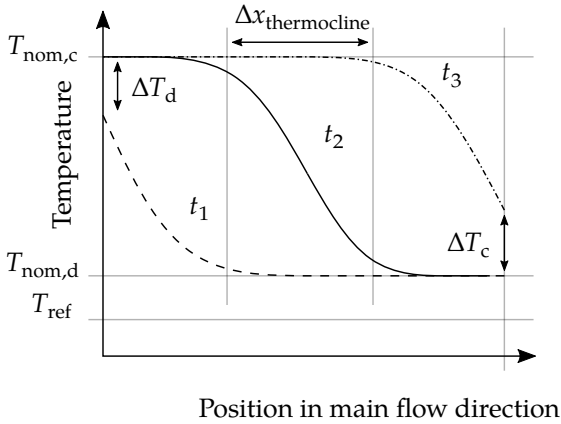


**Figure 3.2 /** Packed-bed temperature along main air flow direction at three different points in time: at the end of full discharge operation ( $t_1$ ), half filled ( $t_2$ ) and at the end of full charge operation ( $t_3$ ).

referred to as thermal destratification. Ultimately, the usable storage capacity would approach zero, as the thermocline thickness approaches the storage length. Decreasing the thermocline thickness by means of the temperature deviation tolerance at the end of charge or discharge avoids this situation [19].

On the other hand, a packed-bed storage outlet temperature deviation as large as the nominal charge and discharge temperature spread in order to maximize the usable storage capacity is not feasible either. One reason is that the rate of charge and discharge of the packed-bed storage depends on the air enthalpy difference across the heat storage, which is obvious when looking at the energy balance of the packed-bed storage unit

$$\frac{\partial U^s}{\partial t} = \dot{m}_{\text{air}}(h_{\text{in}} - h_{\text{out}}) + \dot{Q}_{\text{loss}}. \quad [3.1]$$

In order to keep the charge or discharge power set point, a small temperature and thus enthalpy difference across the TES would necessitate a large air mass flow, leading to high packed-bed pressure loss and fan energy demand. Furthermore, the electric heater would be exposed to high inlet temperatures at charge and the required HRSG air inlet temperature would not be maintainable at discharge.

Consequently, the packed-bed storage has a limited depth of charge and discharge, which depends on the TES outlet temperature and therefore on the temperature distribution in the packed bed.

The nominal charge temperature can be controlled by the fan rotational speed according to the electric heater power at the respective ETES load point. The nominal discharge temperature on the other hand depends on the HRSG air outlet temperature and thus on the water-steam cycle operation and HRSG design.

The live steam parameters should be close to their nominal values during the entire discharge to keep the water-steam cycle efficiency high. Therefore, the HRSG air inlet temperature must be maintained, even for the necessary packed-bed storage outlet temperature deviation at the end of discharge. A way to ensure this is a margin between the nominal TES charging and nominal HRSG air inlet temperature, in which case the HRSG air inlet temperature can be controlled by mixing of the storage outlet air with storage bypass air according to the storage outlet temperature [121]. The flow path through the switched off electric heater can be used as a storage bypass at discharge to reduce the balance of plant cost.

### 3.3 Applications

The ETES system can be used for various purposes in energy systems with a high share of VRE. Besides the basic application as EES, it can also be employed for flexible power-to-heat, cogeneration of heat and power or conversion of existing power plants into energy storage units. Figure 3.3 gives an overview of the different application cases. Combinations are generally worthwhile in order to further improve the benefit to the energy system. The numbers in the text refer to the numbers of Figure 3.3.

The basic ETES application is a standalone EES unit (1), time shifting electricity from wind and solar energy. It consists of an ETES air cycle in combination with a water-steam cycle. The system can be built anywhere, as there are no geographical prerequisites. One example would be an addition to a wind or solar farm, thus enabling the provision of dispatchable renewable energy and

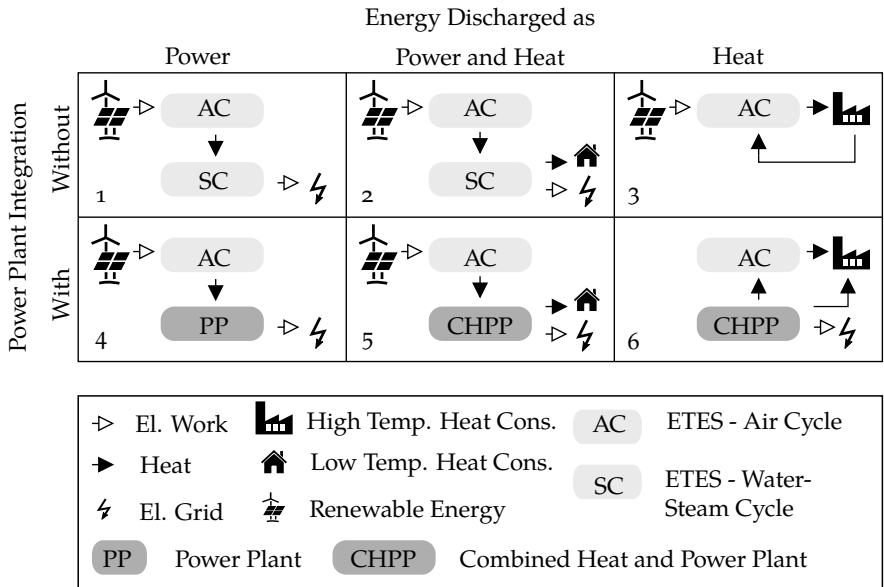


**Figure 3.3 /** Overview on application cases for the ETES concept.

possibly mitigation of either grid congestion or expansion.

Combined heat and power generation at discharge (2) increases the utilization rate of the stored thermal energy. Heat can be supplied to customers during the discharge process by steam extraction or back-pressure operation of the water-steam cycle. As the ETES system is emission-free and has no significant safety concerns, the whole unit may be located close to residential areas, reducing the heat losses and cost associated with the heat network.

The stored thermal energy may also be used to solely provide low-carbon heat from wind and solar energy upon demand (3). The thermal energy storage allows an electricity-led operation in order to provide flexibility to the electricity sector. The feasible temperature range is limited by the maximum storage temperature. Power-to-heat applications do not require a water-steam cycle, which significantly reduces the capital costs compared to power-to-power applications. The heat can be supplied using steam as heat transfer fluid. If applicable, air can be used as heat transfer fluid directly as well, thus eliminating the need for a HRSG. If waste heat is available from the industrial

process above the ETES nominal discharge temperature, it can be recovered and used to replace electric energy at the charge process.

An ETES integration in existing fossil-fueled power plants or combined heat and power plants with water-steam cycles, such as coal-fired or combined-cycle power plants, is beneficial, as the existing water-steam cycle and grid infrastructure may be shared (4 and 5). For coal-fired power plants, only the ETES air cycle including the HRSG has to be added. For combined-cycle power plants even the existing HRSG may be eventually utilized. Essential requirement is a heat storage temperature above the plant's live-steam temperature with added operational margin according to Section 3.2. Smaller sized ETES systems can be integrated in power plants to partly replace energy from fossil fuel combustion with stored renewable energy, to increase the maximum power output or to use the stored heat for water-steam cycle preheating during startup. Ultimately, existing power plants may be turned into EES units, completely eliminating fossil fuel combustion.

Some combined heat and power plants today face the economic challenge of providing contractually guaranteed heat in times of high electricity generation from wind and solar energy and thus low wholesale electricity prices [25]. The ETES system can be used to provide industrial process heat in these time periods (6) in order to enable the power plant to shut down or to avoid the need for additional fossil fuel heat generators. The packed-bed storage can be charged with cogenerated heat from the power plant while at operation.

### 3.4 State of the Art

A major strength of the ETES concept is its use of commercially available components for the charge and discharge processes, especially also in the targeted multi-MW scale. HRSG are used in combined cycle power plants [58]. Electric heaters supply process heat for various industrial applications [114]. The component for which the least operational experience exists is the packed-bed storage.

A first ETES demonstration plant has been commissioned in 2019 in Hamburg, Germany, by Siemens Gamesa Renewable Energy as part of the joint research

Rated Power Heater:	5.4 MW
Rated Power Turbine:	1.4 MW
Thermal Storage Capacity:	130 MWh
Charge Temperature:	750 °C
Live Steam Temperature:	480 °C
Live Steam Pressure:	65 bar
Storage Material Weight:	$1 \times 10^6$ kg

a / Key figures.



b / Front view of plant site.

**Figure 3.4 /** ETES demonstration plant in Hamburg-Altenwerder, Germany.

project *Future Energy Solution* funded by Germany's Sixth Energy Research Program. Figure 3.4 shows the key figures and a picture of the demonstration plant. The packed-bed storage unit and electric heater can be seen upfront, the water-steam cycle is inside the gray building behind. The top part of the air cooled condenser can be seen behind the storage unit.

The demonstration plant incorporates a high-temperature packed-bed thermal energy storage at a larger scale than the experimental setups listed in Section 2.6. Crushed volcanic rock is used as the storage material. The rocks are filled into a concrete containment, the main air flow direction in the packed bed is horizontal. Conventional thermal insulation materials, such as aerated concrete and rock wool, are used to diminish the heat losses at low cost. A grating is used to hold up the packed bed at the hot and cold sides.

### 3.5 Efficiency Definition

The efficiency definition for the ETES system is based on energy rather than power in this work, according to the reasoning in Section 2.2. Energy has been furthermore chosen over exergy as measure for the following reasons.

- The form of discharged energy can be electricity or heat. A higher temperature and thus exergy content of discharged heat is not generally

beneficial, depending on the temperature requirements of the heat application.

- The energetic efficiency of an electric heater does not depend on the temperature level. The exergetic efficiency of the electric heater on the other hand would increase at a higher air inlet temperature, even though the overall ETES system efficiency is not necessarily improved.
- Energetic efficiencies of water-steam cycles at different system parameters are well documented in literature.

The ETES efficiency has to be defined differently for power-to-power and power-to-heat operation according to the form of discharged energy. A second important reason is that the electric work intake at discharge, mainly to operate the fan, has to be valued differently. At power-to-heat operation, it can be just added to the electric work intake at charge and hold, as discharge operations not necessarily occur in times of high electricity value. Thus, no differentiation between operational modes is needed. At power-to-power operation on the other hand, the electricity self-consumption at discharge has to be provided from the stored energy. Hence, the discharged electricity is the difference of the electricity generated by the steam cycle and the self-consumption of the air cycle. Otherwise, no just comparison of storage technologies is feasible, as the value of electricity at discharge of EES units is generally higher than the value at charge.

The ETES round-trip efficiency at power-to-power operation is defined with the electric work intake at charge and hold  $W_{el,c} + W_{el,h}$  and the electric work output at discharge  $W_{el,d}$  as

$$\eta_{p2p} = \frac{|W_{el,d}|}{W_{el,c} + W_{el,h}} \quad [3.2]$$

At power-to-heat operation, the ETES efficiency is defined using the electric work intake in the overall observation time period  $W_{el}$  and the heat transferred to the water-steam cycle  $Q_{sg}$

$$\eta_{p2h} = \frac{|Q_{sg}|}{W_{el}} \quad [3.3]$$

It is also denoted as air cycle efficiency  $\eta_{ac}$ , as no water-steam cycle is necessary at power-to-heat operation. The heat transferred with the HRSG in the overall observation time period is defined as

$$Q_{sg} = \int (\dot{m}_{\text{steam,out}} h_{\text{steam,out}} - \dot{m}_{\text{fw,in}} h_{\text{fw,in}}) dt. \quad [3.4]$$

In the case of power-to-power operation it is useful to detach the water-steam cycle efficiency  $\eta_{sc}$  from the air cycle efficiency  $\eta_{ac}$  for two reasons:

1. The air cycle efficiency is yet uncertain, whereas water-steam cycle efficiencies are well documented in literature.
2. The air cycle efficiency is sensitive to the application case and especially operational schedule due to self-discharge of the storage unit and standby losses. Furthermore, the transient behavior during operation, which is mainly a consequence of changes in the packed-bed storage temperature field, must be taken into account. The water-steam cycle on the other hand is only used at discharge and dynamic effects are significantly faster compared to the storage temperature field. Consequently, the water-steam cycle can be simplified as quasi-stationary process, whereas the air cycle can't.

According to Spliethoff [167, page 209], efficiencies of advanced modern steam power plants are at 35 to 47%, eventually reaching above 50% in the future.

For an initial guess of the water-steam cycle efficiency, the Curzon-Ahlborn efficiency may be alternatively used

$$\eta = 1 - \left( \frac{T_{\text{sink}}}{T_{\text{source}}} \right)^{\frac{1}{2}}, \quad [3.5]$$

as also proposed by Thess [174] for a simple mathematical model of PTES systems. It solely depends on the heat source and sink temperatures and can thus be used as easily as the Carnot efficiency. It is derived as the efficiency of a Carnot engine at maximum power output and correlates well with measured power-plant efficiencies [41]. For the live steam temperature of the demon-

station plant, as stated in Figure 3.4a, and a heat sink temperature of 20 °C, it is 0.38.

In order to increase the precision and take part-load operation into account, the water-steam cycle efficiency can be modeled as performance table depending on the boundary conditions.

With the net work of the water-steam cycle  $W_{el,net,sc}$  and the electric work of the air cycle at discharge  $W_{el,d,ac}$ , the overall ETES electric work at discharge  $W_{el,d}$  is

$$|W_{el,d}| = |W_{el,net,sc}| - |W_{el,d,ac}|. \quad [3.6]$$

Thus, the ETES round-trip efficiency at power-to-power operation can be written as product of the air cycle and water-steam cycle efficiencies according to

$$\eta_{p2p} = \frac{\overbrace{|Q_{sg}| - \frac{1}{\eta_{sc}} |W_{el,d,ac}|}^{\eta_{ac}}}{W_{el,c,ac} + W_{el,h,ac}} \cdot \frac{\overbrace{|W_{el,net,sc}|}^{\eta_{sc}}}{|Q_{sg}|}. \quad [3.7]$$

In summary, the air cycle efficiency in power-to-power and power-to-heat operation are

$$\eta_{ac,p2p} = \frac{|Q_{sg}| - \frac{1}{\eta_{sc}} |W_{el,d,ac}|}{W_{el,c,ac} + W_{el,h,ac}} \quad \text{and} \quad \eta_{ac,p2h} = \frac{|Q_{sg}|}{W_{el}}. \quad [3.8]$$

## 3.6 Usable Capacity Ratio

Besides the efficiency, the packed-bed usable capacity ratio is another key performance indicator. It results from the limited depth of charge and discharge of packed-bed TES. Reason is the

- thermocline inside the packed bed, which occupies a portion of the packed-bed volume according to the internal heat transfer characteristics and the
- necessary termination of charge and discharge operation at the defined packed-bed outlet deviation tolerance from the nominal charge or discharge temperature, as explained in Section 3.2.

Thus, the minimum and maximum limit of the stored internal energy  $U^s$  depend on the temperature distribution. A nominal thermal storage capacity is therefore defined in this work with spatially constant temperatures in the packed bed as

$$\Delta U_{\text{nom}}^s = U^s(T = T_{\text{nom},c}) - U^s(T = T_{\text{ref}}). \quad [3.9]$$

The reference state is set arbitrarily at a temperature of  $T = 293.15$  K for the results of this work. The SOC is defined with this reference state as well

$$\text{SOC} = \frac{U^s - U_{\text{ref}}^s}{\Delta U_{\text{nom}}^s}. \quad [3.10]$$

The depth of charge and discharge can be quantified by means of the usable capacity ratio, as defined in Equation 2.6. It is also denoted as material efficiency [140] or utilization rate [29] in literature. An overview on different possible definitions is given by Haller et al. [70] with the background of hot water storage, but these may also be applied to packed beds.

Figure 3.5 illustrates the usable capacity ratio for the special case of an axial-flow packed bed with constant cross section, no lateral porosity and temperature variation as well as constant specific heat capacities. The nominal thermal storage capacity is illustrated in Figure 3.5 as  $A_2$  and the usable capacity as  $A_1$ . As shown, the usable capacity ratio as defined in this work also depends on the nominal discharge temperature, and thus on the HRSG air outlet and feed water temperature. Feed water preheating in order to increase the water-steam cycle efficiency therefore reduces the usable capacity ratio.

For packed-bed TES, the usable capacity ratio changes over time. Thus, a mean

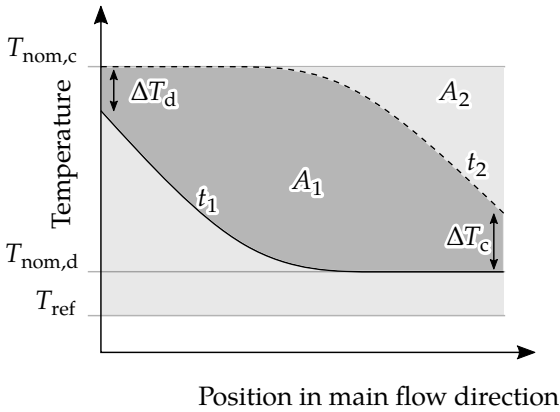


**Figure 3.5 /** Packed-bed temperature along main air flow direction for an “empty” ( $t_1$ ) and “full” ( $t_2$ ) storage unit. In the case of an axial-flow packed bed with constant cross section, no lateral porosity and temperature variation as well as constant specific heat capacities, the usable capacity ratio is  $\varphi = A_1/A_2$ .

value in an observation time period is defined in this work from the average SOC value at all points of time in the period  $t_i$ , when an outlet temperature deviation tolerance is about to get violated and thus the storage operational mode changes

$$\bar{\varphi} = \overline{\text{SOC}}(\forall t_i, T_{s,cs} = T_{\text{nom},c} + \Delta T_c) - \overline{\text{SOC}}(\forall t_i, T_{s,hs} = T_{\text{nom},d} - \Delta T_d). \quad [3.11]$$

Besides the ETES air cycle and packed-bed storage design, the mean usable capacity ratio depends on the system operational schedule. A long hold operation for example reduces the available depth of discharge, as the thermocline thickness increases and the TES outlet temperature deviation tolerance will be exceeded earlier in a consequent discharge. Nevertheless, for a cyclic operation, which is a consecutive charge and discharge operation up to a fixed outlet temperature deviation tolerance, the usable capacity ratio approaches a design-specific limit [74, 121]. This limit can be used to compare the usable capacity ratio for different designs.

The usable capacity ratio has an important effect on the storage unit energy turnover in an observation time period. According to Section 2.2, the energy turnover can be quantified using the number of equivalent full cycles. Besides the usable capacity ratio, the number of equivalent full cycles also depends on the operation of the storage unit. In the case of an ETES unit, the definition

of the number of equivalent full cycles is different at power-to-power and power-to-heat operation, as for the efficiency. It is defined in accordance with Equation 2.10 as

$$n_{\text{efc,p2p}} = \frac{W_{\text{el,c,ac}} + W_{\text{el,h,ac}}}{\Delta E_{\text{nom}}^{\text{s}}} \quad \text{and} \quad n_{\text{efc,p2h}} = \frac{W_{\text{el}}}{\Delta E_{\text{nom}}^{\text{s}}}. \quad [3.12]$$

The temperature deviation tolerance at the end of charge and discharge can be used to control the usable capacity ratio. Generally, the closed ETES system allows larger tolerances compared to open systems, as the outlet air enthalpy is not lost. Furthermore, an increase of fan work due to an increasing storage outlet temperature at charge has negligible consequence on the ETES efficiency, as will be shown in Section 3.7. Nevertheless, at discharge, the required HRSG air inlet temperature limits the available deviation tolerance and an increase in fan work according to a raise in air mass flow decreases the ETES efficiency.

The limited depth of charge and discharge can be compensated by over-sizing of the packed bed. But this leads to additional capital cost as well as packed-bed storage heat and pressure losses and thus lowers the ETES efficiency. Consequently an application case specific design optimization is required, which can be done by numerical simulation.

### 3.7 Classification of Air Cycle Energy Losses

A general energy balance for the ETES air cycle is used to classify the different energy loss contributions. This classification is used in Section 6.7 to evaluate the relevance of these energy loss mechanism on the overall ETES performance for several test cases.

The system boundary includes all components of the air cycle. The energy balance integrated over the observation time period is

$$\Delta U = W_{\text{el}} - W_{\text{el,sby}} - W_{\text{el,loss,eh}} - W_{\text{el,loss,fan}} - Q_{\text{sg}} + Q_{\text{loss}} + H_{\text{loss}}. \quad [3.13]$$

The internal energy difference  $\Delta U$  is mainly stored in the packed-bed. Nevertheless, significant amounts of thermal energy may also be stored in the piping material or the other components of the air cycle. The internal energy difference can be significant for short observation time periods, but in relation to the charged and discharged energy it tends towards zero with increasing observation time, as the amount of charged and discharged energy grows. It is difficult to measure, as all system components may contribute to it, and can be misleading when comparing different experimental results. Therefore, it should be kept as small as possible in order to allow comparison among experiments.

The overall electricity intake of the air cycle is denoted as  $W_{el}$ . It is subtracted by the electric work needed to cover the standby losses  $W_{el,sby}$ , as this electric work does not contribute to the air cycle internal energy. Similarly, energy conversion losses of the electric heater and fan unit  $W_{el,loss,eh} + W_{el,loss,fan}$  are subtracted, as these dissipate into heat and get transferred to the environment directly as well. In the fan case, these losses equal the difference between electric motor energy intake and technical work fed into the air cycle, for example due to friction losses in the motor. Transformer losses are one contribution in the electric heater case.

$Q_{sg}$  is the heat transferred to the water-steam cycle in the HRSG. The overall thermal losses of the air cycle are subdivided into transmission heat losses  $Q_{loss}$  through the thermal insulation of all air cycle components and intentional venting or air leakage losses  $H_{loss}$  due to an air mass flow to or from the environment.

A combination of Equations 3.7 and 3.13 leads to

$$\eta_{ac} = 1 - \frac{\Delta U - Q_{loss} + \left(\frac{1}{\eta_{sc}} - 1\right)W_{el,d} - H_{loss} + W_{el,sby} + W_{el,loss,eh+fan}}{W_{el,c} + W_{el,h}}. \quad [3.14]$$

Using this equation, the different loss mechanism of the ETES air cycle in power-to-power operation can be classified as:

1. Transmission heat loss of the air cycle to the environment  $|Q_{loss}|$ ,

2. Conversion loss in the water-steam cycle, when generating the electricity demand of the air cycle at discharge  $\left(\frac{1}{\eta_{sc}} - 1\right)W_{el,d}$
3. Ventilation loss  $|H_{loss}|$ , when air is leaving or entering the air system due to leakage or intentional venting,
4. Standby loss  $W_{el,sby}$  and
5. Conversion loss of the electric heater and fan unit  $W_{el,loss,eh+fan}$ .

Notably, the technical fan work needed to circulate the air at charge does not appear as a loss mechanism in an energy-based analysis. Furthermore, at discharge, only the conversion loss in the water-steam cycle at generation of the electric work demand needed to cover the technical fan work appears as energy loss. This is due to the fact that the fan work dissipates into heat just as the electric work intake of the heater and is supplied to the TES. This observation is an interesting primary result of the analysis, as it has consequences on the optimal ETES design. But it is restricted to packed-bed TES operation in a closed cycle, as in the case of the ETES concept.

The transmission heat losses include the packed-bed storage in the first place, but the losses from piping and other system components can also be significant, especially for the high temperature system part.

At power-to-heat operation, a corresponding combination of Equations 3.3 and 3.13 leads to

$$\eta_{p2h} = 1 - \frac{\Delta U - Q_{loss} - H_{loss} + W_{el,sby} + W_{el,loss,eh+fan}}{W_{el}}. \quad [3.15]$$

In this case, the electricity demand at discharge does not appear as a loss mechanism, as the work is included in the denominator.

# Chapter 4

## Simulation Method

In this chapter the used simulation methodology is explained. An overview is given at first, introducing three different modeling scales. Then, each scale is described in detail, one per section.

### 4.1 Overview on Multi-Scale Simulation

A multi-scale simulation procedure has been developed for the analysis of the ETES concept in this work. It is illustrated in Figure 4.1.

**System Simulation** is used to evaluate the ETES performance for different designs and application cases under realistic operation conditions. The dynamic model includes all ETES components, such as the packed-bed storage, fan, electric heater, HRSG, piping and control system and covers all relevant loss mechanism. A long simulation time is targeted in order to get a good representation of realistic operation and correctly account for the self-discharge losses. To reduce the computational effort and to allow sensibility analysis and parameter variations for the ETES system in reasonable real time, the packed bed is solely discretized in the main flow direction and uses the porous-media assumption according to Section 2.6.2.

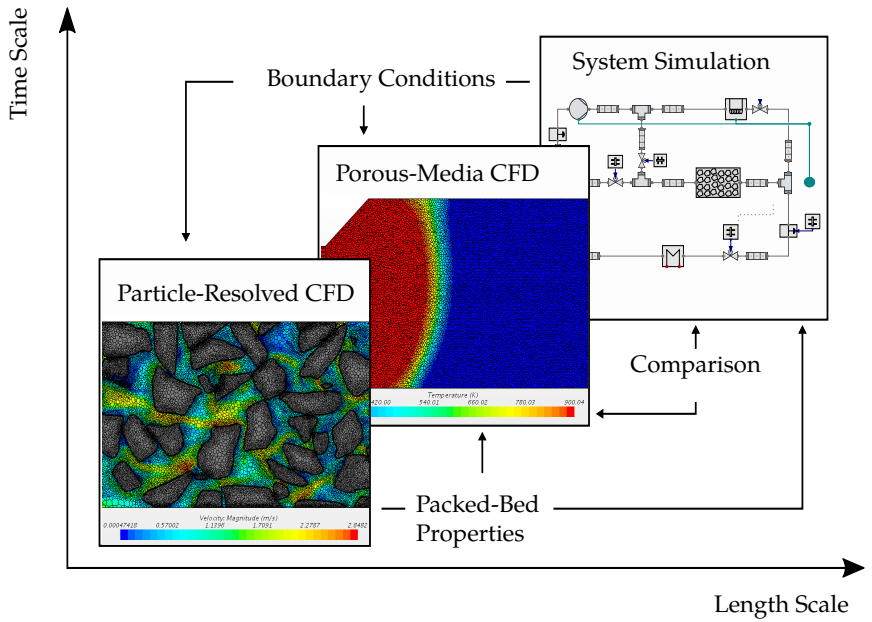


Figure 4.1 / Overview on multi-scale workflow.

**Porous-Media CFD Simulation** is applied to further investigate the three-dimensional temperature and flow field in the packed-bed using the finite-volume approach and the assumption of a continuously distributed porous medium. Reason is that three-dimensional flow effects, such as for example natural convection or uneven flow due to temperature-induced density variations inside the packed bed, are observable in packed-bed TES and the dependency of these effects on the packed-bed properties, storage unit size and operational conditions is not completely clear. The CFD results are thus compared to the results of the one-dimensional system simulation packed-bed model for simulation times of several days to weeks in order to reveal deviations at the exact same boundary conditions and storage designs.

**Particle-Resolved CFD Simulation** is used to determine the packed-bed properties, as introduced in Section 2.6.2 for the one- and three-dimensional packed-bed models. All properties are determined with stationary and three-dimensional finite-volume CFD simulations. The necessary range of validity for the correlations is set by the operating range of the packed-bed storage. The numerical approach leads to a significant cost reduction due to the large number of required experiments, if many different particle shapes, size distributions and materials shall be tested. A small representative subset of the packed bed is numerically generated with the Discrete Element Method (DEM) as computational volume for the CFD simulation, containing approximately 1000 particles.

## 4.2 System Simulation

In order to evaluate the ETES performance for different designs and application cases under realistic operating conditions, system simulation models have been developed in the *Modelica*-language. A dynamic approach has been chosen in order to consider the time-variant temperature field inside the packed bed, which strongly affects the overall ETES system performance, as for example

- the packed-bed outlet temperature at low states of charge is reduced by thermal destratification due to internal heat transfer, especially during long hold operations, and

- the energy demand of the fan is mainly caused by the temperature-dependent packed-bed pressure loss.

The equations used to describe the ETES system follow physical laws, such as the conservation of mass, momentum and energy or Fourier's Law. Therefore, the parameters of the model have intuitive physical meanings and can be generally determined from measurements. Advantages of this physical modeling approach are an easier interpretation of the simulation results and the applicability of the model to ETES units of different scale, as long as the range of validity for the used set of physical laws is not violated.

As introduced in Section 2.7, the object-orientation of *Modelica* enables the utilization of existing model libraries. The system simulation in this work is especially based on the libraries *TransiEnt* and *ClaRa*.

**TransiEnt Library** originates from the research projects *Transient.EE* and *Resilient.EE* and is open-source [71]. The library enables dynamic system simulation of integrated energy systems with high shares of renewable energy [11]. It contains component models in different level of detail for generation, transmission and consumption in the electricity, heat and gas sector, such as PV and WEC plants, heat- and electricity consumers or electricity and heat networks. The component models for the one-dimensional packed-bed storage, HRSG, electric heater and fan, as described in Section 4.2, are included in version 1.4 of the library. Due to the compatibility of the models with the *TransiEnt Library*, many different ETES application cases, including cross-sector storage options, can be analyzed.

**ClaRa Library** originates from the *Dyncap* and *Dynstart* research projects, and is open-source as well [72]. It contains component models for the physical and dynamic modeling of water-steam cycles. The finite volume representations for fluid and solid media of this work as well as the controllers have been instantiated from the library. A finite volume representation for gas media with a dynamic momentum balance, as needed for this work, is added to version 1.6 of the library. The compatibility with the *ClaRa Library* allows to investigate an ETES integration into steam power plants, taking into account transient plant behavior.

Further libraries used in this work are the

- subset of the *TILMedia Suite* [176], as included in the *ClaRa Library*, to provide the air and water media properties for the system simulation as external C-code, the
- *Modelica State Graph 2* [50] to model the state graph controller of the air cycle and the
- *Modelica Standard Library* [127] to provide several basic models for the system simulation.

### 4.2.1 Application Case Models

The application case models define the integration of an ETES unit into the surrounding energy system, in order to impose realistic boundary conditions for the ETES units.

The ETES air cycle and water-steam cycle are modeled as two separate units. Reasons for the separation are:

1. The ETES integration in existing water-steam cycle power plants and the application as power-to-heat unit only require the air cycle, as illustrated in Figure 3.3. Due to the model separation, similar air cycle models can be used for these application cases and EES units.
2. The advantages of a separate air- and water-steam cycle efficiency analysis, as already reasoned in Section 3.5.
3. The water-steam cycle can be simplified as quasi-stationary process, whereas the transient behavior of the air cycle must be taken into account.

The HRSG is included in the air cycle. Thus, the ETES air cycle is a technical system, which can generate steam by means of electric energy, including the option to store the thermal energy intermediately.

Figure 4.2 shows *Modelica*-diagrams for the system simulation models of two different exemplary ETES applications cases. The left side shows the ETES air cycle application as power-to-heat unit for an industrial process and the right side the application as standalone EES in combination with a water-steam

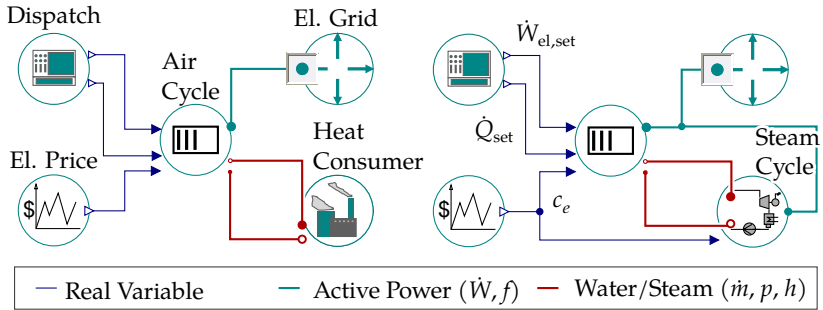


**Figure 4.2 /** Examples of ETES air cycle system integration as power-to-heat unit (left) and standalone EES with a water-steam cycle (right) in *Modelica*. Components and their connections are only labeled once.

cycle.

The ETES air cycle model is connected to the electricity grid with a physical power connector, taken from the *TransiEnt Library*. The heat consumer and water-steam cycle are connected to the air cycle with physical fluid connectors to correctly account for the temperature at heat transfer inside the HRSG. In the dispatch model, the set-point values for the electric power intake and heat flow output of the air cycle are defined according to the operational schedule. The electricity price is furthermore needed as time series data in order to calculate the charging cost for the air cycle.

## 4.2.2 Air Cycle Model

Figure 4.3 shows the *Modelica*-representation of the ETES air cycle flow chart, which is the content of the air cycle icon in Figure 4.2. Accordingly, the connectors match the ones of the icon. The simulation model for the air cycle is hierarchically structured on two levels, which are the

1. air cycle subsystem model, which defines the system layout and instantiates the
2. component models.

Besides the main component models for the packed-bed storage, electric heater, HRSG and fan, the air cycle model includes pipes, junctions, valves, controller, an aggregated standby consumer, an air medium model and a cost model.

The cost model does the calculation of the LCOS, as defined in Equation 2.14, depending on the electricity price data. The annuity method according to the *TransiEnt Library* and the Association of German Engineers [12] is used to account for the capital cost. The operation & maintenance cost is simplified as fixed annual fraction of the capital cost.

The air medium is represented by means of the external C-code provided by the *TILMedia Suite* subset within the *ClaRa Library*. The air flow is discretized in one dimension for all components using finite volumes and a staggered grid, as further explained in the *ClaRa Library Documentation* [73].

The vent upstream of the fan, which is denoted as cold vent in Figure 4.3, is included to keep the pressure level in the closed system constant, as already mentioned in Section 3.1. Consequently, the pressure level upstream of the fan always equals the ambient pressure. The vent upstream of the HRSG, denoted as hot vent, is included in order to prevent an HRSG air inlet temperature above the allowance at a load point change from charge to discharge by releasing hot air from the pipe section.

A challenge to the numerically robust simulation of the shown closed fluid cycle in *Modelica* is the flow reversal at times of operation mode changes from charge to discharge or vice versa. Furthermore, the physical mass flow is close to zero in the packed bed at hold. A common approach to improve the simulation robustness of such systems is a limitation of the mass flow magnitude to values above a small non-zero value. But, for the packed-bed storage, even small mass flows would lead to a significant incorrect energy transport over long hold periods. The introduction of dynamic momentum balances for each finite fluid control volume has been found to solve the problem. But it comes at the cost of additional state variables.

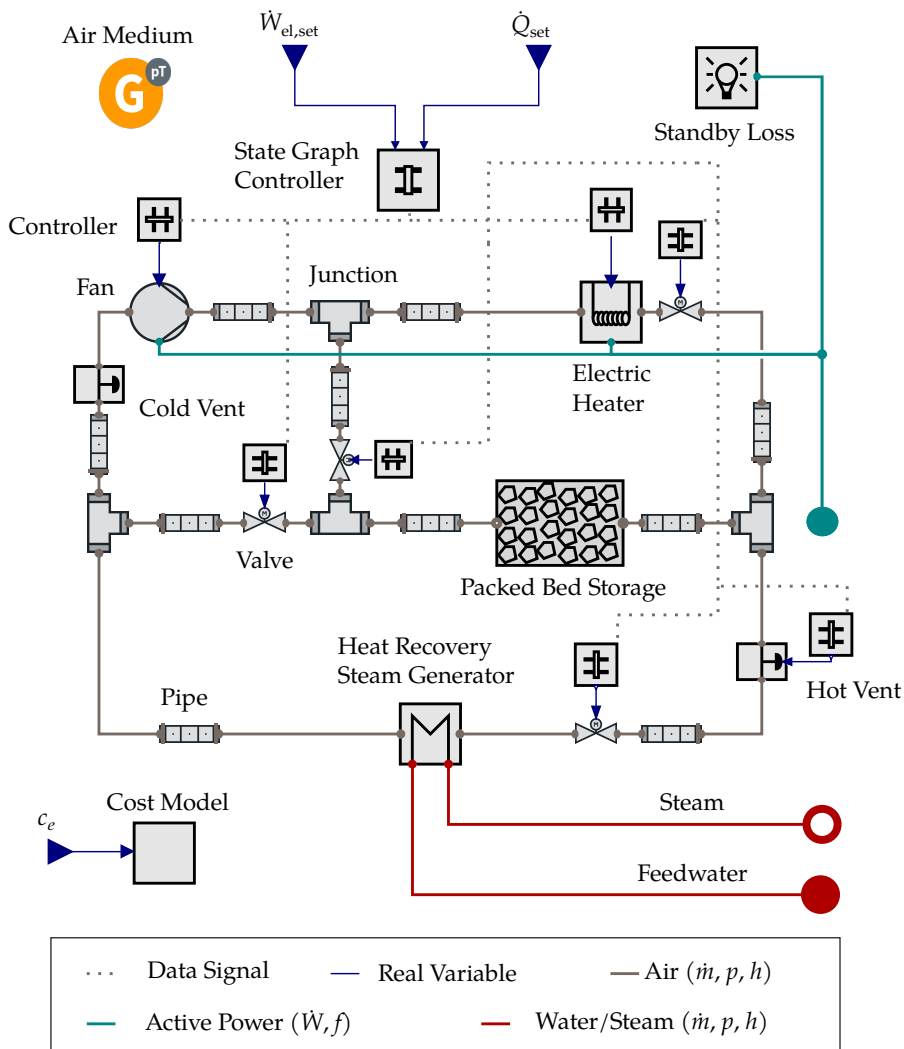


Figure 4.3 / Diagram of the ETES air cycle model.

## Control System

The control system consists of the state graph controller and further units for the electric heater power, fan power and valve openings. The control units are different for power-to-heat and power-to-power operation of the air cycle. Reason is, that for a power-to-heat application of the air cycle, a simultaneous operation of the electric heater and HRSG is beneficial to cover a heat demand in times of high VRE generation. The storage may be additionally charged or discharged according to the relation of current heat demand and VRE availability.

The state graph used at power-to-power operation is shown exemplary in Figure 4.4. The initial state is hold. For an electric power set-point above a minimum value, the operation mode can change from hold to charge. At charge, the electric heater outlet temperature is controlled by the fan power using a PI-controller. If the storage outlet temperature exceeds the allowed deviation from the nominal discharge temperature or the power set-point falls below the minimum value, a down charge state is active as long as the electric heater outlet temperature is above a defined threshold.

At discharge, the valve opening in the bypass of the packed-bed storage through the electric heater is used to control the HRSG inlet temperature with a PI-controller. At operation point changes, a limit on the temporal gradient of the HRSG air inlet temperature has to be obeyed. Therefore, the HRSG air inlet temperature set-point is defined as linear ramp with a fixed temporal gradient from the current temperature to the set-point temperature in the PI-controller for the up and down discharge state. A second PI-controller is used to control the rate of heat transfer in the HRSG by means of the fan rotational speed and thus air mass flow.

The state graph controller furthermore contains an algorithm to prevent a temperature field in the storage, which would not allow any further operation, as the allowed storage outlet temperature deviations are both violated. Therefore, the charge and discharge potentials of the packed-bed storage are estimated from the temperature field and monitored. If their sum falls below a defined threshold in relation to the nominal thermal storage capacity, the storage will be consequently fully charged or discharged until the estimated charge and discharge potentials recover.

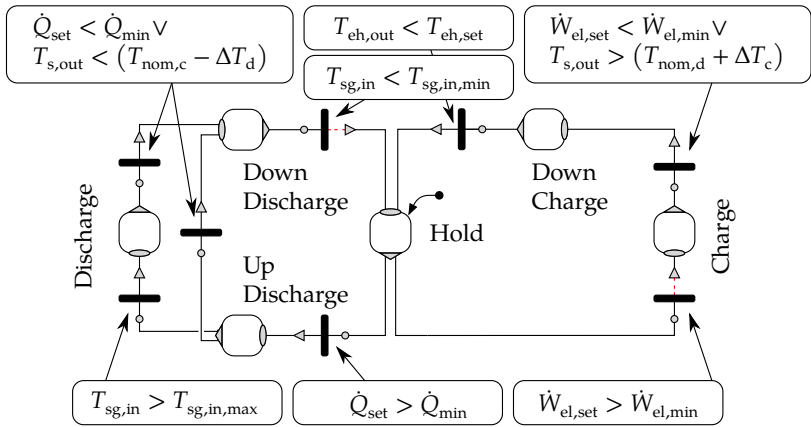


**Figure 4.4** / Diagram of the state graph controller model for power-to-power operation of the ETES air cycle.

### 4.2.3 One-Dimensional Model of Packed-Bed Storage

Besides the representation of the packed bed, the packed-bed storage model further includes air volumes on the hot and cold side of the packed bed as well as the thermal insulation. The model diagram is shown in Figure 4.5. All sub-models are further explained in the following.

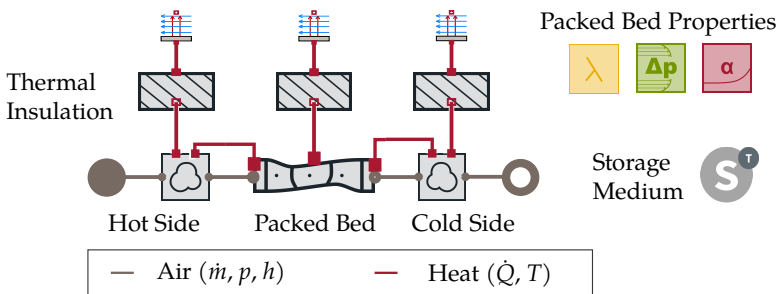


**Figure 4.5** / Diagram of the one-dimensional packed-bed storage model.

## Packed Bed

The packed-bed is only discretized in the main flow direction of the storage unit. Thus no lateral porosity, temperature or velocity variations are taken into account. The porosity is also constant along the main flow direction. The storage cross section along the flow direction is variable and completely filled with rocks. Accordingly, no fluid can bypass the packed bed. The mean volume-equivalent diameter and mean sphericity are used to set the particles surface area according to Section 2.6.2.

A finite-volume formulation of Equation 2.28 is used as mass balance. The packed-bed pressure loss is modeled using an additional body force according to Equation 2.30 in the dynamic free-flow momentum balance of the *ClaRa Library*. According to the packed-bed storage design with a horizontal main air flow direction, as generally used in this work, no gravitational force is taken into account. The permeability and inertial coefficient can be chosen according to the following correlations:

1. Empirical correlation of Ergun [57],
2. Correlation according to Macdonald et al. [115] and
3. Equation 4.19, with constants determined from particle-resolved CFD simulation.

The correlations of Allen et al. [6], which are used at validation of the particle-resolved CFD simulation, are not implemented, as they are not fully in accordance with the approach of Equation 2.30. The one-equation energy balance, which is Equation 2.36 in this work, is used in the model due to the better numerical robustness and faster computation in comparison with the two-equation model. In the one-equation model only the ETC is left as parameter to effect the internal heat flow besides the advection, which simplifies the model verification. The implemented ETC correlations are:

1. A parallel connection of the particle and fluid thermal conductivity according to the porosity, as defined in Equation 2.50.
2. The correlation of Zehner et al. [200] for the ETC at stagnant fluid, optionally added by further correlations from the *VDI Heat Atlas* [13, section Mh] for the flow-related contribution.
3. Equation 4.23 with constants determined from particle-resolved CFD

simulation; the effect of the limited particle-to-fluid heat transfer is taken into account by means of the flow-related ETC according to the derivation of Vortmeyer et al. [182], as outlined in Section 2.6.2.

The packed-bed-to-wall heat transfer coefficient for a one-dimensional packed-bed model should depend on the lateral temperature profile, as stated in Section 2.6.2. But due to the dynamic temperature field inside the packed-bed storage, no simple static correlation can be defined. Nevertheless, several correlations are implemented:

1. Correlation according to Beek [21], as it has been used for a one-dimensional packed-bed model by Hänchen et al. [74].
2. Correlation of Rohsenow et al. [150], as shown in [133, page 80], which is valid for a fully developed temperature profile.
3. Correlation of Schlünder [156] as described in the *VDI Heat Atlas* [13, section Mh], which only accounts for the contact resistance at the wall.

According to the good thermal insulation of the packed-bed storage, the overall heat transfer to the environment is dominated by the thermal resistance of the insulation material and the packed-bed-to-wall heat transfer coefficient plays a secondary role. Thus, for the model validation and the results shown in Chapter 6 an ideal heat transfer between the packed bed and the inner insulation surface is assumed.

An additional heat transfer at the packed bed entrance due to natural convection can be accounted for using a correlation for the packed-bed-to-air heat transfer coefficient. The correlation of Bejan [22], as defined in [133, page 370], has been implemented. As the one-dimensional discretization of the packed-bed model requires an assignment of the transferred heat to the finite volumes, the natural-convection penetration length parameter must be corrected for each design in several iteration steps, as it is necessary for the initial assignment, but depends on the Rayleigh number. In order to reduce the computational time, natural convection at the packed bed in- and outlet is thus not taken into account in the one-dimensional packed-bed model for the results of this work. Conversely, simulation results of the three-dimensional packed-bed model are used to monitor the effect of natural convection.

The internal thermal energy of the packed-bed storage is determined by sum-

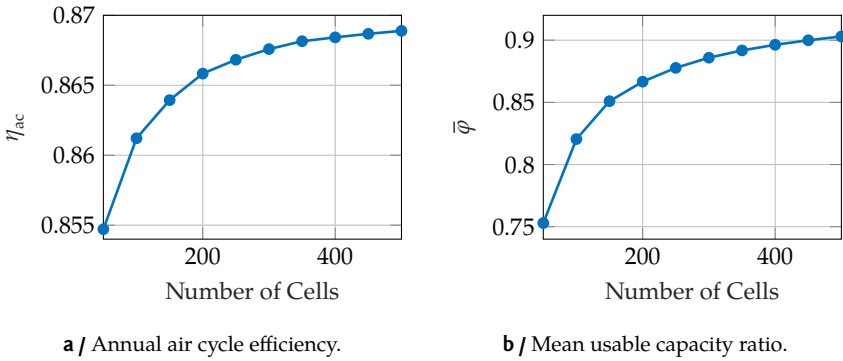


**Figure 4.6 /** Sensitivity of annual air cycle efficiency and mean usable capacity ratio to the number of packed-bed control volumes for a 30 MW ETES unit .

mation of each finite volume's value

$$U_{bed} = \sum_{i=1}^n \rho_p (1 - \varepsilon) u_{p,i} V_i, \quad [4.1]$$

neglecting the air internal energy and using the storage material internal energy  $u_p$  as defined in Equation 4.2.

Figure 4.6 shows exemplary simulation results for the air cycle efficiency and mean usable capacity ratio according to Equations 3.7 and 3.11 for a 30 MW ETES unit. In order to limit the computational time, 300 cells are used for the validation and simulation results in this work. Notably, a higher discretization generally leads to an improved efficiency and usable capacity ratio.

## Storage Medium

The temperature dependency of the storage material's specific heat capacity and thermal conductivity must be taken into account, according to the large temperature variations [8]. Thus, the basic solid medium class of the *TILMedia Suite* is extended with a specific internal thermal energy property

**Table 4.1** / Thermodynamic storage material's properties as used for the results of this work. The constants in Equation 4.3 for the specific heat capacity  $c_p$  and Equation 4.4 for the thermal conductivity  $\lambda$  are determined by curve fitting of data for french basalt from Nahhas et al. [132]. The density  $\rho$  is also taken from this data and the materials emissivity  $\epsilon$  is set according to Zanganeh et al. [198].

$\rho$ kg/m <sup>3</sup>	$\epsilon$	$c_p$ in J/(kg K)			$\lambda$ in W/(m K)	
		$B_1$	$B_2$	$B_3$	$B_4$	$B_5$
2960	0.85	989	0.0658	$-2.74 \times 10^7$	0.4	$-2.68 \times 10^{-5}$

$$u_p = \int_{T_{\text{ref}}}^T c_p(T) dT. \quad [4.2]$$

When fitting the storage material's specific heat capacity with a polynomial in the general form of

$$c_p = B_1 + B_2 T + B_3 T^{-2}, \quad [4.3]$$

the specific internal thermal energy can be determined using the indefinite integral of the polynomial. The general form of Equation 4.3 is chosen according to Maier et al. [116], as also used by other authors, such as Waples et al. [189].

The thermal conductivity is also modeled as polynomial. The general form is chosen according to Mottaghy et al. [130]

$$\lambda = (B_4 + B_5 T)^{-1}. \quad [4.4]$$

As natural rock is used as storage material, the properties vary significantly for different rock types and quarries. For the results of Chapter 6, data from Nahhas et al. [132] is used, which is shown in Table 4.1. Measured data provided by Siemens Gamesa Renewable Energy is used at validation.

## Hot and Cold Side Air Volumes

The hot and cold side air volumes are included in the storage model mainly to take the change of flow cross section from the pipe connection to the packed bed entrance and the resulting pressure loss into account. The significant change of flow cross section results from the design imperative of low air velocities inside the packed bed in order to reduce the fan energy demand. The air volumes at the hot and cold side furthermore contain a heat connector besides the flow connector to the packed-bed. Whereas the flow connector takes the one-dimensional advective heat transport into account, the additional heat connector is added for further heat transport modes. Examples are thermal radiation of the packed-bed surface or a natural convection eddy through the packed-bed entrance during hold operation.

The air volumes on the hot and cold side use dynamic mass, momentum and energy balances for a single control volume. The volume and heat transfer areas need to be specified as geometry parameters. Alternatively, predefined geometries, such as truncated pyramids, may be used. The material mass and heat capacity for the structure can be specified to account for its thermal inertia. Heat transfer coefficients can be selected for the air-to-wall and air-to-packed-bed heat transfer.

The additional pressure loss at in- and outflow of the storage is modeled as

$$\Delta p = \frac{\rho}{\rho_{\text{nom}}} \left( \frac{v}{v_{\text{nom}}} \right)^2 \Delta p_{\text{nom}}. \quad [4.5]$$

It is parameterized using the pressure loss  $\Delta p_{\text{nom}}$  at the nominal density and air velocity.

## Thermal Insulation

The thermal insulation is decisive for the packed-bed storage heat loss, which strongly affects the ETES efficiency.

A variable number of insulation layers with distinct materials can be selected in the model. Furthermore, a variable number of heat flow paths can be set, which is for example useful to account for different insulation structures in floor, top and side directions of the packed-bed storage unit, as also done by Prenzel et al. [147].

The thermal insulation model can either incorporate

- stationary or
- dynamic heat transfer.

The stationary heat transfer requires the material's thermal conductivity and thicknesses of each layer, whereas the dynamic heat transfer additionally requires the material's heat capacity and density to account for the thermal energy storage in each control volume of the insulation model. Due to the large temperature variation, the thermal conductivity and heat capacity can be set as temperature dependent functions in the respective media models.

Axial heat conduction is taken into account in the dynamic thermal insulation model besides the lateral heat conduction, as axial heat conduction through the thermal insulation material may lead to thermal destratification of the packed-bed storage and thus reduce the storage capacity.

The coefficient for the convective heat transfer from the outer thermal insulation surface to the surrounding air is set according to the ambient conditions.

#### 4.2.4 Further Air Cycle Component Models

This section includes the models for all ETES air cycle components besides the packed-bed storage, such as the electric heater, fan, HRSG, valves and pipe sections. For the results of this work, these component models are kept as simple as possible, in order to limit the computational time due to the targeted long simulation time. Nevertheless, more detailed component models, especially concerning the dynamic behavior, can be instantiated alternatively by means of *Modelica's* replaceability-feature. These models are introduced in the *Future Energy Solution* project report [179].

## Electric Heater

The heat  $\dot{Q}_{\text{air}}$  transferred from the electric resistor elements to the air inside the heater is determined from a first order system to simplify the dynamics

$$\frac{d\dot{Q}_{\text{air}}}{dt} = \frac{\eta_{\text{el}} \dot{W}_{\text{el}} - \dot{Q}_{\text{air}}}{\tau_{\text{eh}}}. \quad [4.6]$$

The electric efficiency  $\eta_{\text{el}}$  is used to account for the conversion losses in the electric heater, such as transformer losses.

The air inside the electric heater is discretized in flow direction and dynamic mass, momentum and energy balance equations are used for each finite volume. The pressure loss is defined as nominal pressure loss according to Equation 4.5. Heat losses to the environment are taken into account using a thermal insulation model as described in Section 4.2.3.

## Fan with Electric Motor

Constant electric, mechanical and polytropic efficiencies are used to model the fan along with its electric motor. The dynamic behavior is simplified as first order system for the mass flow. The actual mass flow is determined from the mass flow set point and time constant

$$\frac{d\dot{m}}{dt} = \frac{\dot{m}_{\text{set}} - \dot{m}}{\tau_{\text{fan}}}. \quad [4.7]$$

The outlet temperature is calculated by means of the fan polytropic efficiency

$$T_{\text{out}} = T_{\text{in}} \left( \frac{p_{\text{out}}}{p_{\text{in}}} \right)^{\frac{\kappa-1}{\eta_{\text{poly}}\kappa}}. \quad [4.8]$$

The air mass, momentum and energy balances are stationary in the fan model.

The electric work needed for the motor is determined from the electrical and mechanical efficiencies as well as the air enthalpy difference

$$\dot{W}_{el} = \frac{1}{\eta_{el} \eta_{mech}} \dot{m} (h_{out} - h_{in}) . \quad [4.9]$$

### Heat Recovery Steam Generator

The water-steam temperature profile along the air flow path in the HRSG is taken into account in the air cycle model to include its restriction on the transferred heat and the exergy loss associated with the temperature difference at heat transfer. But solving the dynamic water-steam side balance equations is avoided for the ETES system simulation in order to reduce the computational time due to the large number of discharge operation starts and stops. Alternatively, a pinch-point temperature approach is used, as proposed for design calculations by Eriksen [58] and Ganapathy [64]. An advantage of the approach is that little detail on the specific HRSG design has to be known, except for the general layout, and the pinch- and approach-point temperature differences. According to Eriksen [58], the pinch-point temperature difference is typically at 5.5 to 11 °C.

For the results of this work, a once-through or Benson-type HRSG with single pressure level for evaporation and without steam reheating is used. Exemplary air and water-steam temperatures along the air flow path for this type of HRSG are shown schematically in Figure 4.7.

The pinch-point temperature difference  $\Delta T_{pp}$  is between the steam saturation  $T_{sat}$  and evaporator air outlet temperature. The approach-point difference  $\Delta T_{ap}$  is between the steam saturation and the economizer water outlet temperature. These differences limit the heat transfer and therefore also the air and steam outlet temperatures.

The outlet steam mass flow  $\dot{m}_{steam}$  is determined in the model from a simplified energy balance for the superheater and evaporator

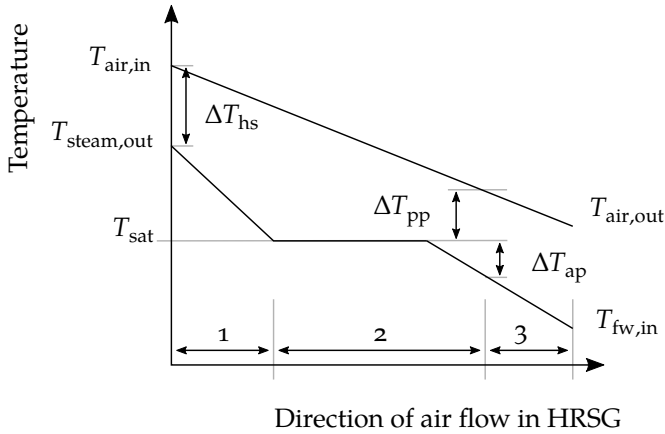


**Figure 4.7 /** Schematic air and water-steam temperatures along the air flow path in single-pressure heat recovery steam generator with superheater (1), evaporator (2) and economizer (3).

$$\dot{m}_{\text{air}} c_{p\text{air}} (T_{\text{air,in}} - T_{\text{sat}} - \Delta T_{\text{pp}}) = \dot{m}_{\text{steam}} (h_{\text{steam,out}} - h(T_{\text{sat}} - \Delta T_{\text{ap}}, p_{\text{out}})). \quad [4.10]$$

The saturation temperature is a function of the steam outlet pressure  $T_{\text{sat}} = f(p_{\text{out}})$ , which is set by the steam turbine or bypass valve. The pressure drop on the water-steam side of the HRSG is neglected.

The steam outlet temperature  $T_{\text{steam,out}}$  is modeled as function of the air inlet temperature

$$T_{\text{steam,out}} = \begin{cases} T_{\text{set}} & \text{for } T_{\text{air,in}} > T_{\text{set}} + \Delta T_{\text{hs,min}} \\ T_{\text{air,in}} - \Delta T_{\text{hs,min}} & \text{for } T_{\text{sat}} < T_{\text{air,in}} < T_{\text{set}} + \Delta T_{\text{hs,min}} \\ T_{\text{sat}} & \text{for } T_{\text{air,in}} < T_{\text{sat}} \end{cases} \quad [4.11]$$

For a regular once-through operation, the steam outlet temperature is kept constant at the set point  $T_{\text{set}}$  by control of the steam mass flow. For lower air

inlet temperatures, a minimum temperature difference at the HRSG hot side  $\Delta T_{hs,min}$  is enforced in the model. The minimum steam outlet temperature is the saturation temperature.

The transferred heat in the superheater, evaporator and economizer and thus the air outlet temperature is calculated from the steam mass flow determined by Equation 4.10, using the stationary water-steam side energy balances.

The air side is discretized in flow direction and dynamic mass, momentum and energy balance equations are used for each finite volume, matching the other component models. The pressure loss is defined by means of the nominal pressure loss according to Equation 4.5.

At low air mass flow rates, a minimum water flow rate in the economizer and evaporator pipes is ensured, which leads to a blow-down flow at start up and cool down of the HRSG. Heat losses to the environment are taken into account using a thermal insulation model, as described in Section 4.2.3.

## Pipes and Valves

The pipe and valve models include a finite volume representation of the enclosed air and sub-models for the pipe wall and thermal insulation, as described for the packed-bed storage in Section 4.2.3. Thus, static or dynamic lateral heat transfer can be taken into account. The pipe length and diameter depend on the specific ETES unit design. Different geometries can be defined for the pipes, such as multiple pipes in parallel or rectangular ducts.

The pressure loss is set by means of a nominal value at nominal density and velocity for each pipe section according to a quadratic relation of pressure loss and velocity, as defined in Equation 4.5. The nominal pressure loss for each pipe section is either a measured value or determined according to the correlation of *Konakov*, given in the *VDI Heat Atlas* [13, section Lab]. An additional pressure drop coefficient may be added to account for bends or other fittings. Values for such pressure drop coefficients are also collected for example in the *VDI Heat Atlas* [13, section Lab].

For each valve a nominal pressure drop and leakage rate or minimum valve

opening must be defined.

## 4.3 Porous-Media CFD Simulation

Three-dimensional flow effects can be significant for large-scale packed-beds as in the case of the TES units in an ETES system. Possible reasons are

- natural convection for horizontal-flow packed-bed designs, especially at hold operation,
- deviations from plug flow due to an abrupt variation of the cross section,
- uneven flow field according to the temperature dependency of the gas density, which may eventually lead to an amplification of temperature field anomalies at discharge, and
- uneven flow according to porosity variations throughout the packed bed.

As the ETES efficiency and usable storage capacity are sensitive to the flow and temperature field in the packed-bed and the technical experience for packed-bed TES is low, especially for large scales and horizontal air flow, a three-dimensional model of the packed bed is used to verify the applicability of the one-dimensional model used in system simulation. Only the packed bed itself is included in the computational domain.

The three-dimensional simulation of the temperature and flow field in the packed-bed is done by means of the finite-volume method in the commercial CFD software *STAR-CCM+*<sup>®</sup> [162]. The whole sequence of simulation setup, run and post processing is automated with macros. The packed-bed geometry can be either defined by means of a surface mesh for irregular storage shapes or as length, height and width for a rectangular storage unit. Furthermore, the packed-bed property correlations and a predefined list of parameters are needed as input.

### 4.3.1 Modeling of Porous Medium

The packed bed is modeled as porous medium with a spatially constant porosity. A vertical porosity variation has not been found to improve the accuracy at validation for the tested horizontal-flow packed beds and is thus not further taken into account. This is different from the findings of Zanganeh et al. [198] for vertical-flow packed beds. A porosity reduction in the vicinity of storage walls is neglected according to

- the irregular particle shapes, which lead to a leveling of the porosity in close vicinity to the wall, as described in Section 2.6.2, and
- the high relation of packed-bed scale to particle size of  $\sqrt{A_{\text{bed,cross}}}/d_p = 250$  to 1500.

The continuity equation for porous media in *STAR-CCM+*<sup>®</sup> is a finite volume formulation of Equation 2.28. The porous-media momentum balance in *STAR-CCM+*<sup>®</sup> is similar to the free-flow momentum balance, but includes an additional body force for the inertial and viscous flow resistance according to Equation 2.30. The permeability and inertial coefficient are taken from the results of particle-resolved CFD simulations, according to Equation 4.20. Furthermore, the gravitational force is taken into account, in order to include the effect of natural convection.

A one-equation energy balance, as shown in Equation 2.36, is used for the three-dimensional CFD model as well, due to the better numerical robustness and faster computation in comparison with a two-equation energy balance. Furthermore, a comparison of both energy balance variants with measurement data has indicated, that the two-equation model is not significantly more accurate for the tested operating conditions and designs characteristic to the deployment in an ETES unit.

No turbulence model is used in the porous medium, as the effect of turbulence on the flow and temperature field is already accounted for in the additional body force and ETC model, as further explained in the *STAR-CCM+ Documentation*[163].

As the ETC model of Equation 2.50 is inherently implemented in the porous-media energy balance of *STAR-CCM+*<sup>®</sup>, the solid thermal conductivity is

modified in order to obtain

- an temperature-variant ETC at stagnant fluid according to Equation 4.23,
- a flow-related ETC in the local flow direction as defined in Equation 2.47 according the derivation of Vortmeyer et al. [182] and
- a flow-related ETC in other directions according to Equation 2.46, using a constant of 5.7 according to the *VDI Heat Atlas* [13, section Mh] for particles of crushed material.

The air density is determined from the ideal gas law. The thermal conductivity, dynamic viscosity and specific heat capacity of air are defined as polynomials in temperature. Their constants are determined from table data interpolation in *Matlab*<sup>®</sup>, using data from the *VDI Heat Atlas* [13, section Dbb]. The specific heat capacity and thermal conductivity of the storage material are modeled as temperature dependent polynomials as well, according to Equations 4.3 and 4.4.

Due to the low fluid velocity and Mach number, the flow is modeled as incompressible. Thus, the *STAR-CCM+*<sup>®</sup> segregated flow solver is used to reduce the computational time. A second-order upwind scheme is set for the discretization of the convection term.

### 4.3.2 Initial and Boundary Conditions

An illustration of the computational domain is shown in Figure 4.8 for a rectangular storage unit. A symmetry plane in vertical and main flow direction is used to reduce the computational time.

Wall boundaries are set on the sides of the packed bed. In contrast to the one-dimensional packed-bed storage model used in the system simulation, only stationary heat transfer is taken into account for the thermal insulation in order to avoid the computational demand associated with three-dimensional discretization of the thermal insulation. The boundary heat flux is determined from the outer heat transfer coefficient  $\alpha_{\text{env}}$ , the packed-bed surface temperature  $T_w$  and the thermal resistance of the insulation layers, which depend on the thermal conductivity  $\lambda$  and thickness  $\Delta y$  of each layer

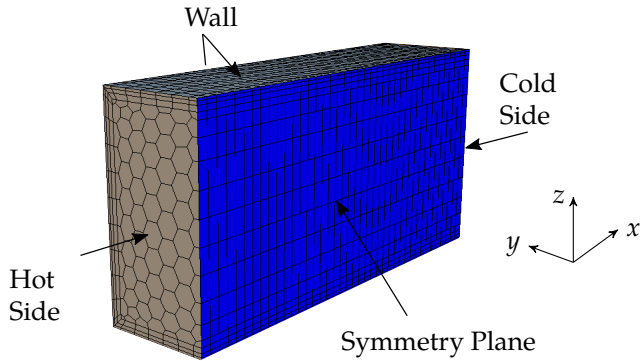


**Figure 4.8 /** Boundary conditions and a very coarse structured mesh for porous-media CFD of rectangular storage geometry.

**Table 4.2 /** Conditions at the hot and cold side boundary for each operation mode in the porous-media CFD simulation.

	Charge	Discharge	Hold
Hot Side	$\dot{m} = \dot{m}_{\text{set}}$ $T = T_{\text{set}}$	$p = p_{\text{env}}$	$p = p(z)$ $T = T_{\text{set}}$
Cold Side	$p = p_{\text{env}}$	$\dot{m} = \dot{m}_{\text{set}}$ $T = T_{\text{set}}$	$p = p(z)$ $T = T_{\text{set}}$

$$\frac{\dot{Q}_w}{A_w} = \frac{1}{\frac{1}{\alpha_{\text{env}}} + \sum \frac{\Delta y}{\lambda}} (T_w - T_{\text{env}}). \quad [4.12]$$

No packed-bed-to-wall thermal contact resistance is taken into account.

The type of boundary condition as well as the respective temperature, pressure and mass flow values at the hot and cold side of the packed bed depend on the storage operation. An overview on the used boundary conditions for each storage operation mode is given in Table 4.2. At any operational mode change, the type of boundary condition is automatically adopted. Thus, any irregular sequence of charge, discharge and hold operation can be simulated.

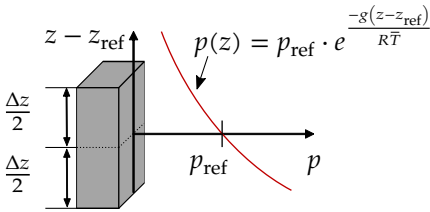


**Figure 4.9 /** Static pressure profile at hot and cold side boundary during hold operation.

The mass flow and temperature values at the hot and cold side boundaries are imported as time table from dynamic system simulation results. Thus, the inlet conditions are in accordance with the dynamic system simulation for charge and discharge. Furthermore, the rate of temperature change at the hot and cold side boundaries at hold operation are in accordance with the overall thermal dynamics of the ETES system, as modeled in system simulation.

Due to the gravitational force, the static pressure is a function of each cells vertical position, which is automatically taken into account in *STAR-CCM+*<sup>®</sup> by means of a constant reference density. But, due to the significant temperature and thus air density variation between the hot and cold side of the packed bed, the pre-defined static pressure profile must be corrected at the hot and cold side boundaries during hold operation. It is alternatively defined with the mean surface temperature at the respective boundary  $\bar{T}$ , as shown in Figure 4.9.

At any change of operational conditions, the flow field is reinitialized with a spatially constant velocity in accordance with the boundary conditions to ensure convergence and to reduce the computational time. Therefore, the temperature field is stored externally and reloaded into the simulation after each re-initialization. The initial static pressure in the packed bed is set in accordance with the defined static pressure function at the hot and cold side boundaries for the initialization of each hold operation.

### 4.3.3 Temporal and Spatial Discretization

A regular mesh is used for rectangular storage units in order to reduce the computational time. In other cases, an unstructured polyhedral mesh is used. The mesh is automatically generated by *STAR-CCM+*<sup>®</sup>. Three prism-layers are used at the packed-bed-to-wall surface, in order to improve the representation

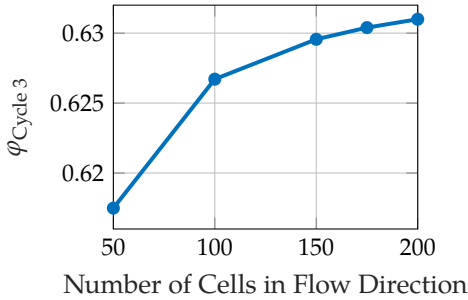


**Figure 4.10 /** Variation of simulated usable capacity ratio for the 3rd cycle of a cyclic full charge and discharge operation with the number of cells in the main air flow direction (horizontal) at a Courant number of  $Co = 0.2$ . The overall number of cells increased from  $0.03 \times 10^6$  to  $1.1 \times 10^6$  and the computational real time from 0.8 to 67 h .

of a thermal gradient in the vicinity of the wall. A very coarse mesh example is shown in Figure 4.8.

An implicit solver is used in order to allow larger time steps. The time step is set according to a modified Courant number, which is defined with the approximated thermocline velocity as

$$Co = \frac{\Delta t}{\Delta x} \frac{v_{x,f} \rho_f c_{pf}}{(1 - \varepsilon) \rho_p c_{pp}} . \quad [4.13]$$

A Courant number of 0.2 has been found to give sufficiently good results at acceptable computational time. The resulting time step is at 60 to 180 s, depending on the storage unit dimensions and operating conditions.

Results of a mesh independence study are shown in Figure 4.10 for a rectangular storage unit with a length of 10 m at cyclic operation. 100 to 150 finite volumes are used in main flow direction ( $x$ ) of the storage in Chapters 5 and 6 accordingly as trade-off between computational time and precision. The discretization leads to cell sizes at 0.01 to 0.1 m for the tested packed-bed designs. Notably, fewer cells in flow direction are needed compared to the one-dimensional packed-bed model. The discretization in both lateral directions ( $y, z$ ) is less influential and the cell dimensions are thus doubled in these directions.

A sufficient convergence of the temperature and flow field is assumed for each inner iteration, if the normalized root mean squared value of all cells energy

and mass balance residuals falls below a threshold of  $1 \times 10^{-5}$ .

### 4.3.4 Post Processing

Mass-flow averaged reports for the packed-bed in- and outlet temperatures as well as absolute pressures are exported as time tables. The pressure drop is determined from the absolute pressure difference. The temperature field is averaged on a number of planes, which are perpendicular to the main flow direction and have equidistant spacing, in order to compare one- and three-dimensional temperature fields. The mean temperature for each plane is exported as time table as well. Furthermore, the energy stored in the packed bed at each time step is determined according to Equation 4.1.

## 4.4 Particle-Resolved CFD Simulation

Particle-resolved CFD simulation is used in this work to determine the packed-bed properties, as necessary to describe the packed bed with a macroscopic porous-media model. The properties are determined for each distinct packed-bed individually, in order to obtain a higher precision compared to general correlations. The DEM is used to generate the packed-bed surface.

The commercial software *STAR-CCM+*<sup>®</sup>[162] is applied for the overall DEM-CFD workflow. An overview on the used method for the numerical determination of the packed-bed properties is shown in Figure 4.11. The parameters to the DEM are the particle's shape, size distribution and mechanical properties. The generated packed-bed surface can be used in subsequent CFD simulations to determine correlations for the

1. packed-bed body force  $f_{\text{bed}}$  in the direction of air flow,
2. particle-to-fluid heat transfer coefficient  $\alpha_{\text{p-f}}$ ,
3. its correction for intra-particle solid thermal resistance  $\alpha_{\text{eff}}/\alpha_{\text{p-f}}$  and the
4. ETC at stagnant fluid  $\lambda_{\text{eff},0}$ .

Separate models are used for the determination of the packed-bed property

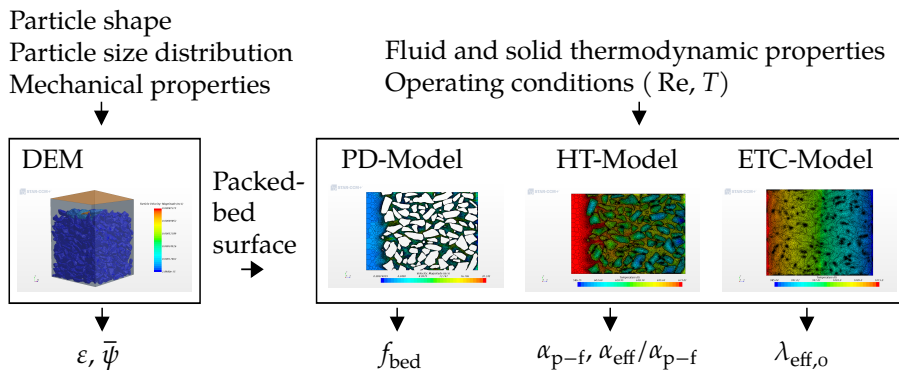


**Figure 4.11** / Overview on DEM-CFD workflow.

correlations to allow maximum flexibility in terms of computational volume, discretization, boundary conditions and initialization. These models are referred to as Pressure Drop (PD)-, Heat Transfer (HT)- and ETC-model in the following.

Similar DEM-CFD workflows have been applied in the field of chemical engineering in order to calculate the pressure drop in reactors containing catalyst particles [15, 56, 91, 173]. Some authors also investigated the particle-to-fluid heat transfer [92, 129] or the ETC of packed beds [177]. Other research areas employing particle-resolved simulations are high-temperature gas-cooled nuclear reactors [193] or in-situ thermal processing of oil sands [82]. The DEM has been further used by Coetzee [37] and Coetzee et al. [38] to investigate the stability of self-supporting tunnels in rock beds.

The packed-bed porosity can not be determined uniquely for a certain DEM parameter set. Reason is the unknown packed-bed densification, as described in Section 2.6.2, which results from mechanical or thermal processing of the packed bed. When using the DEM, the particle injection velocity can be used to generate a loose or dense packed bed, as it sets the amount of available energy for packed-bed densification via rearrangement of particles. Figure 4.12 shows the effect of the particle injection velocity on the porosity. In this work, the final packed-bed properties are determined by interpolation of the packed-bed properties for a loose and dense packed bed according to the measured packed-bed porosity.

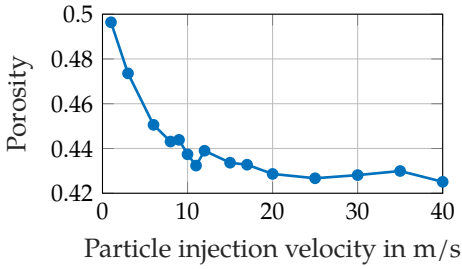


**Figure 4.12** / Characteristic trend for packed-bed porosity variation with respect to particle injection velocity in the DEM.

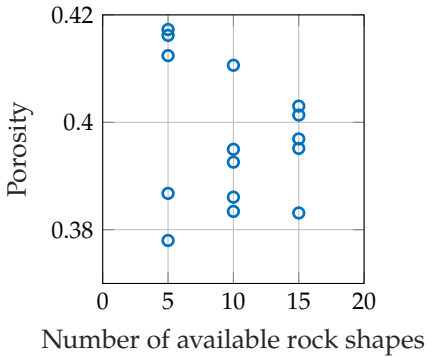


**Figure 4.13** / Packed-bed porosity at a different number of available rock shapes out of 20 and five simulation run repetitions.

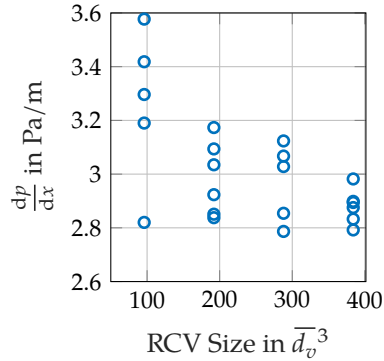


**Figure 4.14** / Pressure gradient at different RCV sizes and five simulation run repetitions.

In reality, each particle shape is different for crushed natural rock, but only a limited number of distinct representative rock shapes can be used in the DEM simulation in order to reduce the complexity. 20 distinct crushed rock shapes determined from laser scanning were provided by Siemens Gamesa Renewable Energy for this work. A similar approach has been used by Latham et al. [106]. Figure 4.13 shows the influence of the number of available rock shapes on the porosity. For each simulation run, a set of shapes was randomly selected out of the 20 available rock shapes, with different limitations on the number of available rock shapes. An asymptotic trend is visible. Accordingly, all 20 available shapes need to be used in order to reduce the dispersion.

The whole DEM-CFD workflow is automated with macros, as also described by Eppinger et al. [55], and similar to the porous-media CFD simulation. All

packed-bed properties can be determined by provision of the particle shapes in the form of a surface mesh, the particle size distribution and a predefined list of parameter values.

## Representative Computational Volume

Due to computational constraints, especially in real time and main memory, the CFD simulations can only be done in small computational volumes compared to the packed-bed storage size. Nevertheless, packed beds are irregular structures, their local properties vary in space. Furthermore, the fluid flow paths in packed beds can be much longer than the direct flow path, as also expressed by the packed-bed tortuosity. Therefore, the computational volume has to be large enough to

- level out random packed-bed structure variations and
- give the option of bypassing areas with high flow resistance.

It is then called RCV. Figure 4.14 shows simulation results for the local pressure gradient at a single operating point, determined with different RCV sizes. A reduction of dispersion between several simulations runs and a reduction of the mean value can be detected with growing RCV size, according to the two reasons listed above.

The DEM-CFD workflow is computationally expensive according to the required RCV size and mesh resolution, further reviewed in Section 4.4.4. Nodes of the high performance cluster at the Hamburg University of Technology are used for the calculation, each having 24 cores. The resulting computational requirements are given in Table 4.3.

### 4.4.1 Generation of Packed Bed Surface

The simulation domain for the DEM is a container of rigid walls as shown in Figure 4.15. The container volume must be larger than the RCV to suppress the influence of the container walls on the porosity inside the RCV. At least one mean volume-equivalent particle diameter is used, according to Section 2.6.2,

**Table 4.3** / Computational requirements of DEM-CFD workflow.

	DEM	PD-Model	HT-Model	ETC-Model
RCV size	-	$384 \bar{d}_v^3$	$216 \bar{d}_v^3$	$288 \bar{d}_v^3$
Cell Count	-	$60 \times 10^6$	$40 \times 10^6$	$30 \times 10^6$
Main memory	40 GB	180 GB	200 GB	190 GB
Real Time	10 h	10 h	20 h	15 h

which is also in good accordance with porosity variations determined from own DEM simulations.

During the simulation time, particles are injected into the domain from a set of injection points close to the top and move downwards due to the gravitational force. At each time step only half of the injection points are available. Their selection is random, such as the particle initial orientation, which leads to a different packed bed after each simulation run, even at equal DEM parameter sets. The particle shape and size is automatically selected for each injected particle to obtain the targeted mass fraction for each shape and size class. The injection flow rate has to be chosen small enough to prevent particle overlap at the injection points, as overlapping particles are deleted after injection and the target size distribution would not be obtained in the end.

Besides spheres, irregular geometries can be used as particle shape by means of the multi-sphere method. With this method, the original particle surface is approximated with eventually overlapping spheres of different size, as shown in Figure 4.16, to reduce the complexity of the DEM method. 100 spheres have been found to give a good representation for this work. An investigation on the validity of the multi-sphere method has been done by Kruggel-Emden et al. [102].

The particle size distribution is specified as cumulative distribution function of the volume-equivalent particle diameter  $d_v$ , as defined in Equation 2.23. The size distribution is defined with respect to the particle count. A mass specific distribution can be derived using the mean particle size for each size class. The size definition used for the results of this work is shown in Figure 4.17. A measured size distribution on the other hand has been used at validation. The porosity of packed beds is sensitive to the size distribution width [107].

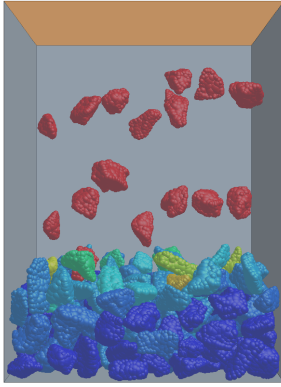


**Figure 4.15** / Velocity of particles at packing process with downwards gravity. The velocity ranges from 10 m/s (red) to 0 m/s (blue).

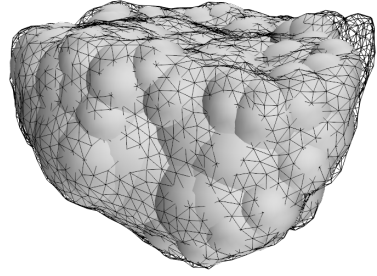


**Figure 4.16** / Multi-sphere approximated particle shape.

The porosity reduction with the size distribution width for the distribution of Figure 4.17 is shown in Figure 4.18. Accordingly, a precise measurement of the size distribution is necessary.

In each time step the equation of motion for each particle is solved by the DEM algorithm, considering linear and rotational degrees of freedom

$$\begin{aligned}
 m \frac{d\mathbf{v}_p}{dt} &= \mathbf{F}_g + \mathbf{F}_{\text{contact}} \\
 J \frac{d\boldsymbol{\omega}_p}{dt} &= r_{\text{contact}} \times \mathbf{F}_{\text{contact}} \cdot
 \end{aligned}
 \tag{4.14}$$

The gravitational force  $\mathbf{F}_g$  acts on the particle's center of gravity. A linear spring model is used for the contact force  $\mathbf{F}_{\text{contact}}$ . The force thus results from any overlap with other particles or walls and has a normal and tangential component. Parameters of the model are the spring stiffness and damping coefficient which can be determined from the material's coefficient of restitution, as described in the *STAR-CCM+ Documentation* [163], and a static friction coefficient. No fluid friction and particle rolling friction is taken into account. The mechanical storage material's properties are shown in Table 4.4. They are

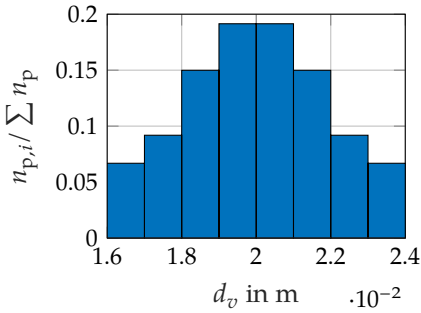


**Figure 4.17** / Particle size distribution with a mean volume-equivalent diameter of  $\bar{d}_v = 0.02$  m and a standard deviation of  $\sigma = 0.002$  m .

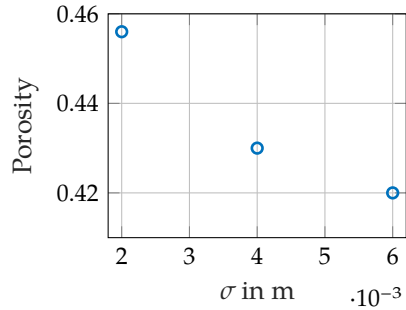


**Figure 4.18** / Variation of the porosity with the standard deviation  $\sigma$  at a mean volume-equivalent diameter of  $\bar{d}_v = 0.02$  m.

**Table 4.4** / Mechanical storage material's properties used in the DEM contact model, according to Coetzee et al. [38].

Stiffness	Static Friction Factor	Coefficient of Restitution
0.62 MN/m	0.9	0.23

taken from a DEM study by Coetzee et al. [38].

The time step of the simulation is automatically adopted by the DEM solver to dissolve collisions and ensure convergence. The simulation continues until the packed bed has settled and the velocity of each particle falls below a limit of  $|\mathbf{v}_p| < 0.001$  m/s. Finally, the sphere-approximated particles are replaced by their original shape at the exact same location and orientation. The packed-bed surface mesh is then exported for further use in subsequent CFD simulations.

## 4.4.2 Modeling of Fluid Flow and Heat Transfer

The finite volume method is used to solve the continuity equation as well as the momentum and energy balance in the computational domain. The energy balance is not needed in the PD-model, whereas the momentum balance is not needed in the ETC-model.

The effect of the intra-particle thermal resistance on the particle-to-fluid heat transfer must be taken into account, as the Biot number according to Equation 2.42 is generally larger than 0.1 for characteristic ETES operating conditions and the tested particle sizes, especially due to the low thermal conductivity of natural rock.

In order to limit the computational time, all simulations are stationary. To allow a stationary simulation of the particle-to-fluid heat transfer an evenly distributed volumetric energy source or sink is introduced inside the particles. It corresponds to the assumption of a uniform heating or cooling of all particles in the computational domain. The source term is determined from a simplified packed-bed energy balance as

$$\frac{\dot{Q}}{V_p} = \frac{v_{x,f} \rho_f c_{pf}}{1 - \varepsilon} \frac{dT}{dx}. \quad [4.15]$$

Comparison of the stationary results with a dynamic calculation of the heat transfer showed no deviation of the results, thus verifying the approach. Further verification studies showed, that a variation of the temperature gradient or a sign change, which corresponds to charge or discharge operation, has a negligible effect on the resulting heat transfer coefficient.

The flow is modeled as incompressible, as the Mach number is low. Therefore, the *STAR-CCM+*<sup>®</sup> segregated flow solver is used to reduce the computational time. The convection term is discretized with a second order upwind scheme.

The air density depends on the temperature and is determined from the ideal gas law. The specific heat capacity and thermal conductivity of air are assumed as constant for each operating point and determined from table interpolation at the respective mean temperature inside the computational volume, using data from the *VDI Heat Atlas* [13]. As the pressure in the packed-bed storage unit of ETES systems is close to ambient pressure, no pressure dependency of the air thermal conductivity is taken into account. The specific heat capacity and thermal conductivity of the particles are set as constant values for each operating point as well, according to the respective mean temperature and Equations 4.3 and 4.4.

Following Dixon et al. [48], transition from laminar to turbulent flow occurs at a Reynolds number of  $100 < Re < 200$ , using the definition in Equation 2.29. Turbulence is modeled using the Reynolds Average Navier Stokes method. In the turbulent regime, the realizable  $k,\varepsilon$ -turbulence-model, as implemented in *STAR-CCM+*<sup>®</sup>, is selected, as it has been found to give acceptable results compared to direct numerical simulation in packed beds of monodisperse spheres using the method outlined by Jin et al. [93]. The  $k,\varepsilon$ -turbulence-model has also been employed by Bai et al. [15] and Eppinger et al. [56] for particle-resolved CFD simulation.

Variation of the surface sand-grain roughness in the turbulence model does not effect the pressure drop in the simulation. Thus, the particle surface is modeled as hydraulically smooth in the turbulent regime, meaning the roughness height is smaller than the viscous boundary layer thickness. The negligible effect of the surface roughness in the turbulent regime is reasonable, as the pressure drop in porous media is mainly caused by inertial forces for high Reynolds numbers [39], according to the packed bed tortuosity and less dependent on the surface friction, which is more relevant at low air velocities and thus laminar flow.

Radiation must be taken into account in the ETC-model, due to the high ETES storage temperature. According to Zanganeh et al. [198] radiation becomes more important than heat conduction in packed beds at temperatures above 150 °C. The radiation is modeled as gray-body thermal surface-to-surface radiation. The transferred heat from any surface to another can be determined from the view factor and the particle emissivity. The pore space is assumed transparent. The view factor is automatically determined by *STAR-CCM+*<sup>®</sup> for each surface. In order to reduce the computational time, the used mesh is coarser than the original surface mesh by a factor of 10, which has been identified as reasonable trade-off between accuracy and computational time.

### 4.4.3 Boundary Conditions

An rectangular computational domain is used for each of the CFD simulations, as shown in Figure 4.19. A velocity inlet is used as upstream and a pressure outlet as downstream boundary condition in the PD- and HT-model. The inlet velocity is determined from the Reynolds number set-point for the respective

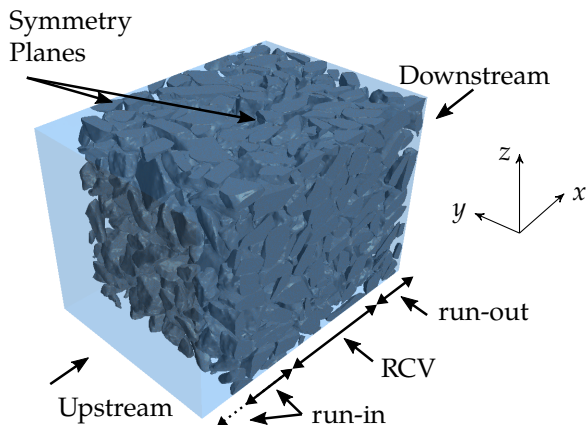


**Figure 4.19** / Overview on boundary conditions used for particle-resolved CFD simulation.

simulation run. In the ETC-model, a constant temperature is used as upstream and downstream boundary condition, which is determined from the mean temperature set-point and an arbitrary temperature gradient, which does not affect the ETC. Symmetric boundary conditions are used at the four sides of all models in order to determine the properties inside the packed bed, thus preventing any wall influence.

The RCV is extended with a run-in and run-out section to suppress the influence of the used up- and downstream boundary conditions on the results. Verification showed that a length of two volume-equivalent particle diameters is sufficient for the run-in and run-out sections in all three models. Thus, it is longer than the wall-effect influence on the porosity, which results from the DEM.

An additional fluid volume is added by mesh extension at the upstream side for the PD- and HT-model in order to allow the air to adopt to the available flow paths in the downstream packed bed. No extension is used at the outlet, as turbulence would lead to convergence problems otherwise and the effect on the flow field in the RCV is sufficiently prevented by the run-out section filled with particles.

The operating range is set by means of the Reynolds number and temperature.

Ten different Reynolds numbers in the range of  $1 < \text{Re} < 2500$  are simulated with the PD-model, which covers the superficial air velocities observed for different ETES packed-bed storage designs in system simulation, ranging from 0.01 to 2 m/s. Reynolds numbers below ten are omitted in the HT-model, as the temperature difference between the particles and fluid becomes negligible and thus also the relevance of the particle-to-fluid heat transfer coefficient. Eight mean temperatures are simulated with the ETC-model in the range of  $300 \text{ K} < T < 1000 \text{ K}$ , according to the ETES operating conditions.

The flow direction in the PD and HT-model and the direction of the temperature gradient in the ETC-model can be chosen perpendicular or parallel to the packing direction used in the DEM. This feature is used to calculate different packed-bed properties at horizontal and vertical flow direction in packed beds of irregularly shaped particles, according the vertical direction of a gravity-based packing process.

#### 4.4.4 Spatial Discretization

For the discretization of the computational domain an unstructured, body-fitted mesh with polyhedral cells is generated, using the automatic mesh generation tool provided by *STAR-CCM+*<sup>®</sup>. In the PD-model only the fluid volume needs to be meshed, whereas for the conjugate heat transfer in the HT- and ETC-Model the particles have to be meshed as well. A conformal mesh is generated at the interface to improve the accuracy and stability of the calculation.

Prism-layers are used on the particle surface when fluid flow is present, i.e. in the PD- and HT-Model. The boundary layer is resolved using the low  $y^+$ -approach [163]. The  $y^+$ -values are kept as low as possible with the available main memory resources to place the wall-nearest cell in the laminar sub layer. Typically, 75 % of the particle surface area has a  $y^+$ -value of the wall-nearest fluid cell below one and 95 % below two at a Reynolds number of  $\text{Re} = 1000$ .

The particle contact points need a geometry adaption before meshing, as single points of contact would lead to highly skewed cells. A comprehensive overview on this topic is given by Dixon et al. [49]. In this work, the particles are locally flattened, enforcing a minimum distance between all particles and walls, as

**Table 4.5** / Mesh Parameters as used in particle-resolved CFD simulations.

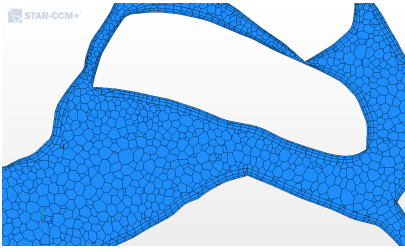
	PD-model	HT-model	ETC-model
Meshed Region	Fluid	Fluid and Particles	Fluid and Particles
Number of Prism Layers	3	3	-
Prism Layer Thickness in % of $\bar{d}_v$	2	2	-
Surface Cell Size in % of $\bar{d}_v$	1 – 2	1 – 3	10 – 4
Volume Growth Rate	1.3	1.3	1.3

described in detail by Eppinger et al. [56]. The method has the least effect on the porosity and can be automatically done in *STAR-CCM+*<sup>®</sup>. Nevertheless, cells of poor quality are still present in the mesh, but their influence on the convergence is automatically suppressed by the *STAR-CCM+*<sup>®</sup> solver.

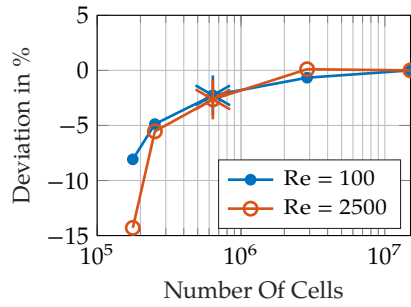
Exemplary sections of the PD, HT- and ETC-model mesh are shown in Figure 4.20 along with results of their mesh independence studies. The selected cell size is indicated. A smaller computational volume is used in the mesh independence study to allow a fine mesh resolution with the available main memory resource. In each mesh refinement step, the base size is cut in half and a prism layer is added, while keeping the prism layer thickness constant. Refining the base size was generally found to reduce the result deviation more than adding additional prism layers. Table 4.5 summarizes the used mesh parameters for all three models.

#### 4.4.5 Post Processing

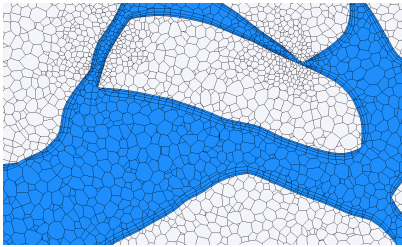
The porosity and particle surface in the RCV are determined by summation of the cell surfaces and volumes of the generated particle surface mesh. The packed-bed correlations are derived from the CFD simulation results for the stationary flow and temperature field at each operation point. A sufficient convergence of the stationary temperature and flow field is assumed, if the relative change of the targeted value, such as the pressure gradient, heat transfer coefficient or effective thermal conductivity, remains below a limit of 0.1 % for 30 consecutive solver iterations.



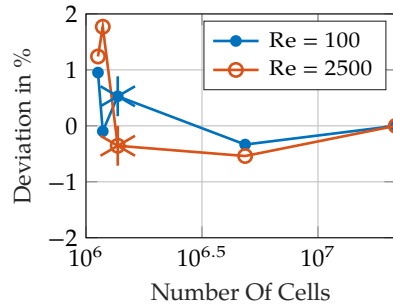
a / PD-model.



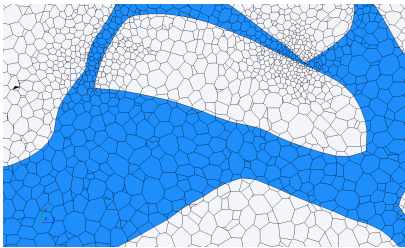
b / PD-model.



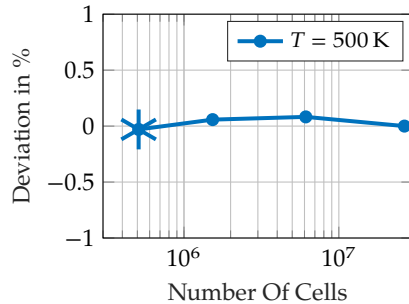
c / HT-model.



d / HT-model.



e / ETC-model.



f / ETC-model.

**Figure 4.20** / Exemplary cut plane sections of mesh used for the PD, HT- and ETC-model and respective mesh independence study results for a small computational domain of  $2.5 \bar{d}_v^3$ . The star denotes the selected mesh. The relative deviation is defined with respect to the target value as determined with the finest mesh .

The packed-bed body force in the RCV is calculated from the mass-flow averaged pressure at the RCV in- and outlet surfaces and the RCV length in flow direction  $\Delta x$

$$f_{\text{bed}} = \frac{\bar{p}_{\text{in}} - \bar{p}_{\text{out}}}{\Delta x}. \quad [4.16]$$

The particle-to-fluid heat transfer coefficient is determined from the heat flux through the particle surface and the difference of the mean particle surface and fluid temperatures  $\bar{T}_{p,\text{surf}}$ ,  $\bar{T}_f$  in the RCV according to Equation 2.37. The correction of the particle-to-fluid heat transfer coefficient for the intra-particle thermal resistance is calculated by means of the relation of temperature differences used in the heat transfer coefficient definitions

$$\frac{\alpha_{\text{eff}}}{\alpha_{p-f}} = \frac{\bar{T}_{p,\text{surf}} - \bar{T}_f}{\bar{T}_p - \bar{T}_f}. \quad [4.17]$$

The heat flux through the outlet surface of the RCV  $\dot{Q}_{\text{out}}$  and the difference of the mean temperature at the RCV in- and outlet surfaces is used to calculate the ETC at stagnant fluid

$$\lambda_{\text{eff},o} = \frac{\dot{Q}_{\text{out}} \Delta x}{A_{\text{out}} (\bar{T}_{\text{in}} - \bar{T}_{\text{out}})}. \quad [4.18]$$

The simulation results for the packed-bed body force, particle-to-fluid heat transfer coefficient, its correction for intra-particle thermal resistance and the ETC at stagnant fluid for each operating condition and packed bed are exported as table data.

### Derivation of Packed-Bed Correlations from Simulated Data

In the last step, the exported simulation data is used in *Matlab*<sup>®</sup> [119] to determine packed-bed specific property correlations by means of curve fitting with

the optimization toolbox.

In a first step, the form of the correlation has to be selected. Various different types of correlations for the packed-bed properties are used in literature, as already reviewed in Section 2.6.2. In order to ease the verification of the derived correlation, a prominent empirical correlation form is chosen as baseline instead of polynomials. The constants in this correlation are then adopted in order to represent the CFD simulation results. All correlations are defined in a non-dimensional way.

The correlation for the packed-bed body force is set to

$$Eu = \frac{B_1}{Re} + B_2. \quad [4.19]$$

It can be converted into the Darcy-Forchheimer form, as shown in Equation 2.30, by means of a permeability  $K$  and inertial coefficient  $c_F$  defined as

$$K = \frac{2\epsilon d_h^2}{B_1} \quad \text{and} \quad c_F = \frac{B_2}{\sqrt{2B_1}\epsilon^3}. \quad [4.20]$$

For the particle-to-fluid heat transfer coefficient, a dimensionless correlation in accordance with the empirical correlation of Wakao et al. [184] is used

$$Nu_{p-f} = B_1 + B_2 Re^{B_3} Pr^{\frac{1}{3}}. \quad [4.21]$$

The effect of the solid thermal resistance on the effective particle-to-fluid heat transfer coefficient  $\alpha_{\text{eff}}/\alpha_{p-f}$  is modeled as function of the Biot number according to the correlation of Stuke [172]

$$\frac{\alpha_{\text{eff}}}{\alpha_{p-f}} = \left(1 + \frac{1}{B_1} Bi\right)^{-1}. \quad [4.22]$$

And finally a superposition of the model derived by Krischer [100] for the conduction related part and a radiation part in accordance with the general term of van Antwerpen et al. [181], as described in Section 2.6.2, is used as correlation for the ETC at stagnant fluid. The radiation exchange factor notably contains a temperature dependency.

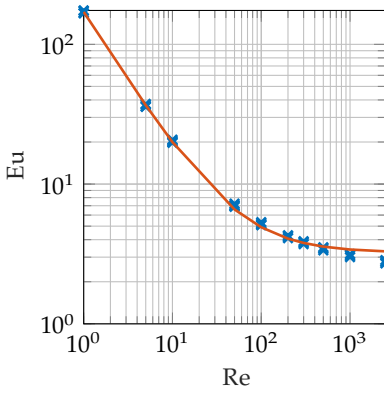
$$k_{\text{eff},o} = \left( \frac{B_1}{k_{\text{eff,cond,I}}} + \frac{1 - B_1}{k_{\text{eff,cond,II}}} \right)^{-1} + \left( B_2 + \frac{B_3}{T} \right) k_{\text{eff,rad}}. \quad [4.23]$$

The constants for each of the correlations and packed beds are exported and can then be used in the one- and three-dimensional packed-bed storage model to define the macroscopic packed-bed properties.

### Averaging of Simulation Run Repetitions

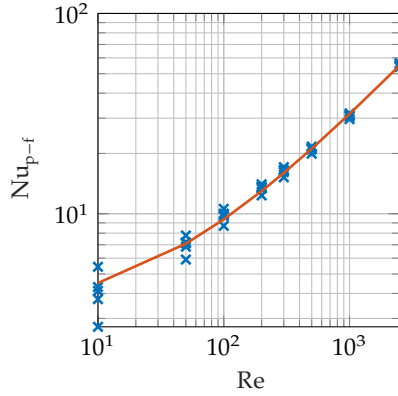
As the RCV size for one simulation run is limited by constraints on the main memory demand, each set of parameters is simulated repeatedly, in order to further level out the influence of the random packed-bed structure on the properties by averaging. Figure 4.21 shows the dispersion of simulation results for each correlation of one exemplary parameter set and an RCV size, as shown in Table 4.3.

The largest deviation among the simulation results, which were all generated with the same DEM parameter set, can be seen for the Nusselt number at low Reynolds numbers, which is due to small particle-to-fluid temperature differences and thus strong impact of pore geometry. The mean Nusselt number at  $Re = 10$  is 4.1. The standard deviation of the Nusselt number at  $Re = 10$  is 0.98, which is the highest value in the whole range of Reynolds numbers. As the Biot number depends on the particle-to-fluid heat transfer coefficient, the results for the intra-particle thermal resistance correction scatter accordingly.



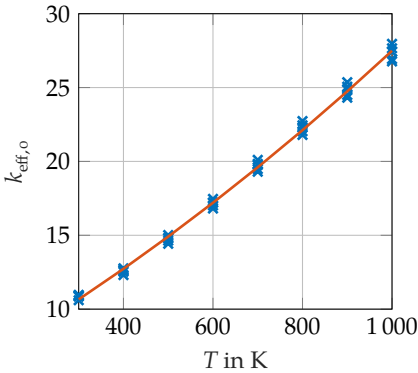
× Results — Correlation

**a** / Pressure Gradient.



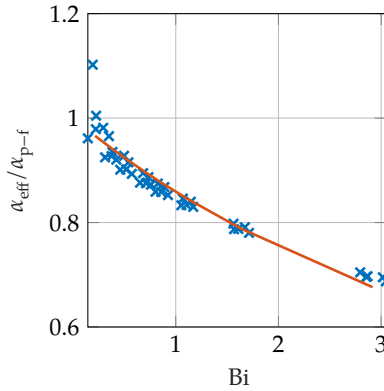
× Results — Correlation

**b** / Particle-to-fluid heat transfer coefficient.



× Results — Correlation

**c** / Effective thermal conductivity at stagnant fluid.



× Results — Correlation

**d** / Correction for intra-particle thermal resistance.

**Figure 4.21** / Dispersion of results for repeated particle-resolved CFD simulations of one exemplary parameter set. Five simulation runs have been done for each operating point.



# Chapter 5

## Model Validation

This chapter provides validation results for the models presented in the previous chapter. At first, exemplary packed-bed property correlations determined from the DEM-CFD workflow are compared to empirical correlations from literature. Then, simulation results for the pressure drop and temperature field inside two horizontal-flow packed-bed storage units are compared to experimental results provided by Siemens Gamesa Renewable Energy. Finally, simulation results for the HRSG and fan of the ETES demonstration plant are compared to manufacturer's specifications.

### Measure for Comparison

In order to compare two curves, the Mean Absolute Error (MAE) of a set of evaluation points  $x_i$  is used as deviation measure

$$\text{MAE} = \frac{1}{n} \sum_{i=1}^n |x_i - x_{\text{ref},i}|. \quad [5.1]$$

## 5.1 Particle-Resolved CFD Simulation

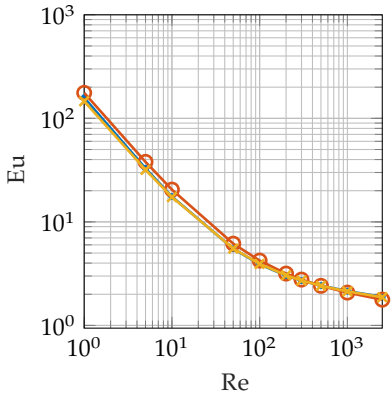
The comparison of simulation results from the DEM-CFD workflow with empirical correlations from literature is shown in this work for two different packed beds, which are composed of either monodisperse spheres or polydisperse rocks. Spheres are chosen as second particle shape for comparison besides the rocks in order to reduce the number of influential quantities and as many correlations are available for such packed beds. A size of 0.03 m is set for all spheres and a particle size distribution as shown in Figure 4.17 for the polydisperse rocks. All 20 available rock shapes, which are determined by laser scan, are used.

A constant thermal conductivity of  $2 \text{ W}/(\text{m K})$ , a density of  $2500 \text{ kg}/\text{m}^3$  and an emissivity of 0.85 are used as material properties for all particles at validation of the particle-resolved CFD simulation. The temperature dependent air properties are interpolated from *VDI Heat Atlas* [13] data. The resulting ratio of the particle and fluid thermal conductivities  $\lambda_p/\lambda_f$ , which defines a further boundary on the applicability of ETC models, is thus at 29 to 75 in the considered temperature range of 300 to 1000 K. The DEM parameters determined by Coetzee et al. [38] are used for the spheres and rocks, as shown in Table 4.4.

Figures 5.1 and 5.2 show the comparison of simulation results and empirical correlations from literature for monodisperse spheres and polydisperse rocks respectively. The correlations derived from the DEM-CFD simulation workflow are shown in blue color. The curve fitting results of the simulated packed-bed properties according to Equations 4.19 and 4.21 to 4.23 are shown in each plot legend. Additionally, the mean absolute error for each empirical correlation is shown in the legend of each plot.

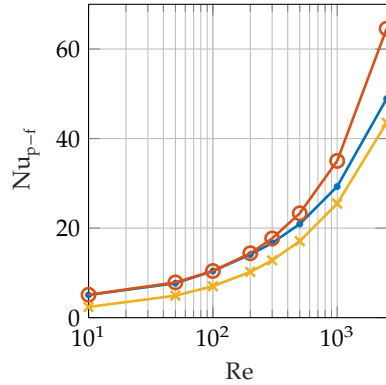
The porosity calculated with the DEM for the monodisperse spheres is  $\varepsilon = 0.385$  and the particle surface area per unit volume  $a_{\text{bed}} = 120 \text{ m}^2/\text{m}^3$ . The exact value for the particle surface area per unit volume according to Equation 2.25 is  $a_{\text{bed}} = 123 \text{ m}^2/\text{m}^3$ . The simulated porosity for the polydisperse rocks is  $\varepsilon = 0.41$  and the particle surface area per unit volume  $a_{\text{bed}} = 217 \text{ m}^2/\text{m}^3$ .

According to Allen et al. [6], packed beds with perpendicular packing and flow direction, which he refers to as cross-current, and packed beds with axial



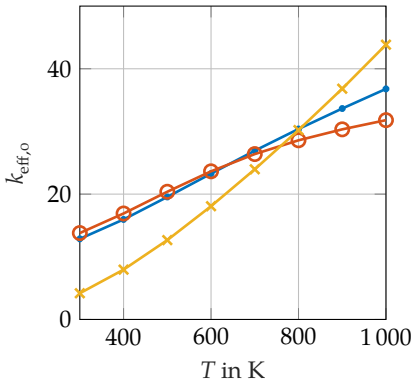
- $Eu = \frac{156}{Re} + 2.09$
- Allen et al. [6] (MAE = 2.8)
- ×— Brauer [27] (MAE = 1.3)

a / Pressure Gradient.



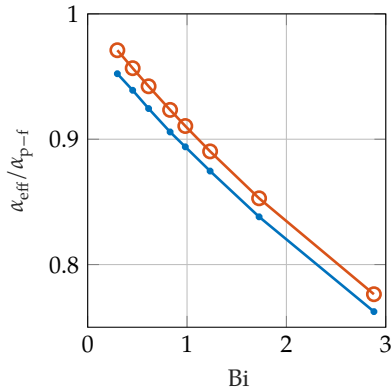
- $Nu_{p-f} = 3.45 + 0.506 Re^{0.589} Pr^{\frac{1}{3}}$
- Gnielinski [69] (MAE = 3.2)
- ×— Wakao et al. [184] (MAE = 3.7)

b / Particle-to-fluid heat transfer coefficient.



- $k_{eff,o} = \left(\frac{0.752}{k_I} + \frac{1-0.752}{k_{II}}\right)^{-1} + \left(-0.0924 + \frac{424}{T}\right)k_{rad}$
- Zehner et al. [200] (MAE = 1.7)
- ×— Yagi et al. [195] (MAE = 5.26)

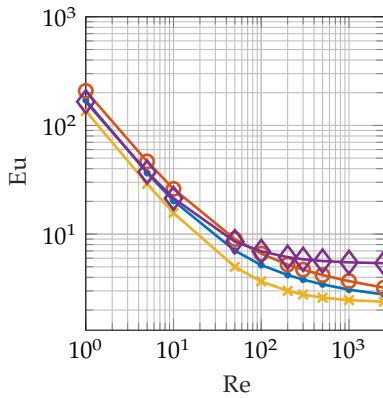
c / Effective thermal conductivity at stagnant fluid.



- $\frac{\alpha_{eff}}{\alpha} = \left(1 + \frac{1}{8.68} Bi\right)^{-1}$
- Stuke [172] (MAE = 0.017)

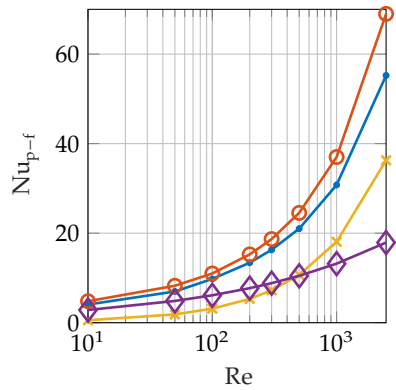
d / Correction for intra-particle thermal resistance.

**Figure 5.1/** Simulation results and correlation from DEM-CFD workflow in comparison with empirical correlations from the literature for packed beds of monodisperse spheres with a diameter of 0.03 m. Five simulation runs have been done for each operating point .



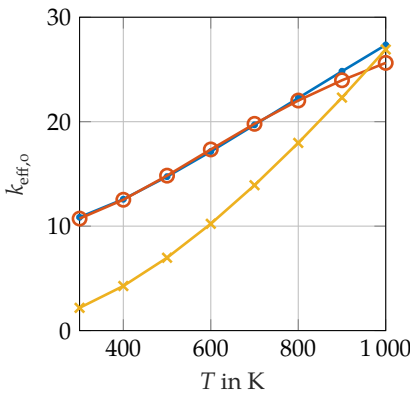
- $Eu = \frac{167}{Re} + 3.23$
- Allen et al. [6] (MAE = 6)
- \*— Ergun [57] (MAE = 5.5)
- ◇— Macdonald et al. [115] (MAE = 2.2)

a / Pressure Gradient.



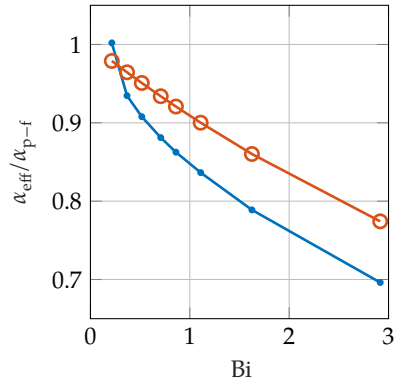
- $Nu_{p-f} = 3.14 + 0.338 Re^{0.658} Pr^{\frac{1}{3}}$
- Gnielinski [69] (MAE = 3.9)
- \*— Coutier et al. [40] (MAE = 9.3)
- ◇— Pfeffer [145] (MAE = 11)

b / Particle-to-fluid heat transfer coefficient.



- $k_{eff,o} = \left( \frac{0.402}{k_I} + \frac{1-0.402}{k_{II}} \right)^{-1} + \left( 0.0057 + \frac{403}{T} \right) k_{rad}$
- Zehner et al. [200] (MAE = 0.42)
- \*— Yagi et al. [195] (MAE = 5.59)

c / Effective thermal conductivity at stagnant fluid.



- $\frac{\alpha_{eff}}{\alpha} = \left( 1 + \frac{1}{6.09} Bi \right)^{-1}$
- Stuke [172] (MAE = 0.053)

d / Correction for intra-particle thermal resistance.

**Figure 5.2** / Simulation results and correlation from DEM-CFD workflow in comparison with empirical correlations from the literature for packed beds of crushed rocks with a size distribution as shown in Figure 4.17. 20 distinct laser-scanned particle shapes were used. Five simulation runs have been done for each operating point .

packing and flow direction, referred to as co-current, have to be distinguished due to the alignment of non-spherical particles at the packing process. As only the co-current correlation is explicitly defined in his paper, axial packing and flow direction is used at validation of the particle-resolved CFD simulation accordingly. For the monodisperse spheres, the empirical correlation of Allen et al. [6] for smooth spheres, which is equation number 38 in his paper, is used for the comparison.

In the correlation of Stuke [172], which is also shown in Equation 2.43, a constant of  $B = 10$  is used for both packed beds, even though this constant has been explicitly derived for monodisperse spheres. Reason is that to the author's knowledge, no constant for crushed rock shapes has been proposed in the literature yet. Following the results of Figure 5.2, a constant of 6 is proposed hereby.

The CFD simulation results for the effect of intra-particle thermal resistance on the particle-to-fluid heat transfer for the monodisperse spheres is smaller than the value according to Stuke [172]. A possible reason is the analytic derivation of Stuke's correlation for a single particle. Thus, the effect of uneven flow through the packed-bed pores is not taken into account.

The correlation of Zehner et al. [200] for the effective thermal conductivity at stagnant fluid shows a better accordance with the DEM-CFD simulation results than the correlation of Yagi et al. [195], especially for temperatures below 800 K. The results for the particle-to-fluid heat transfer coefficient and pressure gradient are in between the empirical correlations.

Overall, the validation shows a good accordance of the simulation results to the empirical correlations, especially considering the deviations among the correlations themselves. As expected, the deviations are larger for the polydisperse laser-scanned crushed rock shapes, probably due to the larger number of influential quantities.



a / Hamburg-Altenwerder, Germany.



b / Hamburg-Bergedorf, Germany.

**Figure 5.3 /** Pictures of packed-bed storage units used for validation .

## 5.2 One- and Three-Dimensional Packed-Bed Storage Models

Besides the ETES demonstration plant in Hamburg-Altenwerder, as already described in Section 3.4, measurement results of a smaller test site in Hamburg-Bergedorf operated by Siemens Gamesa Renewable Energy as well is used for validation of the one- and three-dimensional packed-bed models. The packed-bed storage of the test site in Hamburg-Bergedorf is charged with exhaust gas at  $600\text{ }^{\circ}\text{C}$ . The thermal storage capacity is  $5\text{ MWh}_{\text{th}}$ . Pictures of both thermal energy storage units are shown in Figure 5.3.

The storage units are equipped with many temperature measurement points inside the packed bed. They are distributed on a center line along the horizontal main flow direction and furthermore in radial direction towards the insulation at several cross-sections. The pressure is measured at the in- and outlet of the storage unit.

In order to compare the packed-bed temperature field of the one- and three-dimensional models with the measured temperatures, the mean temperature along the main flow direction is used. It is calculated from the three-dimensional temperature fields of the CFD simulation and measurement data by averaging all values in perpendicular directions to the main flow. Each temperature sensor or cell value is weighted according to his surface share of the respective packed-bed cross section.

A stationary thermal insulation is used for the one-dimensional model in order to increase the comparability to the three-dimensional model and as the correct initialization of the dynamic insulation model requires a high resolution of temperature measurement points. Both models use packed-bed correlations determined from particle-resolved CFD simulation. Approximately 150 cells are used in the main flow direction of the CFD model.

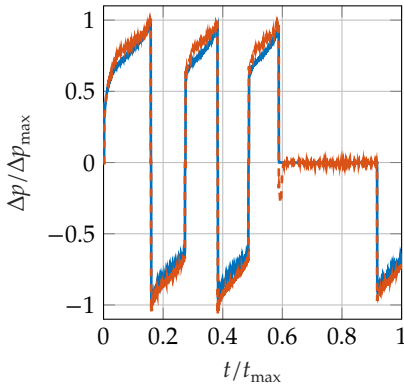
Figure 5.4 shows a comparison of simulation results from the one- and three-dimensional packed-bed models with measured data from the test site in Hamburg-Bergedorf. Data of three full cycles with a hold period within the last cycle is used. The pressure inlet minus the pressure outlet of the storage unit is shown as well as the mean temperature in the main flow direction at three different points in time.

The pressure loss is under-predicted by the one-dimensional model with a mean absolute error at 4.4 % of the maximum measured pressure difference, whereas it is over-predicted by the three-dimensional model with an error of 6.6 %.

The one-dimensional temperature field inside the packed bed of the test site is simulated with a mean absolute error at 5.9 % of the maximum measured temperature after three full cycles and the hold period with the one-dimensional model and 5 % with the three-dimensional model. The temperature field deviations after the hold period at  $t_2$  indicate an under-estimation of the test site heat losses through the thermal insulation with both models. The thickness of the thermocline region is also under-estimated with both models at  $t_1$  and  $t_3$ , which are at the end of discharge operations.

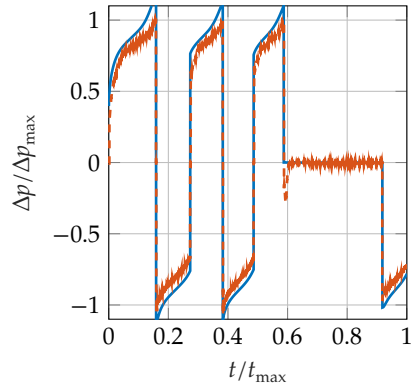
Figure 5.5 shows simulation results from the one- and three-dimensional packed-bed models for a single charge operation of the storage unit of the ETES demonstration plant in Hamburg-Altenwerder. The short break of the charge process has been due to technical reasons.

For the demonstration plant, the pressure loss is significantly under-predicted by the one-dimensional model with a mean absolute error of 26 % of the maximum measured pressure difference. The pressure loss of the three-dimensional model is closer, but still has an error of 21 %. Main reason is that the measured pressure loss includes the in- and outlet sections of the storage unit, which are not included in both models at validation, as a value for the nominal pressure



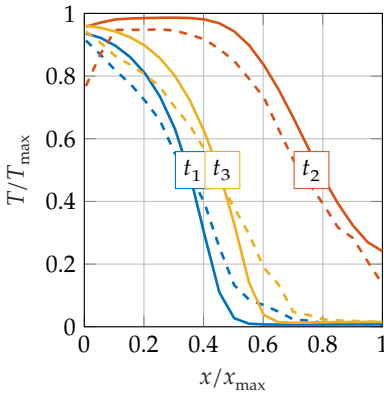
— SIM (MAE = 4.4%) - - - MEAS

a / 1D Model: Pressure Loss.



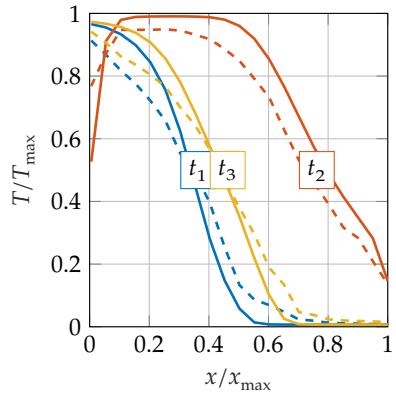
— SIM (MAE = 6.6%) - - - MEAS

b / 3D Model: Pressure Loss.



— SIM(MAE = 5%) - - - MEAS  
 — SIM(MAE = 8.2%) - - - MEAS  
 — SIM(MAE = 5.9%) - - - MEAS

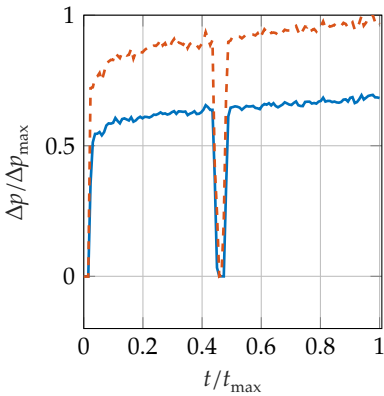
c / 1D Model: Temperature along main flow direction at  $t_1 = 0.48$ ,  $t_2 = 0.88$  and  $t_3 = 1$ .



— SIM(MAE = 5.8%) - - - MEAS  
 — SIM(MAE = 8.6%) - - - MEAS  
 — SIM(MAE = 5%) - - - MEAS

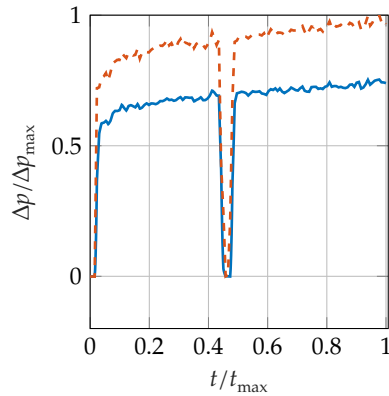
d / 3D Model: Temperature along main flow direction at  $t_1 = 0.48$ ,  $t_2 = 0.88$  and  $t_3 = 1$ .

**Figure 5.4 /** Simulations results of one- and three-dimensional models in comparison with measured data from the test site in Hamburg-Bergedorf for three full cycles with an hold operation within the last cycle. All values, including the MAE, are relative to the maximum measured value (MAE = 5% meaning 5% of the maximum value). The time is relative to the measurement time .



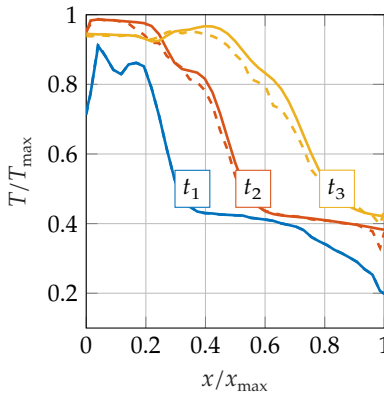
— SIM (MAE =26%) - - - MEAS

**a / 1D Model: Pressure Loss.**



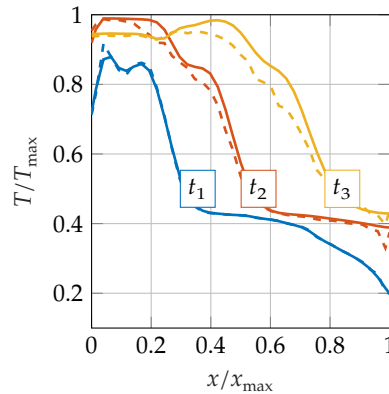
— SIM (MAE =21%) - - - MEAS

**b / 3D Model: Pressure Loss.**



— SIM - - - MEAS  
 — SIM(MAE =1.4%) - - - MEAS  
 — SIM(MAE =2.1%) - - - MEAS

**c / 1D Model: Temperature along main flow direction at  $t_1 = 0$ ,  $t_2 = 0.46$  and  $t_3 = 1$ .**



— SIM - - - MEAS  
 — SIM(MAE =2%) - - - MEAS  
 — SIM(MAE =3%) - - - MEAS

**d / 3D Model: Temperature along main flow direction at  $t_1 = 0$ ,  $t_2 = 0.46$  and  $t_3 = 1$ .**

**Figure 5.5 /** Simulations results of one- and three-dimensional models in comparison with measured data from the demonstration plant in Hamburg-Altenwerder for a single charge with a short break. All values, including the MAE, are relative to the maximum measured value (MAE = 5% meaning 5% of the maximum value). The time is relative to the measurement time .

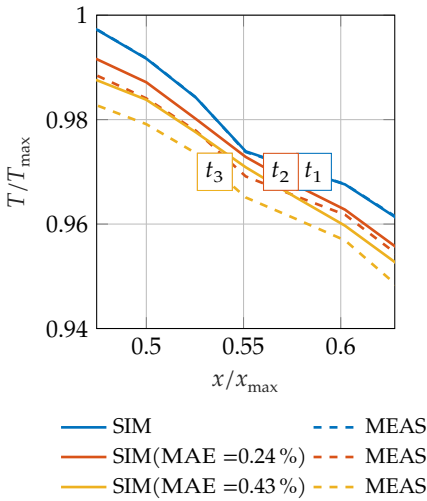
loss of the in- and outlet section has not been independently measured and model calibration to the measured data is avoided. Separate CFD simulations of the in- and outlet sections showed pressure losses for both together at 15 to 23 % of the overall storage unit pressure loss and thus match the deviation. Another possible reason for the deviation could be a packed-bed porosity reduction during operation due to the thermal expansion of the rocks and resulting packed bed settling behavior.

A growing trend of error over time can be observed for the one-dimensional temperature field in the packed-bed storage unit of the demonstration plant. Nevertheless, the mean absolute error is at 2.1 % of the maximum measured temperature for the one-dimensional model and at 3 % for the three-dimensional model at the end of the charge period.

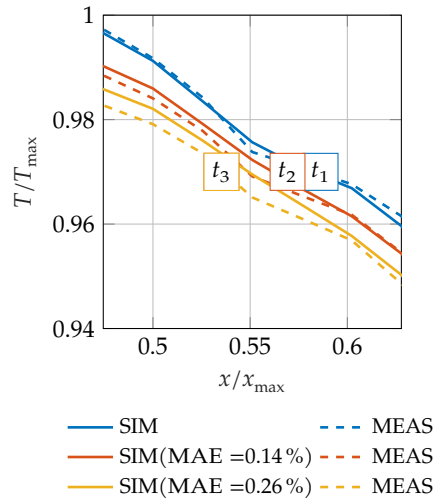
Simulation results for the temperature field in the packed-bed storage unit of the ETES demonstration plant in Hamburg-Altenwerder during a hold operation of three days are compared to measured values in Figure 5.6. Two sections of the temperature field along the main flow direction are shown, namely in the center and close to the packed-bed outlet on the hot side.

As can be seen from the central section of the packed bed, the heat losses through the storage unit insulation are taken into account more accurately with the three-dimensional model.

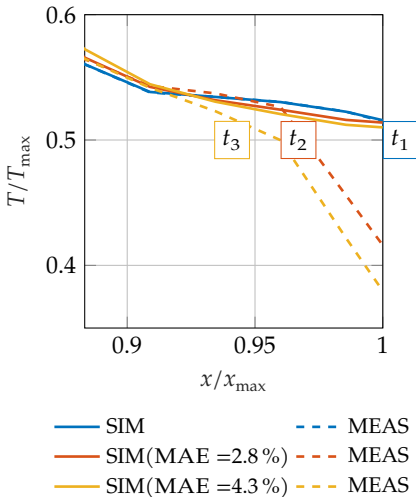
An intrusion of cold air into the lower part of the packed bed due to natural convection at the in- and outlet is observable for horizontal-flow packed-bed storage designs at hold operation. The effect has also been described by Bejan [22] and Bejan et al. [23]. The ability to represent the resulting temperature drop in the vicinity of the packed-bed in- and outlet during hold operation is an advantage of the three-dimensional packed-bed model. It can simulate the mean temperature along the main flow direction in the considered section with a mean absolute error of 2.1 % of the maximum measured temperature, whereas the one-dimensional model does not account for it under the used assumptions. The Rayleigh number according to Equation 2.56 is 40 at the end of hold operation.



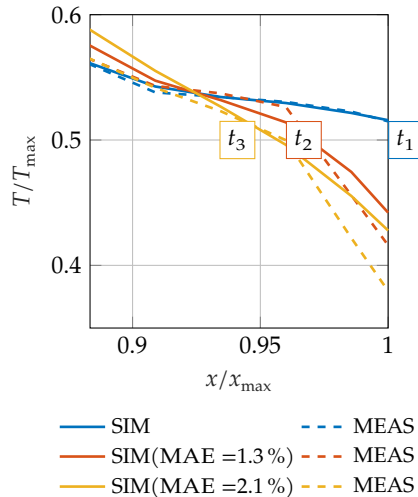
**a / 1D Model:** Temperature along central part of main flow direction at  $t_1 = 0$ ,  $t_2 = 0.5$  and  $t_3 = 1$ .



**b / 3D Model:** Temperature along central part of main flow direction at  $t_1 = 0$ ,  $t_2 = 0.5$  and  $t_3 = 1$ .



**c / 1D Model:** Temperature along main flow direction close to hot side at  $t_1 = 0$ ,  $t_2 = 0.5$  and  $t_3 = 1$ .



**d / 3D Model:** Temperature along main flow direction close to hot side at  $t_1 = 0$ ,  $t_2 = 0.5$  and  $t_3 = 1$ .

**Figure 5.6 /** Simulations results from the one- and three-dimensional models in comparison with measured data from the demonstration plant in Hamburg-Altewerder at a hold operation of 3 days. All values, including the MAE, are relative to the maximum measured value (MAE = 5 % meaning 5 % of the maximum value). The time is relative to the measurement time.

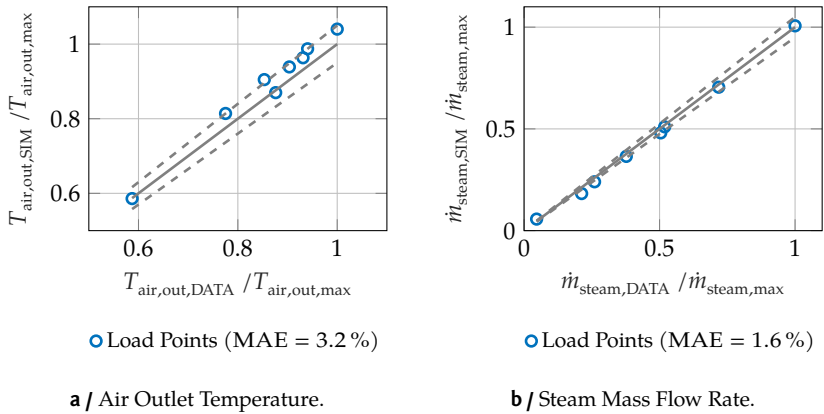


**Figure 5.7 /** Comparison of stationary simulation results for the HRSG air outlet temperature and steam mass flow with manufacturer's specifications at eight different load points with respect to air inlet temperature and air mass flow. The dotted lines mark the  $\pm 5\%$  deviation range.

### 5.3 Heat Recovery Steam Generator and Fan Models

A comparison of stationary simulation results from the simple pinch-point based HRSG model, as introduced in Section 4.2.4, with manufacturer's specification for the HRSG of the ETES demonstration plant in Hamburg-Altewerder is shown in Figure 5.7. Eight different load points with respect to air inlet temperature and air mass flow rate are compared.

As shown, the stationary air outlet temperature and steam mass flow rate are simulated with a relative error approximately in the range of  $\pm 5\%$  for all specified load points. The representation of HRSG part load behavior is thus considered satisfactory for this work.

Stationary simulation results, determined with the polytropic efficiency based fan model, are compared to manufacturer's specifications for the fan included in the ETES demonstration plant at six different load points in Figure 5.8. The load points include three volume flow rates at two different air inlet temperatures.

The relative error for all load points is in the range of  $\pm 20\%$ . One reason is the

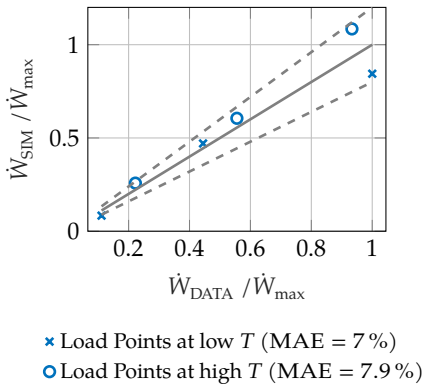


**Figure 5.8 /** Comparison of stationary simulation results for the fan power demand  $\dot{W}$  with manufacturer's specifications for six different load points with respect to inlet temperature and volume flow rate. The dotted lines mark the  $\pm 20\%$  deviation range.

utilization of a constant polytropic efficiency at different air inlet temperatures and thus densities. Nevertheless, the fan model is used in this work for its simplicity and numeric robustness, but the precision at validation has to be kept in mind at evaluation of the simulation results.



# Chapter 6

## Results

In this chapter the system simulation and CFD models are applied to a selection of test cases in order to evaluate the ETES air cycle performance. The interplay of modeling scales follows the relations outlined in Figure 4.1. After an introduction to the test cases, the packed-bed property correlations, as determined particularly for horizontal-flow rock beds with the DEM-CFD workflow, are presented. The influence of the storage unit aspect ratio, storage material particle size, outlet temperature deviation tolerance at charge and insulation thickness on the air cycle performance is shown for some test cases as example. Furthermore, simulation results of one- and three-dimensional packed-bed models are compared over a simulation period of two months to verify the applicability of the one-dimensional packed-bed model for horizontal-flow packed-bed TES at irregular operation and large scale. Finally, the air cycle efficiency and usable capacity ratio are compared among the test cases, using the energy loss classification according to Section 3.7 for the discussion.

### 6.1 Definition of Test Cases

The ETES test cases used in this work are defined by selection of unit size, way of energy system integration and operational schedule. A combination of

**Table 6.1** / Nominal values for the live steam temperature  $\vartheta_{\text{nom,steam}}$ , live steam pressure  $p_{\text{nom,steam}}$ , feedwater temperature  $\vartheta_{\text{nom,fw}}$  and charge temperature  $\vartheta_{\text{nom,c}}$  of all test cases.

System Integration	$\vartheta_{\text{nom,steam}}$ °C	$p_{\text{nom,steam}}$ bar	$\vartheta_{\text{nom,fw}}$ °C	$\vartheta_{\text{nom,c}}$ °C
P2P	500	65	120	750
P2H	150	5	20	600

energy system integration and operational schedule is also referred to as an application case.

The sizing of ETES units depends on the nominal rate of charge and discharge of the packed-bed storage in the first place, as it sets the size of all air cycle components besides the packed-bed storage unit itself. Two different units with a nominal rate of charge and discharge at 5 and 30 MW are analyzed in this thesis. The smaller unit is at a similar scale compared to the ETES demonstration plant in Hamburg-Altenwerder and the larger at a scale anticipated as reasonable for an upcoming pilot plant. The system parameters for both units, as used in this work, are shown in Table A.1.

Furthermore, two exemplary ways of ETES energy system integration are analyzed in this chapter. These are

1. Power-to-Power (P2P) operation for an application as standalone EES unit without any opportunity to cogenerate heat and power and
2. Power-to-Heat (P2H) operation to supply an industrial consumer of process heat without any means of re-electrification.

The operating temperatures are different at P2P and P2H. The nominal values for both ways of energy system integration, as analyzed in this work, are shown in Table 6.1. The nominal charge temperature of the packed-bed storage is set well above the required live steam temperature in order to obtain an operational margin to the required HRSG air inlet temperature, as explained in Section 3.2, and to increase the volumetric energy storage density.

## Operational Schedules

The operational schedule defines the set point values for the electric power intake at charge and rate of heat transfer in the HRSG at discharge over time. Whereas both are time-variant at power-to-power operation in order to balance VRE electricity generation and demand, the set point for the rate of discharge is constant in the case of power-to-heat operation, as the steam shall be provided to a constantly running industrial process whenever possible. The resulting course of the packed-bed storage state of charge over the simulation time, resulting from each of the five operational schedules in power-to-power operation, is shown in Figure A.1.

Only few studies are available in literature with respect to irregular operation of packed-bed TES. McTigue et al. [121] studied the effect of cycle duration perturbations on the usable capacity ratio. They found that the usable capacity ratio recovers in one or two cycles after the perturbation for a storage operation with a fixed outlet temperature deviation tolerance.

Two different irregular schedules are used in this work in order to represent realistic operating conditions to an energy storage application for VRE balancing. These are based on time-series data for the residual load and wholesale electricity price. The data for both schedules is provided by the German federal network agency [66]. January and July of the year 2019 are chosen as observation time period in order to include a summer and winter month, which reflects the prevalence of wind energy in Germany in winter and the characteristic variation of PV electricity generation and demand in summer.

In the residual load based schedule, the ETES unit is set to charge, if the residual load, which is defined here as the electricity generation from WEC and PV minus the electricity demand, is positive. At power-to-power operation, the ETES unit is set to discharge, if the residual load is negative. In order to represent a future scenario with an increase in installed PV and WEC capacity and thus variability of residual load, the German electricity generation from wind and solar energy of the year 2019 is scaled by a factor of two, which corresponds to the required installed capacity for the year 2030 according to the Fraunhofer Institut für Solare Energiesysteme ISE[63].

In the wholesale electricity price based case, a charge of the ETES unit is

initiated, if the price falls below a threshold of 80 % of the monthly mean price. According to the limited power ramp rate, a discharge is initiated at power-to-power operation, if the wholesale price is above a threshold of 120 % of the monthly mean price for the next six hours. These thresholds are chosen for the results of this work, as the wholesale price spread in the data set would not allow an economic operation anyways and increasing price spreads are expected at a higher installed capacity of PV and WEC.

Furthermore, three cyclic schedules are used in this work in order to increase the comparability to other works. Unfortunately, to the author's knowledge, no normative energy storage operational schedules exist. Thus two simple regular operational schedules are defined based on characteristic solar and wind energy fluctuations.

The cyclic solar-based schedule is created according to a typical diurnal variation of PV electricity generation and demand, commonly known as *California Duck Curve* [31]. The storage is charged from 09:00 to 17:00 every day at high PV generation. In the case of power-to-power operation, the storage is discharged from 18:00 to 22:00, at peak electricity demand.

The cyclic wind-based schedule is less universal, as the variation of WEC electricity generation is not as regular as the electricity generation from PV. According to Weber et al. [190], the persistence time statistics of wind power are not well understood yet. A period of five consecutive days with an average wind capacity factor below 10 % happens once a year in Germany whereas time periods of 24 h with an average wind capacity factor below 10 % happen approximately ten times per year on average [137]. A series of 2 day charge, 2 day hold, 4 day discharge and again 2 day hold is used at power-to-power operation in this work. At power-to-heat operation, the schedule leads to a two-day charge per ten days of cycle duration.

The set-point power values for one operational cycle of the solar- and wind-based schedules at a power-to-power application case are shown in Figure 6.1. Ten consecutive cycles are simulated for all three cyclic schedules, which leads to an observation time period of 10 days in the solar- and 100 days in the wind-based case.

The set point for the rate of charge and discharge is constantly at the nominal point while in operation for both irregular schedules and the cyclic full charge

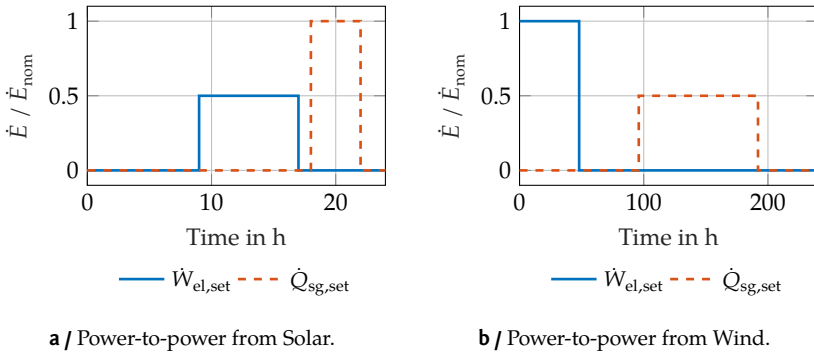


**Figure 6.1 /** Cyclic operational schedules for ETES units based on characteristic wind and solar energy availability variations for power-to-power operation.

and discharge operation at power-to-power applications. Thus, no part load occurs. At power-to-heat operation, the rate of discharge is reduced in order to

- achieve a higher coverage of the industrial steam demand over time and
- account for the reduced rate of charge of the packed-bed storage due to concurrent steam generation during charge.

### Packed-Bed Dimension

According to each operational schedule, a nominal discharge duration  $\Delta t_{nom,d}$  for each test case can be defined, which is

- 4 h for the solar-based schedule in power-to-power operation and 16 h in power-to-heat operation,
- 24 h for the time-series-data based operational schedules as well as the cyclic full charge and discharge in power-to-power and power-to-heat operation and
- 96 h for the wind-based schedule in power-to-power operation and 192 h in power-to-heat operation.

Using the nominal discharge duration, the packed-bed volume is dimensioned

for each test case individually as

$$V_{\text{bed}} = \frac{\dot{Q}_{\text{sg,set}} \Delta t_{\text{nom,d}}}{\rho_p (1 - \varepsilon) (u_p(T_{\text{nom,c}}) - u_p(T_{\text{nom,d}}))}. \quad [6.1]$$

The resulting packed-bed volumes range from 75 m<sup>3</sup> for the 5 MW unit at a solar-based operation to 5400 m<sup>3</sup> for the 30 MW unit at wind-based operation.

A rectangular storage unit shape is used for all test cases with a horizontal main air flow direction. The storage unit is filled with crushed rocks, whose thermodynamic properties are taken from Table 4.1. The packed-bed height is limited to 10 m, according to the allowable mechanical stress on the particles and storage containment, as explained in Section 2.6.

## 6.2 Packed-Bed Properties at Horizontal Flow

The DEM-CFD workflow, as presented in Section 4.4, is used to determine the packed-bed properties particularly for horizontal-flow packed-beds of crushed rock in the necessary operating range and air as heat transfer fluid.

Main reason is that, according to Allen et al. [8], the relative orientation of packing and flow direction in a packed bed of crushed rock can alter the packed-bed pressure drop up to 80 %, as irregularly shaped particles tend to orientate with flat surfaces towards the ground at the packing process. Consequently, the pressure drop in horizontal-flow packed beds may be significantly over-estimated, when applying a correlation taken from an experiment with vertical flow direction. Besides the pressure drop, the particle orientation also affects the effective thermal conductivity at stagnant fluid, which thus varies in horizontal and vertical temperature gradient direction accordingly.

Table 6.2 shows the determined constants for the packed-bed property correlations used in this work for horizontal-flow packed beds of crushed rock. The particle size distribution of Figure 4.17, and all 20 available rock shapes, as de-

**Table 6.2** / Packed-bed properties determined from particle-resolved CFD simulation for crushed rocks with a particle size distribution as shown in Figure 4.17 and horizontal flow. The porosity is 0.41 and the mean sphericity according to Equation 2.24 is 0.81.

Property	Correlation	Constants		
		$B_1$	$B_2$	$B_3$
Eu	Equation 4.19	158	2.62	
$Nu_{p-f}$	Equation 4.21	2.93	0.349	0.645
$\alpha_{eff}/\alpha_{p-f}$	Equation 4.22	5.96		
$k_{eff,o}$	Equation 4.23	0.31	-0.0124	421

terminated from laser scanning, are used. The correlations validity is restricted to ambient pressure, which is in accordance with the ETES operation. In accordance with the validation, a constant thermal conductivity of  $2 \text{ W}/(\text{m K})$ , a density of  $2500 \text{ kg}/\text{m}^3$  and an emissivity of 0.85 is used as material properties at the determination of the packed-bed property correlations. The temperature dependent air properties are interpolated from data of the *VDI Heat Atlas* [13].

Figure 6.2 shows exemplary sections of the temperature and velocity field on a cut-plane section for a Reynolds number of 2500. The velocity field shows the fluid acceleration in narrow channels between particles. The radial temperature gradient inside the irregularly shaped solid particles is visible in the temperature field. Furthermore, the alignment of several flat particles can be detected.

In Figure 6.3, the pressure gradient at  $20^\circ\text{C}$  and the effective thermal conductivity in horizontal ( $x$ ) air flow and temperature gradient direction, as determined with the packed-bed correlations of Table 6.2, are compared to the properties in vertical direction ( $z$ ), as determined with the packed-bed correlations shown in Figure 5.2. The relative difference of the properties in both directions is used as measure for the comparison.

According to the CFD simulation results, the pressure gradient is lower at horizontal air flow direction, especially at higher velocities. The difference is between 5% at a superficial air velocity of  $0.01 \text{ m}/\text{s}$  and 19% at  $1 \text{ m}/\text{s}$ . The difference is not as large as measured by Allen et al. [6], but the particle size,

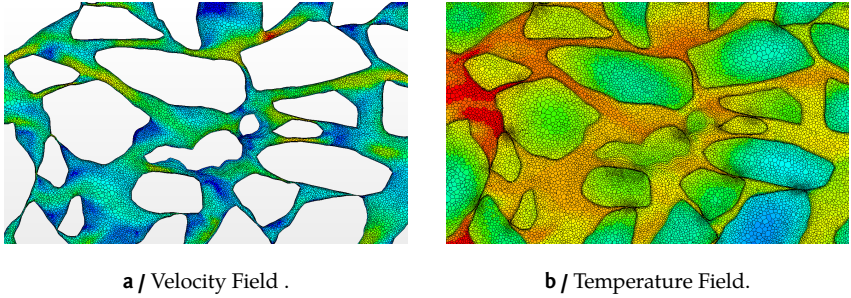


**Figure 6.2** / Exemplary cut-plane sections of the temperature and velocity field at  $Re = 2500$ . The flow is from left to right, gravity is downwards, the velocity ranges from 0 m/s (blue) to 20 m/s (red) and the temperature ranges from 600 K (blue) to 670 K (red) .

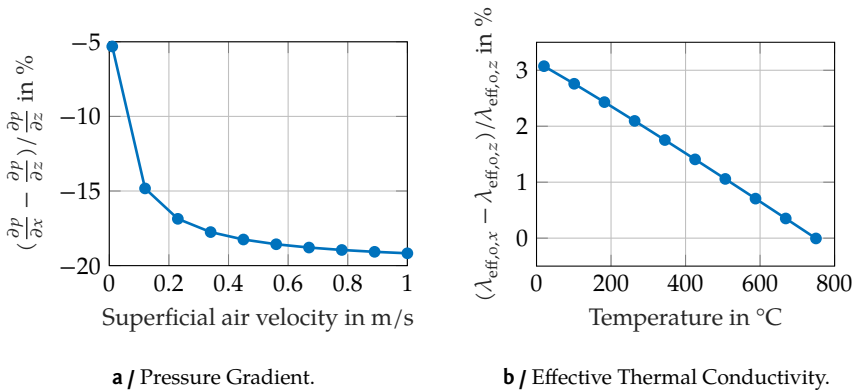


**Figure 6.3** / Comparison of the local pressure gradient at 20°C and effective thermal conductivity at stagnant fluid in horizontal ( $x$ ) and vertical ( $z$ ) air flow or temperature gradient direction for a packed bed of crushed rock.

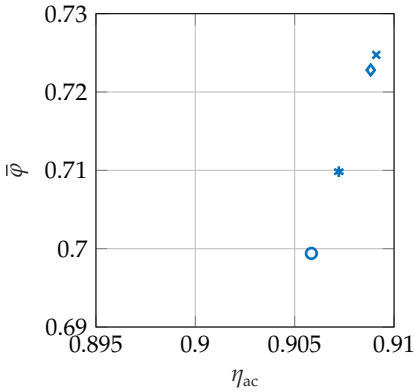
porosity and shape is also different from their experiments. The particle-to-fluid heat transfer coefficient is increased along with the pressure gradient according to the analogy of frictional pressure drop and heat transfer, but the increase is smaller and less significant to the ETES performance and thus not further discussed here.

In contrast to the pressure loss, the effective thermal conductivity at stagnant fluid is higher at a horizontal thermal gradient in comparison to a vertical gradient. Reason is, that the alignment of irregularly shaped particles reduces the influence of the particle contact point thermal resistance in horizontal direction at low temperatures. But the difference is 3 % at most for the tested particle shapes according to the CFD simulation results. At higher temperatures, the radiant heat transfer is increasingly dominant and diminishes the difference.

It must be noted, that as the roundness of the particles is the main reason for the alignment and thus variation of packed-bed properties with the direction of air flow and temperature gradient, the influence of the packing direction may alter significantly for differently shaped particles.

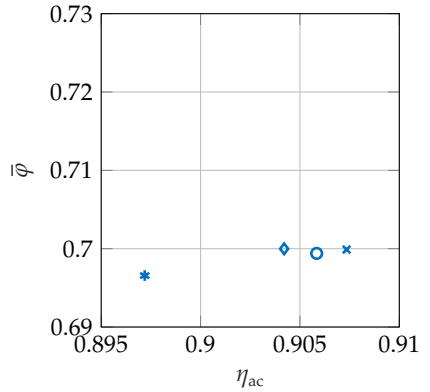
The sensitivity of the packed-bed mean usable capacity ratio and air cycle efficiency, as defined in Equations 3.7 and 3.11 and determined with the one-dimensional packed-bed model, to the packed-bed body force and ETC correlation is shown in Figure 6.4, comparing the correlations determined by particle-resolved CFD simulation for horizontal and vertical flow with correlations from literature. A 30 MW-ETES unit in a power-to-power application and a cyclic full charge and discharge operation is used for the analysis. An additional 24 h hold is added between each operation phase for this specific analysis, in order to demonstrate the relevance of the ETC.

As expected, the ETC correlation mainly affects the usable capacity ratio, whereas the packed-bed body force mainly affects the air cycle efficiency due to the according fan work. But, the sensibility of the efficiency on the packed-bed body force is low, due to the low storage unit aspect ratio, as further discussed in Section 6.3, and the closed ETES system. Even though the correlation of Macdonald et al. [115] is explicitly dedicated to particles with rough surfaces such as crushed rocks, the efficiency determined with the properties of Table 6.2 for a horizontal flow direction is closer to the efficiency determined with the correlation of Ergun [57].



- Table 6.2
- × Zehner et al. [200]
- \* VDI Heat Atlas [13, section Mh]
- ◇ Equation 2.50

a / Effective thermal conductivity.



- Table 6.2
- × Ergun [57]
- \* Macdonald et al. [115]
- ◇ Figure 5.2

b / Packed-bed body force.

**Figure 6.4** / Sensitivity of air cycle efficiency and mean usable capacity ratio on the used ETC and packed-bed body force correlation for a 30 MW ETES unit with a nominal discharge duration of 24 h. The schedule consists of full charge and discharge operations with 24 h hold after each operation.

## 6.3 Selection of Particle Size and Storage Aspect Ratio

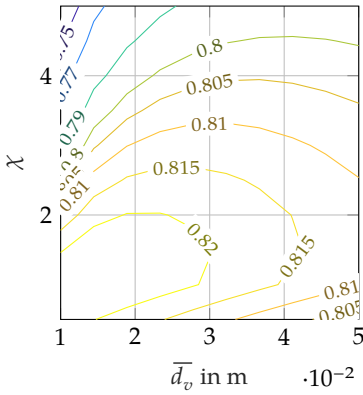
The particle size and packed-bed aspect ratio, as defined in Equations 2.19 and 2.21 are important design parameters for axial-flow packed-bed TES, as they significantly affect the usable capacity ratio as well as the heat and pressure losses. The aspect ratio sets the air velocity in the packed bed at the same rate of charge or discharge and thermal storage capacity. Simulation studies with varying particle size or aspect ratio have been done by several authors for packed-bed TES, as already reviewed in Section 2.6, but the influence with the specific background of the ETES concept is yet uncertain.

A sensibility analysis is thus required in order to ensure that the ETES performance does not suffer from an arbitrarily chosen particle size and packed-bed aspect ratio. In this work, both parameters are varied at the same time in order to show their interdependence, as the effects of the packed-bed aspect ratio and mean particle size are entangled.

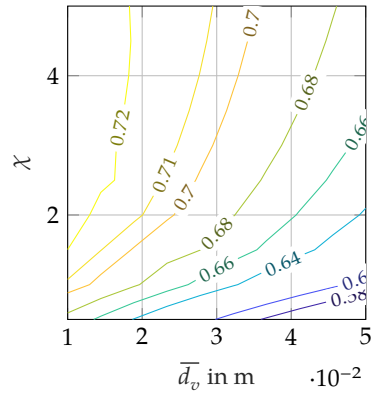
Besides the particle size and aspect ratio, the ETES air cycle efficiency and packed-bed storage usable capacity ratio furthermore depend on the

1. way of energy system integration, as for example the electricity intake at discharge is valuated differently at power-to-power and power-to-heat operation,
2. operational schedule, for example due to the frequency and length of hold operations,
3. unit size, as for example larger units are less prone to heat losses and
4. further design parameters, such as for example the thermal insulation thickness.

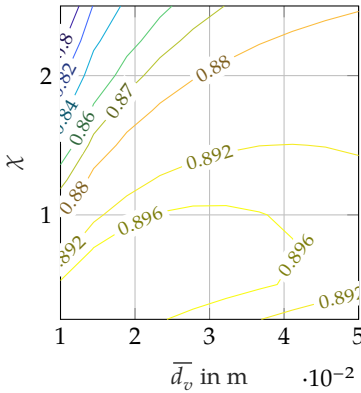
As the interdependence of all these influential quantities is not clear, the optimal aspect ratio and particle size should be determined for each test case individually. Simulation results for the packed-bed storage usable capacity ratio and efficiency of the 5 and 30 MW designs at the residual load based operational schedule and power-to-power operation are shown for different aspect ratios and particle sizes in Figure 6.5 as example.



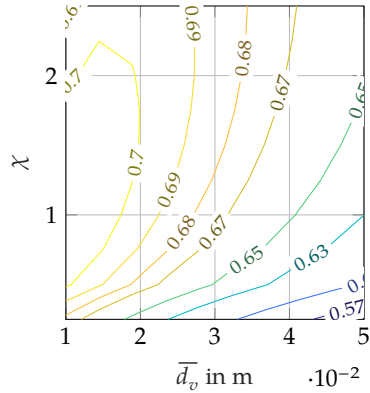
a / Air cycle efficiency  $\eta_{ac}$  for 5 MW unit.



b / Mean usable capacity ratio  $\bar{\varphi}$  for 5 MW unit.



c / Air cycle efficiency  $\eta_{ac}$  for 30 MW unit.



d / Mean usable capacity ratio  $\bar{\varphi}$  for 30 MW unit.

**Figure 6.5** / Air cycle efficiency and packed-bed storage mean usable capacity ratio at different aspect ratios  $\chi$  and mean volume-equivalent particle diameter  $\bar{d}_v$ . The results for the 5 and 30 MW size are compared at power-to-power operation and an operational schedule based on time-series data for the residual load. 100 simulation runs have done for each unit. Note the different aspect ratio range.

It is obvious, that the ETES air cycle efficiency in power-to-power operation decreases at high aspect ratios and small particle sizes due to the increasing packed-bed pressure loss and thus high fan energy demand at discharge. On the other hand, the packed-bed usable capacity ratio decreases at low aspect ratios and large particle sizes, as the internal heat losses and thus thermal destratification increases. In combination, this leads to a conflict of goals.

At packed-bed deployment in the closed ETES system two further effects are relevant:

- The usable capacity ratio decreases at high aspect ratios and small particle sizes, as the storage air inlet temperature increases due to the resulting high packed-bed pressure loss and thus increased fan energy demand and fan air outlet temperature.
- The air cycle efficiency decreases at low aspect ratios and large particle sizes, as the reduced usable capacity ratio limits the energy turnover in the observation time period and thus increases the significance of self-discharge and standby losses.

In order to identify an optimal design solution with respect to both, efficiency and usable capacity ratio, the levelized cost of storage, as defined in Equation 2.14, can be used if the specific values for the charge and capital cost are given.

The comparison of the 5 and 30 MW unit performance shows that the optimal aspect ratio at equal particle size is generally lower for the 30 MW unit. Reason is the packed-bed pressure loss, which depends on the mean superficial air velocity in the packed bed along with the packed-bed length. When comparing units of different volume at the same aspect ratio, the larger unit is longer and leads to a higher superficial air velocity at the same time. In order to keep the superficial air velocity and packed-bed length constant, a scaling law of  $A_{\text{cross}} \propto \dot{Q}_{\text{nom}}$  can be used, which leads to a decreasing aspect ratio with packed-bed volume.

The simulation results also show, that the effects of particle size and aspect ratio on the ETES performance partly compensate each other. Thus, several combinations may lead to a similar performance. Notably, low aspect ratios increase the necessary constructional effort and cost for the in and outlet

sections of the storage unit, especially with respect to an even flow distribution inside the packed bed, which is not taken into account in this analysis.

In consequence, a storage unit aspect ratio of  $\chi = 1$  and 0.5 for the 5 MW and 30 MW units at power-to-power operation is used, as well as an aspect ratio of 1.5 and 1 at power-to-heat operation respectively. A volume-equivalent particle diameter of 0.02 m is used for all test cases.

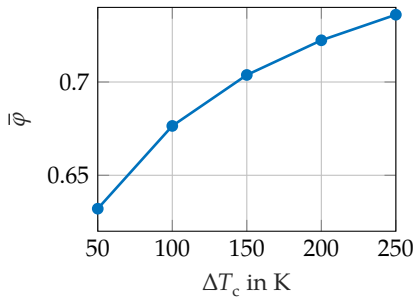
According to the chosen aspect ratio as well as the unit size and operational schedule, the mean superficial air velocity inside the packed bed at nominal charge temperature and rate of charge or discharge varies significantly among the test cases. Whereas it is approximately 0.14 m/s at discharge in the case of power-to-power operation and wind-based operational schedule with the 5 MW unit, it is 1.7 m/s at discharge for the solar-based power-to-power operation of the 30 MW unit. The resulting peak packed-bed pressure loss in the observation period for these test cases is 8 and 46 mbar.

## 6.4 Selection of Storage Outlet Temperature Deviation Tolerance

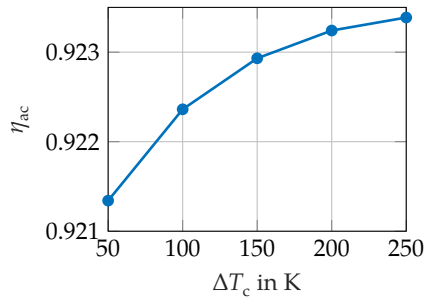
Further design parameters which significantly affect the air cycle performance are the storage outlet temperature deviation tolerances at charge and discharge. They must be chosen carefully in order to optimize the usable capacity ratio along with the efficiency [29, 135]. The application of variable deviation tolerances has been evaluated for a CSP plant by Fasquelle et al. [61], but fixed values are assumed in this work.

In the case of ETES, the deviation tolerance at discharge is strictly limited by the minimum required HRSG air inlet temperature. It is thus set to 200 K in this work, according to the chosen operating temperatures.

The optimum deviation tolerance at charge is limited by the rated fan power, which must be high enough to ensure the required air mass flow at low air enthalpy differences across the packed-bed storage, as already encountered in Section 3.2. Furthermore, the components on the cold side of the ETES system



a / Mean usable capacity ratio.



b / Air cycle efficiency.

**Figure 6.6 /** Effect of the storage outlet temperature deviation tolerance at charge on the mean usable capacity ratio and air cycle efficiency in the observation time period for the 30 MW unit at cyclic full charge and discharge power-to-power operation.

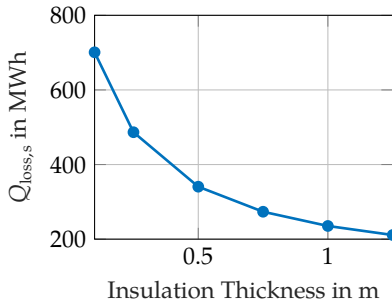
and the electric heater must tolerate the increased temperature. Both criteria are of an economic nature.

The variation of mean packed-bed storage usable capacity ratio and air cycle efficiency with the temperature deviation tolerance at charge is shown in Figure 6.6 for the 30 MW unit at power-to-power operation and cyclic full charge and discharge. For this analysis, the fan is dimensioned large enough to always maintain the electric power set point of the ETES unit.

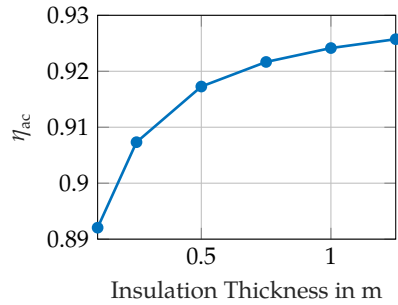
The mean usable capacity ratio increases with the temperature deviation tolerance, as expected. Thus also the equivalent number of full cycles and energy turnover per observation time period increase.

The air cycle efficiency increases as well, due to the reduction of self-discharge and standby losses caused by the higher energy turnover. Notably, the increasing air outlet temperature of the packed-bed storage at charge does not limit the air cycle efficiency, as the system is closed. Furthermore, the fan energy demand, which increases with the operating temperature, does not limit the air cycle efficiency either because the technical work of the fan is stored as thermal energy in the packed bed, as already encountered in Section 3.7.

Accordingly, a high temperature deviation tolerance at charge is generally beneficial from a thermodynamic point of view. Nevertheless, the storage



a / Packed-Bed Storage Heat Loss.



b / Air cycle efficiency.

**Figure 6.7 /** Variation of packed-bed storage transmission heat loss and air cycle efficiency in the observation period with the inner insulation layer thickness of the packed-bed storage for the 30 MW unit at power-to-power operation and wind-based operational schedule.

outlet temperature deviation tolerance at charge is set to 150 K for all test cases in this work due to the mentioned economic reasons.

## 6.5 Selection of Packed-Bed Storage Thermal Insulation Thickness

The heat losses of the packed-bed storage can be reduced by thermal insulation, which on the other hand increases the cost and requires space. Two insulation layers are used in this work for the packed-bed storage model, which are made of aerated and lightweight concrete. An ideal case with uniform insulation thickness and without any thermal bridges is assumed. Figure 6.7 shows the results of an inner aerated concrete layer thickness variation on the packed-bed storage transmission heat losses and air cycle efficiency for the 30 MW unit at power-to-power operation and wind-based operational schedule. The outer lightweight concrete layer thickness is kept at 0.5 m for this analysis.

As shown, the effort to further reduce the transmission heat losses increases with the installed insulation layer thickness. Generally, the insulation thickness should be chosen for each test case individually according to economic design

optimization. Nevertheless, an aerated concrete layer thickness of 0.5 m is used in this work for all test cases in order to keep the comparability.

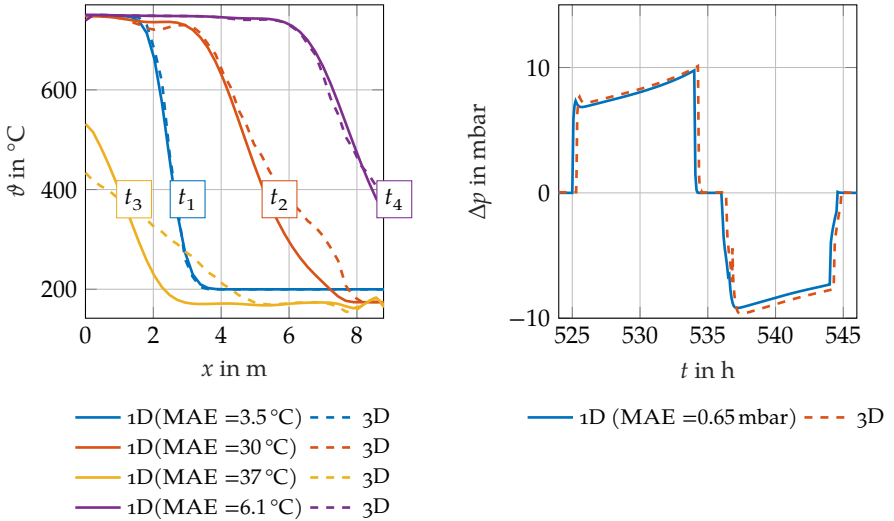
## 6.6 Comparison of One- and Three-Dimensional Storage Models

Three-dimensional CFD simulation, as described in Section 4.3, is used in this work to verify the applicability of the one-dimensional packed-bed model, as experimental results are not available for packed beds larger than the storage unit of the demonstrator plant. In order to detect deviations, that might accumulate in the long run, a simulation time of two months is used in the CFD simulation as well. To limit the calculation time, the number of cells in the main flow direction of the CFD model is reduced to 100.

As the strength of natural convection depends on the packed-bed permeability, the operating conditions and the storage unit size and shape, which is also evident from the Rayleigh number definition in Equation 2.56, the applicability of the one-dimensional model must be verified for each test case individually.

Results of a one- and three-dimensional model comparison are shown as example in Figure 6.8 for the 30 MW unit at power-to-power operation and the wholesale electricity price based schedule. The figure shows the mean temperatures along the main flow direction in both packed-bed storage models at four different points of time  $t_{1-4}$ , as well as the pressure drop for a consecutive charge and discharge operation between  $t = 524$  h and  $t = 546$  h. The points of time used for the comparison of the temperatures are also marked in Figure 6.9, which shows the state of charge over time. Furthermore, the temperature fields on the symmetry plane of the packed-bed, as illustrated in Figure 4.8, resulting from the three-dimensional CFD simulation are shown in Figure 6.10 at the same points of time.

The temperature fields on the symmetry plane clearly show a vertical profile in the packed bed at  $t_2 = 540$  h and  $t_3 = 1340$  h, which is caused by natural convection. The vertical temperature profile mainly develops at hold operation. The Rayleigh number according to Equation 2.56 for example at  $t_3$  is  $Ra = 463$ . According to the CFD simulation results, such a temperature profile is



a / Mean temperature along main flow direction for  $t_1 = 8$  h,  $t_2 = 540$  h,  $t_3 = 1340$  h and  $t_4 = 1405$  h.

b / Pressure drop at 524 to 546 h.

**Figure 6.8 /** Comparison of simulation results for the mean temperature along the main flow direction and the pressure drop of the one- and three-dimensional model for a 30 MW unit at a power-to-power operation and the wholesale electricity price based operational schedule.

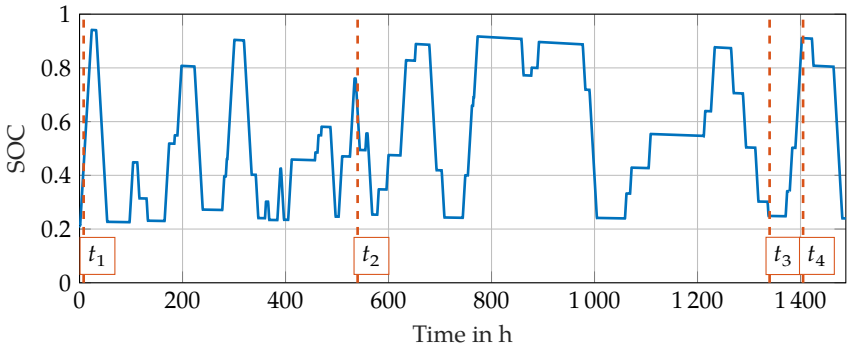


**Figure 6.9 /** State of charge over time at the comparison of the one- and three-dimensional models.

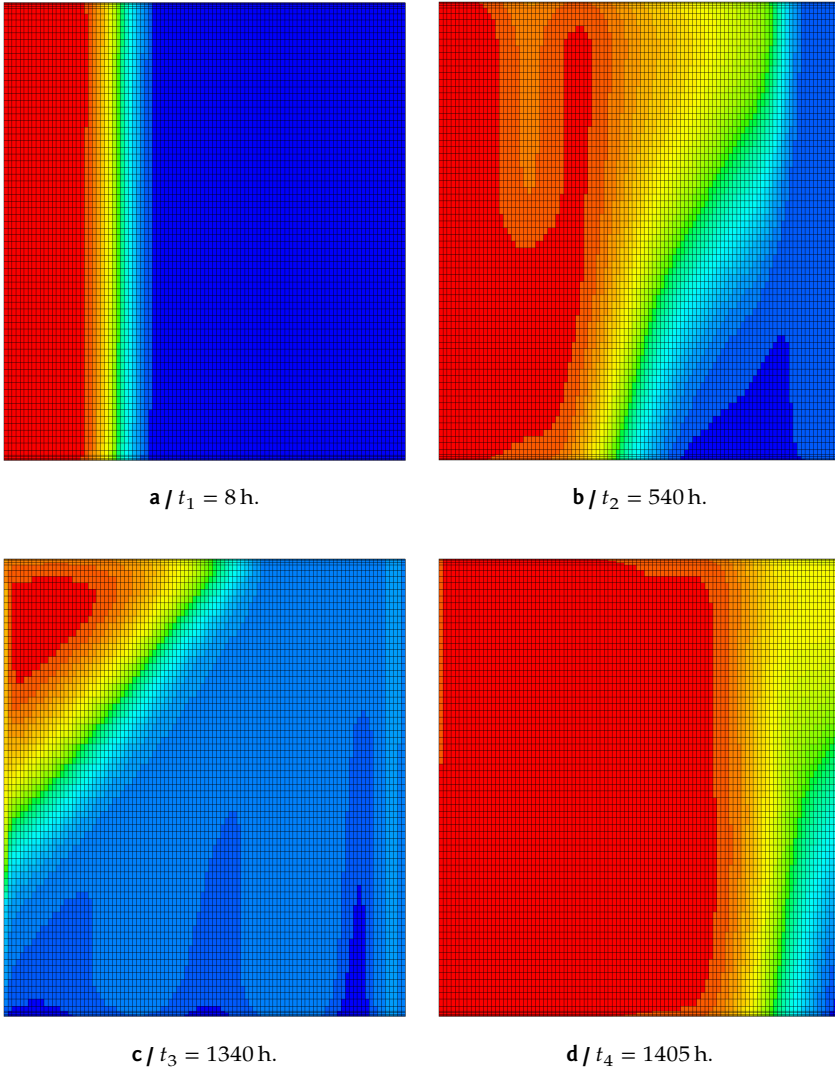


**Figure 6.10** / Temperature field on the symmetry plane (see Figure 4.8) determined by porous-media CFD simulation for a rectangular horizontal-flow packed-bed storage unit at four different points of time. Flow at charge is from left to right, the temperature ranges from 20 °C (blue) to 750 °C (red) .

sustained or even further strengthened at discharge operations, which leads to a reduced depth of discharge, as also encountered by Soprani et al. [166]. The storage outlet temperature at  $t_3 = 1340$  h according to the three-dimensional model is for example approximately  $\vartheta_{\text{out}} = 430$  °C, whereas it is  $\vartheta_{\text{out}} = 530$  °C in the one-dimensional model.

But, after the subsequent charge operation at  $t_4 = 1405$  h, the vertical temperature profile has leveled. Accordingly, the mean absolute error of the one-dimensional model with respect to the three-dimensional model reduces from 37 °C to 6.1 °C. Reasons for the temperature profile leveling are,

- a larger mass flow in cold packed-bed sections at the same pressure gradient due to the increased air density and more importantly
- a removal of the thermocline region from the packed bed according to the outlet temperature deviation tolerance.

At  $t_2 = 540$  h on the other hand, the vertical temperature profile is still present, as it has not been diminished as much in the preceding charge operation, which was stopped before the thermocline had reached the packed-bed outlet.

A small difference between both models with respect to the pressure loss across the packed bed is encountered for the tested rectangular design. The mean absolute error is at 0.65 mbar in the time period of 524 to 546 h including a charge and discharge operation.

Besides the non-uniform flow, the three-dimensional model also accounts for temperature gradients inside the packed-bed towards the walls, which result from wall heat losses. As the one-dimensional model can not account for these, it tends to over-predict the heat losses. Nevertheless, no significant effect is shown for the tested packed bed with a volume of 2700 m<sup>3</sup>. One reason is, that the good thermal insulation of the packed-bed storage leads to a limited influence of the temperature gradient inside the packed bed on the overall heat transfer, even though is apparent in Figure 6.10. The temperature gradient inside the packed bed may become increasingly relevant for smaller packed-bed storage units or even longer hold operations.

Due to the periodic temperature profile leveling, the mean temperature along the main flow direction in the one-dimensional model does not deviate sig-

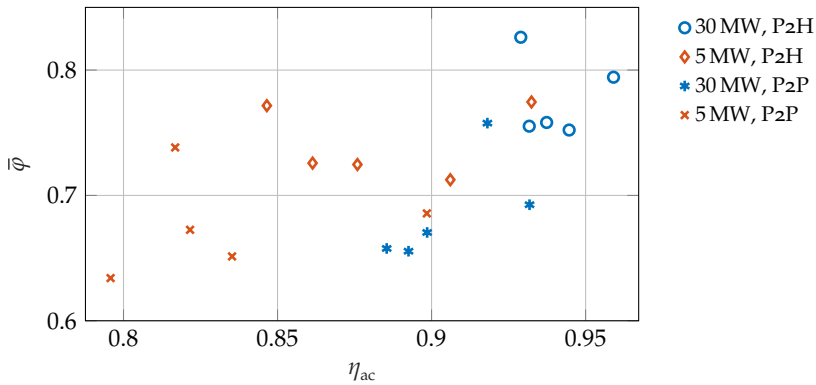


**Figure 6.11 /** Energy-based air cycle efficiency  $\eta_{ac}$  and mean usable capacity ratio  $\bar{\varphi}$  for all test cases in the observation time period.

nificantly from the three-dimensional model for this storage design and operating conditions over the simulation time of two months. According to the comparison results, the one-dimensional model is applicable to the tested horizontal-flow packed-bed TES unit and operational schedule even though the outlet temperature and thus also depth of discharge are over-predicted intermediately. Comparison results are similar for the other test cases. However, further designs and operating conditions may lead to different results. Larger particles for example increase the natural convection at hold due to the lower packed-bed permeability. Smaller storage unit aspect ratios lead to lower air velocities at charge and thus reduce the described effect of temperature profile leveling, similar to lower outlet temperate deviation tolerances.

## 6.7 Comparison of Air Cycle Performance for the Test Cases

Finally, the ETES air cycle efficiency and packed-bed storage mean usable capacity ratio can be compared for all test cases in this section. The respective simulation results are shown in Figure 6.11. The air cycle efficiency ranges from 78 to 96 % and the mean usable capacity ratio from 63 to 83 % for all 20 test cases.

P2H operation leads to higher efficiencies in comparison to P2P at all operational schedules due to the increased energy turnover and irrelevance of technical fan work demand on the overall efficiency. Furthermore, the packed-bed usable capacity ratio is generally higher according to

- the lower HRSG air outlet temperature, which results from the lower live steam temperature and pressure requirements, and
- the storage unit design with increased aspect ratio, which is reasoned by the irrelevance of technical fan work demand at power-to-heat operation.

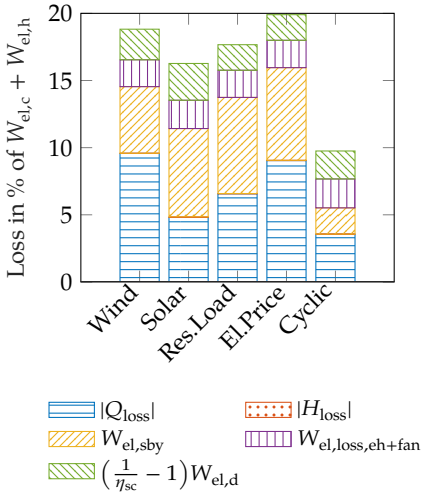
The larger 30 MW units show an improved efficiency and at least similar usable capacity ratio compared to the 5 MW units at all operational schedules.

The contribution of each energy loss mechanism according to Section 3.7 for all test cases is shown in Figure 6.12 in order to further analyze the reasons for the efficiency variation among the test cases.

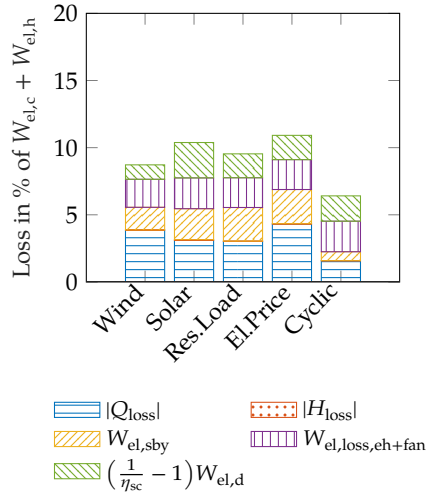
The five operational schedules used in this work are listed in the following, printing the short notation used in Figure 6.12 as bold letters. The schedules are based on

1. a characteristic cyclic **wind**-based operation,
2. the *California Duck Curve* as characteristic cyclic **solar**-based operation,
3. **residual load** time series data,
4. wholesale **electricity price** time series data and
5. **cyclic** full charge and discharge operation without hold.

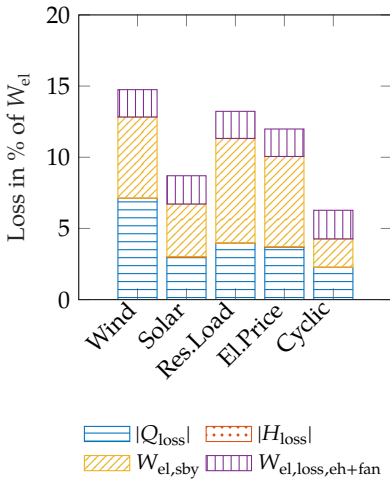
The relevance of the overall air cycle transmission heat losses  $Q_{\text{loss}}$  mainly depends on the unit size and operational schedule, especially due to the varying energy turnover per observation time period. The electricity price and residual load based operational schedules show the highest share of hold operation, which is around 75 % of the observation time. The cycle composed of subsequent full charge and discharge operations on the other hand does not include any hold operation. Accordingly, the number of equivalent full cycles, which quantifies the energy turnover is at 12.5/month for the cyclic operation, whereas it is at 3.6/month for the electricity price based schedule. Furthermore, the installed thermal storage capacity is relevant, as the state of charge at each hold operation, because a higher temperature inside the packed



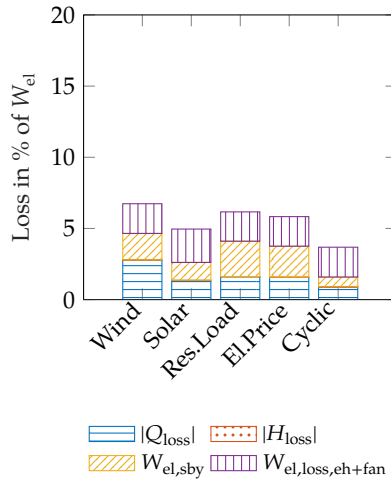
a / 5 MW unit in power-to-power operation.



b / 30 MW unit in power-to-power operation.



c / 5 MW unit in power-to-heat operation.



d / 30 MW unit in power-to-heat operation.

**Figure 6.12** / Energy loss contributions for all test cases according to Section 3.7 in relation to the electric energy intake, which has to be differentiated according to charge, discharge and hold mode in the case of power-to-power operation.

bed at hold significantly increase the transmission heat losses.

The relative share of the storage unit heat loss with respect to the overall air cycle heat loss also varies among the different operational schedules and unit sizes. Whereas it is 81 % for the 5 MW unit and wind-based operational schedule, it can be as low as 16 % for the 30 MW unit and solar-based operational schedule. Accordingly, the thermal insulation of the piping is increasingly relevant at a high frequency of operation and large thermal storage capacities. Furthermore, the heat capacity of the pipes should be low in order to store less thermal energy during charge and discharge operation and thereby reduce heat losses at hold.

The transmission heat losses are significantly lower for the larger unit size of 30 MW in comparison to the 5 MW unit at the same insulation thickness due to the improved relation of storage volume to surface area. Even for the irregular operational schedules, the transmission heat losses remain below 10 and 5 % of the electric energy intake respectively.

The self-discharge rate relates the transmission heat losses to the observation time and storage capacity. It is defined according to Equation 2.8 with the overall heat losses of the air cycle as

$$\text{SDR} = \frac{|Q_{\text{loss}}|}{\Delta t \Delta E_{\text{nom}}^s}. \quad [6.2]$$

According to the simulation results, it varies from 0.29 %/day in the case of the 30 MW unit at wind-based power-to-power operation to 4.7 %/day in the case of the 5 MW unit at solar-based power-to-power operation for the chosen insulation thickness.

As the air vent, which is necessary to maintain the pressure level inside the air cycle, is positioned upfront of the fan and thus at a low temperature level, the ventilation loss  $|H_{\text{loss}}|$  is generally at least one magnitude below the transmission heat loss, and included here for the sake of completeness. No air leakage is taken into account.

The contribution of standby losses  $W_{\text{el,sby}}$  is subject to uncertainty, as it is based

on the assumption of a constant auxiliary electric power demand of 50 and 100 kW for the 5 and 30 MW units respectively. Nevertheless, this standby power for example accounts for 51 % of the overall energy losses at power-to-heat operation with the 5 MW unit and the residual-load based schedule according to the low number of equivalent full cycles of 5.5/month. Thus, standby losses can be critical and should be given attention at the storage system design process.

The conversion losses of the electric heater and fan  $W_{el,loss,eh+fan}$  such as transformer and electric motor losses are modeled proportional to the power intake. Thus, they are at 2.1 to 2.3 % for each unit size and operational schedule, varying only with the packed-bed pressure loss and thus respective fan energy demand.

The necessity to generate the electric work demand of the air cycle at discharge from the water-steam cycle and the related conversion loss in the water-steam cycle  $(\frac{1}{\eta_{sc}} - 1)W_{el,d}$  is one reason for the lower air cycle efficiency at power-to-power in comparison to power-to-heat operation. A water-steam cycle efficiency of 0.45 is assumed here. The loss is at 2 to 3.5 % for all test cases, but it can be significantly higher for different particle sizes and storage unit aspect ratios, as shown in Section 6.3. The electric work demand of the air cycle at discharge is mainly due to fan work, which is associated with the packed-bed pressure loss. The pressure loss strongly depends on the air velocity inside the packed bed. Due to the short discharge operation and thus high rate of discharge, the solar-based operational schedule shows the highest contribution of the energy loss according to electric work demand at discharge on the overall energy loss.



# Chapter 7

## Conclusion

The ETES concept is a build-anywhere large-scale energy storage technology, which is suitable to balance VRE generation with both electricity and heat demands. According to its technology readiness and cost-effectiveness, the ETES concept can make a valuable contribution to the fast reduction of CO<sub>2</sub>-emissions and fossil-fuel dependency by supporting the increase of the VRE share on the electricity and heat demand.

The ETES system can be subdivided in an

- air cycle including a packed-bed TES, electric heater and HRSG which can provide steam upon demand for various purpose, and a
- conventional water-steam cycle to optionally generate electricity from the steam by means of a turbine and thus complement an EES system.

The analysis of the storage concept in this thesis includes three modeling scales, which are system simulation, CFD simulation of the packed-bed storage and particle-resolved CFD simulation. The simultaneous numerical investigation on different scales facilitates a more-physical modeling, as the dependency on empirical correlations is reduced and it increases the insight, as the interactions of the parameters on the micro and macro scale can be revealed.

## Summary of Simulation Results

According to the simulation results for 20 different test cases shown in this work, the energy-based air cycle efficiency is at 78 to 96 %, depending on the way of energy system integration, operational schedule and unit size. In the case of an EES application, this air cycle efficiency has to be multiplied to the water-steam cycle efficiency to obtain the round-trip efficiency. Typical water-steam cycle efficiencies for modern steam power plants are at 35 to 47 % [167]. Heat loss to the environment is the most significant energy loss mechanism for an ETES air cycle unit at most tested designs and operational conditions. The heat loss of the packed-bed storage remains at hold operation and therefore leads to permanent self-discharge, but can be diminished by thermal insulation up to a limit defined by economic design optimization. Further energy loss mechanism of the ETES air cycle are the conversion losses in the water-steam cycle associated with the electric work demand of the air cycle at discharge in the case of power-to-power operation, leakage or venting of air, conversion losses in the electric heater and fan such as transformer and electric motor losses and the standby electricity demand. Notably, the simulated schedules regard irregular storage operation as relevant to VRE and load balancing with relative shares of hold operation on the overall observation time up to 75 %.

The nominal volumetric thermal storage capacity for a packed bed of basalt heated up to 750 °C is at 0.33 MWh<sub>th</sub>/m<sup>3</sup>, using a reference temperature of 20 °C and the material properties of Nahhas et al. [132]. But the usable storage capacity is lower due to the thermal destratification in combination with the operational limits on the packed-bed in- and outlet temperature at charge and discharge. For the tested designs and operational schedules a usable capacity ratio of 63 to 83 % has been determined by simulation in this work, which is high compared to values reported by other authors [33, 125, 140, 164, 198]. Reason is that packed beds have been often analyzed with the background of open air cycles, for which the air enthalpy leaving the storage at charge is lost and thus the outlet temperature deviation tolerance must be significantly lower compared to the closed ETES system. The packed bed can be oversized to compensate the limited depth of charge and discharge, which leads to additional heat loss and fan work in return.

The optimal storage unit aspect ratio generally decreases with the packed-bed volume, in order to limit the fan energy demand. Nevertheless, the contrary

effects of the packed-bed aspect ratio and particle size on the ETES air cycle efficiency and packed-bed usable capacity ratio lead to the necessity for an application case specific design optimization.

A horizontal-flow design for packed-bed TES allows to build large-scale units at a lower construction cost compared to the more common vertical-flow design. Even though natural convection at hold operation reduces the depth of discharge, the temperature profile levels at charge operations with sufficient air velocity for the tested designs according to CFD simulation results. Consequently, the reduction of usable capacity is limited and can be accepted. Particle-resolved CFD simulations indicate a 5 to 20 % reduction of the pressure gradient for horizontal-flow packed beds in comparison to vertical-flow beds. Reason is the evenly arrangement of the tested non-spherical particle shapes at the packing process, which is consistent with the experimental results of Allen et al. [6]. The difference in effective thermal conductivity at stagnant fluid in horizontal and vertical direction has been found to be 3 % at most.

### **Comparison to other Electric Energy Storage Technologies**

The ETES round trip efficiency, when applied as EES, is only approximately half the value of pumped hydro or lithium-ion battery efficiencies and in the same range as EES by electrolysis and oxidation of hydrogen. But the overall energy utilization can be significantly increased if a concurrent heat demand can be fulfilled at discharge by cogeneration of heat and power. This is not equally the case for hydrogen energy storage due to the electrolysis efficiency at charge. On the other hand, the self-discharge rate of hydrogen energy storage is lower and it is thus more suitable for long hold operations as necessary for seasonal energy storage or strategic energy reserve.

The ETES power-to-power round-trip efficiency is also low in comparison to other Carnot Battery concepts, as the efficiency is limited by the discharge cycle according to the utilization of an electric heater for charge instead of a heat pump. On the other hand, the high storage temperature allows the utilization of conventional water-steam cycles for discharge and leads to a high volumetric energy storage density. Furthermore, the ETES level of technology readiness is higher than that of many other Carnot Battery concepts due to the utilization of conventional process equipment for charge and discharge.

Significant advantage on pumped hydro energy storage is the independency of the ETES concept on geographical prerequisites. Furthermore, the energy density is significantly higher, leading to less land-use. In contrast to lithium-ion batteries, ETES is not subject to resource limitations on the storage material. The nominal charge and discharge power as well as the storage capacity of ETES units can be scaled independently, as the charge and discharge processes use components which are separate from the storage unit, namely the electric heater and HRSG. The scaling of these components can thus be done according to the application case requirements, such as wind and solar energy or load characteristics, which further reduces the capital cost.

Due to the usage of crushed rock as storage material and commercially available components for the charge and discharge processes, the ETES technology is cost-competitive compared to other EES technologies [160, 161]. Walter et al. [186] estimate the system cost for a 100 MW ETES unit at 40 % of the cost for a corresponding PTES system. In combination with the self-discharge loss, the ETES concept is thus assumed to be especially suitable for balancing of VRE electricity generation and demand at a nominal charge and discharge duration in the range of several hours to several days, as

- the relevance of capital cost with respect to efficiency increases at low numbers of equivalent full cycles per year,
- the relevance of capital cost per storage capacity increases at high energy to power ratios and
- the relevance of self-discharge increases at longer hold operations.

### **Power-to-Heat Operation and Power Plant Integration**

Besides the application as EES in combination with a water-steam cycle, the ETES concept can be also used to provide low-carbon heat from VRE upon demand. The resistivity of the packed-bed TES at least up to temperatures of 750 °C, as shown with the demonstration plant, facilitates the provision of industrial process heat. In Germany, the industrial process heat demand at 100 to 500 °C, which is beyond the applicability of conventional hot water storage, has been 5.4 % of the overall final energy demand in 2015 [76].

Live steam temperatures of existing coal-fired power plants in Germany are

generally below 650 °C [167]. Thus, these plants can be supplied with steam from an ETES air cycle according to the high storage temperature, which still leaves an operational margin in order to allow a storage outlet temperature deviation tolerance at discharge.

As stack losses, which lead to efficiencies of 94 to 95 % for modern hard coal-fired boilers according to Rackley [148] or 88 to 92 % for coal-fired boilers according to Vakkilainen [180], as well as fuel preparation and exhaust gas treatment are omitted, it is expected, that the overall efficiency of power plants is not significantly decreased, if supplied with steam from an ETES unit instead of a coal-fired boiler.

At a nominal gravimetric thermal storage capacity of 0.15 kWh<sub>th</sub>/kg for a packed bed of basalt at a temperature spread of 500 °C, a packed-bed usable capacity ratio of 70 % and a net calorific value for hard coal of 24 MJ/kg, a storage material mass, which is equivalent to the mass of a hard-coal storage for 30 days, would allow a power plant operation at nominal load purely from the thermal storage for approximately 11 hours. An ETES integration in existing power plants can be especially worthwhile if the power plant otherwise faces regulatory phase-out.

## Outlook

At the current stage, natural convection is not taken into account in the one-dimensional packed-bed model directly, but retroactively accounted for by result comparison with the three-dimensional CFD packed-bed model. Future work should investigate ways to integrate natural convection modeling into system simulation for horizontal-flow packed-bed TES, taking into account charge, hold and discharge operation.

In order to further analyze the potentialities and limitations of the ETES concept, a pilot plant with a rate of charge and discharge of 30 MW as well as a thermal storage capacity of 1 GWh<sub>th</sub> should be experimentally tested. Based on the simulation results of this work, it is expected to show an improved performance in comparison to the existing demonstration plant.



# Bibliography

- [1] A. Abdon, X. Zhang, D. Parra, M. K. Patel, C. Bauer, and J. Worlitschek. "Techno-economic and environmental assessment of stationary electricity storage technologies for different time scales." In: *Energy* 139 (2017), pages 1173–1187.
- [2] E. Achenbach. "Heat and flow characteristics of packed beds." In: *Experimental Thermal and Fluid Science* 10.1 (1995), pages 17–27.
- [3] G. Airò Farulla, M. Cellura, F. Guarino, and M. Ferraro. "A Review of Thermochemical Energy Storage Systems for Power Grid Support." In: *Applied Sciences* 10.9 (2020), page 3142.
- [4] B. Alazmi and K. Vafai. "Analysis of Variants Within the Porous Media Transport Models." In: *Journal of Heat Transfer* 122.2 (2000), page 303.
- [5] K. G. Allen, T. von Backström, E. Joubert, and P. Gauché. "Rock bed thermal storage: Concepts and costs." In: *American Institute of Physics Conference Proceedings* 1734 (2016).
- [6] K. G. Allen, T. W. von Backström, and D. G. Kröger. "Packed bed pressure drop dependence on particle shape, size distribution, packing arrangement and roughness." In: *Powder Technology* 246 (2013), pages 590–600.
- [7] K. G. Allen, T. W. von Backström, and D. G. Kröger. "Packed Rock Bed Thermal Storage in Power Plants: Design Considerations." In: *Energy Procedia* 49 (2014), pages 666–675.
- [8] K. G. Allen, T. W. von Backström, and D. G. Kröger. "Rock bed pressure drop and heat transfer: Simple design correlations." In: *Solar Energy* 115 (2015), pages 525–536.

- [9] K. G. Allen, T. W. von Backström, D. G. Kröger, and A.F.M. Kisters. "Rock bed storage for solar thermal power plants: Rock characteristics, suitability, and availability." In: *Solar Energy Materials and Solar Cells* 126 (2014), pages 170–183.
- [10] R. Anderson, L. Bates, E. Johnson, and J. F. Morris. "Packed bed thermal energy storage: A simplified experimentally validated model." In: *Journal of Energy Storage* 4 (2015), pages 14–23.
- [11] L. Andresen, P. Dubucq, R. Peniche Garcia, G. Ackermann, A. Kather, and G. Schmitz. "Status of the TransiEnt Library: Transient Simulation of Coupled Energy Networks with High Share of Renewable Energy." In: *Proceedings of the 11th International Modelica Conference* (2015), pages 695–705.
- [12] Association of German Engineers. *Economic efficiency of building installations*. 2012.
- [13] Association of German Engineers, editor. *VDI Heat Atlas*. 11th edition. Berlin Heidelberg: Springer-Verlag, 2006.
- [14] M. M.S. Al-Azawii, C. Theade, P. Bueno, and R. Anderson. "Experimental study of layered thermal energy storage in an air-alumina packed bed using axial pipe injections." In: *Applied Energy* 249 (2019), pages 409–422.
- [15] H. Bai, J. Theuerkauf, and Gillis, P. A. and Witt, P. M. "A Coupled DEM and CFD Simulation of Flow Field and Pressure Drop in Fixed Bed Reactor with Randomly Packed Catalyst Particles." In: *Industrial and Engineering Chemistry Research* (2009).
- [16] N. G. Barton. "Simulations of air-blown thermal storage in a rock bed." In: *Applied Thermal Engineering* 55.1-2 (2013), pages 43–50.
- [17] R. Bauer. "Effektive radiale Wärmeleitfähigkeit gasdurchströmter Schüttungen aus Partikeln unterschiedlicher Form und Größenverteilung." In: *VDI-Forschungsheft* 582 (1977).
- [18] T. Bauer, W.-D. Steinmann, D. Laing, and R. Tammé. "Thermal Energy Storage Material and Systems." In: *Annual Review of Heat Transfer* 15.1 (2012), pages 131–177.

- [19] R. Bayón, E. Rivas, and E. Rojas. "Study of Thermocline Tank Performance in Dynamic Processes and Stand-by Periods with an Analytical Function." In: *Energy Procedia* 49 (2014), pages 725–734.
- [20] V. Becattini, T. Motmans, A. Zappone, C. Madonna, A. Haselbacher, and A. Steinfeld. "Experimental investigation of the thermal and mechanical stability of rocks for high-temperature thermal-energy storage." In: *Applied Energy* 203 (2017), pages 373–389.
- [21] J. Beek. "Desing of packed catalytic reactors." In: *Advanced Chemical Engineering* 3 (1962), pages 203–271.
- [22] A. Bejan. "Lateral Intrusion of Natural Convection into a Horizontal Porous Structure." In: *Journal of Heat Transfer* 103 (1981), pages 237–241.
- [23] A. Bejan and C. L. Tien. "Natural Convection in a Horizontal Porous Medium Subjected to an End-To-End Temperature Difference." In: *Journal of Heat Transfer* 100 (1978), pages 191–200.
- [24] H. Bindra, P. Bueno, and J. F. Morris. "Sliding flow method for exergetically efficient packed bed thermal storage." In: *Applied Thermal Engineering* 64.1-2 (2014), pages 201–208.
- [25] M. B. Blarke. "Towards an intermittency-friendly energy system: Comparing electric boilers and heat pumps in distributed cogeneration." In: *Applied Energy* 91.1 (2012), pages 349–365.
- [26] B. Bouvry et al. "Mediterranean basin basalts as potential materials for thermal energy storage in concentrated solar plants." In: *Solar Energy Materials and Solar Cells* 171 (2017), pages 50–59.
- [27] H. Brauer. *Grundlagen der Einphasen- und Mehrphasenströmungen*. Grundlagen der chemischen Technik. Aarau: Sauerländer, 1971.
- [28] P. Breeze. "Hydrogen Energy Storage." In: *Power System Energy Storage Technologies*. Edited by P. Breeze. San Diego: Elsevier Science & Technology, 2018, pages 69–77.
- [29] A. Bruch, S. Molina, T. Esence, J. F. Fourmigué, and R. Couturier. "Experimental investigation of cycling behaviour of pilot-scale thermal oil packed-bed thermal storage system." In: *Renewable Energy* 103 (2017), pages 277–285.

- [30] N. F. Cabello, J. López Sanz, and F. Zaversky. "Analysis of steel making slag pebbles as filler material for thermocline tanks in a hybrid thermal energy storage system." In: *Solar Energy* 188 (2019), pages 1221–1231.
- [31] California Independent System Operator. *Flexible Resources help Renewables Fast Facts*. URL: [http://www.caiso.com/Documents/Flexibleresourceshelprenewables\\_FastFacts.pdf](http://www.caiso.com/Documents/Flexibleresourceshelprenewables_FastFacts.pdf).
- [32] California Independent System Operator. *Homepage*. 2020. URL: <http://www.caiso.com/>.
- [33] B. Cárdenas, T. R. Davenne, J. P. Rouse, and S. D. Garvey. "Effect of design parameters on the exergy efficiency of a utility-scale packed bed." In: *Journal of Energy Storage* 18 (2018), pages 267–284.
- [34] M. Cascetta, F. Serra, G. Cau, and P. Puddu. "Comparison between experimental and numerical results of a packed-bed thermal energy storage system in continuous operation." In: *Energy Procedia* 148 (2018), pages 234–241.
- [35] H. Chen, X. Zhang, J. Liu, and T. Chunqing. "Compressed Air Energy Storage." In: *Energy Storage - Technologies and Applications* (2013).
- [36] T. Chen, Y. Jin, H. Lv, A. Yang, M. Liu, B. Chen, Y. Xie, and Q. Chen. "Applications of Lithium-Ion Batteries in Grid-Scale Energy Storage Systems." In: *Transactions of Tianjin University* 26.3 (2020), pages 208–217.
- [37] C. J. Coetzee. "Calibration of the discrete element method and the effect of particle shape." In: *Powder Technology* (2016).
- [38] C. J. Coetzee and R. G. Nel. "Calibration of discrete element properties and the modelling of packed rock beds." In: *Powder Technology* 264 (2014), pages 332–342.
- [39] U.M.S. Costa, J. S. Andrade Jr., H. A. Makse, and H. E. Stanley. "The role of inertia on fluid flow through disordered porous media." In: *Physica A* 266 (1999).
- [40] J. P. Coutier and E. A. Farber. "Two Applications of a numerical approach of heat transfer process within rock beds." In: *Solar Energy* 29 (1982), pages 451–462.

- [41] F. L. Curzon and B. Ahlborn. "Efficiency of a Carnot engine at maximum power output." In: *American Journal of Physics* 43.1 (1975), pages 22–24.
- [42] H. Darcy. "Les fontaines publiques de la ville de Dijon." In: (1856).
- [43] C. K. Das, O. Bass, G. Kothapalli, T. S. Mahmoud, and D. Habibi. "Overview of energy storage systems in distribution networks: Placement, sizing, operation, and power quality." In: *Renewable and Sustainable Energy Reviews* 91 (2018), pages 1205–1230.
- [44] Dassault Systemes. *Dymola*. URL: <https://www.3ds.com/de/produkte-und-services/catia/produkte/dymola/>.
- [45] 1414 Degrees. *Homepage*. 2020. URL: [1414degrees.com.au](http://1414degrees.com.au).
- [46] P. Denholm and M. Hand. "Grid flexibility and storage required to achieve very high penetration of variable renewable electricity." In: *Energy Policy* 39.3 (2011), pages 1817–1830.
- [47] T. Desrues, J. Ruer, P. Marty, and J. F. Fourmigué. "A thermal energy storage process for large scale electric applications." In: *Applied Thermal Engineering* 30.5 (2010), pages 425–432.
- [48] A. G. Dixon and S. A. Logtenberg. "Computational fluid dynamics studies of fixed bed heat transfer." In: *Chemical Engineering and Processing: Process Intensification* 37.1 (1997), pages 7–21.
- [49] A. G. Dixon, M. Nijemeisland, and E. H. Stitt. "Systematic mesh development for 3D CFD simulation of fixed beds: Contact points study." In: *Computers & Chemical Engineering* 48 (2013), pages 135–153.
- [50] DLR and Dynasim AB. *Modelica State Graph 2 Repository*. 2020. URL: [https://github.com/modelica-3rdparty/Modelica\\_StateGraph2](https://github.com/modelica-3rdparty/Modelica_StateGraph2).
- [51] V. Dreißigacker. "Direkt durchströmte Feststoffwärmespeicher: thermomechanische Untersuchungen von Schüttungen für die großtechnische Speicherung von Hochtemperaturwärme." Dissertation. Stuttgart, 2013.
- [52] V. Dreißigacker, H. Müller-Steinhagen, and S. Zunft. "Thermo-mechanical analysis of packed beds for large-scale storage of high temperature heat." In: *Heat and Mass Transfer* 46.10 (2010), pages 1199–1207.

- [53] O. Dumont, G. F. Frate, A. Pillai, S. Lecompte, M. de paepe, and V. Lemort. "Carnot battery technology: A state-of-the-art review." In: *Journal of Energy Storage* 32 (2020), page 101756.
- [54] B. Eppinger, D. Steger, C. Regensburger, J. Karl, E. Schlücker, and S. Will. "Carnot battery: Simulation and design of a reversible heat pump-organic Rankine cycle pilot plant." In: *Applied Energy* 288 (2021), page 116650.
- [55] T. Eppinger, N. Jurtz, and R. Aglave. "Automated workflow for spatially resolved packed bed reactors with spherical and non-spherical particles." In: *Proceedings of 10th International Conference on CFD in Oil & Gas, Metallurgical and Process Industries* (2014).
- [56] T. Eppinger, K. Seidler, and M. Kraume. "DEM-CFD simulations of fixed bed reactors with small tube to particle diameter ratios." In: *Chemical Engineering Journal* 166.1 (2011), pages 324–331.
- [57] S. Ergun. "Fluid Flow Through Packed Columns." In: *Chemical Engineering Progress* 48 (1952), pages 89–94.
- [58] V. L. Eriksen, editor. *Heat recovery steam generator technology*. Duxford, United Kingdom: Woodhead Publishing, 2017.
- [59] T. Esence, A. Bruch, S. Molina, B. Stutz, and J.-F. Fourmigu. "A review on experience feedback and numerical modeling of packed-bed thermal energy storage systems." In: *Solar Energy* 153 (2017), pages 628–654.
- [60] S. E. Faas and Thorne, L.R., Fuch, E.A., Gilbertsen, N. D. *10 MWe Solar Thermal Central Receiver Pilot Plant - Thermal storage subsystem evaluation - Final Report*. Edited by Sandia National Laboratories. 1986.
- [61] T. Fasquelle, Q. Falcoz, P. Neveu, and J.-F. Hoffmann. "A temperature threshold evaluation for thermocline energy storage in concentrated solar power plants." In: *Applied Energy* 212 (2018), pages 1153–1164.
- [62] J. Figgenger, P. Stenzel, K.-P. Kairies, J. Linßen, D. Haberschusz, O. Wessels, G. Angenendt, M. Robinius, D. Stolten, and D. U. Sauer. "The development of stationary battery storage systems in Germany – A market review." In: *Journal of Energy Storage* 29 (2020), page 101153.

- [63] Fraunhofer Institut für Solare Energiesysteme ISE. *Studie: Wege zu einem klimaneutralen Energiesystem - Die deutsche Energiewende im Kontext gesellschaftlicher Verhaltensweisen*. 2020.
- [64] V. Ganapathy. *Waste heat boiler deskbook*. Lilburn, GA: Fairmont Press, 1991.
- [65] J. Gasia, L. Miró, and L. F. Cabeza. "Review on system and materials requirements for high temperature thermal energy storage. Part 1: General requirements." In: *Renewable and Sustainable Energy Reviews* 75 (2017), pages 1320–1338.
- [66] German Federal Network Agency. *Electricity Market Data*. 2020. URL: <https://www.smard.de>.
- [67] M. Giese. "Strömung in porösen Medien und Berücksichtigung effektiver Viskositäten." Dissertation. München: Technische Universität München, 1998.
- [68] A. Gil, M. Medrano, I. Martorell, A. Lázaro, P. Dolado, B. Zalba, and L. F. Cabeza. "State of the art on high temperature thermal energy storage for power generation. Part 1—Concepts, materials and modellization." In: *Renewable and Sustainable Energy Reviews* 14.1 (2010), pages 31–55.
- [69] V. Gnielinski. "Wärme- und Stoffübertragung in Festbetten." In: *Chemie Ingenieur Technik* 52.3 (1980), pages 228–236.
- [70] M. Y. Haller, C. A. Cruickshank, W. Streicher, S. J. Harrison, E. Andersen, and S. Furbo. "Methods to determine stratification efficiency of thermal energy storage processes – Review and theoretical comparison." In: *Solar Energy* 83.10 (2009), pages 1847–1860.
- [71] Hamburg University of Technology. *TransiEnt Library*. 2020. URL: <https://www.tuhh.de/transient-ee/en/>.
- [72] Hamburg University of Technology, XRG Simulation GmbH, and TLK Thermo GmbH. *ClaRa Library*. 2020. URL: <https://www.claralib.com/index.php>.
- [73] Hamburg University of Technology, XRG Simulation GmbH, and TLK Thermo GmbH. *ClaRa Library Documentation*. 2020.

- [74] M. Hänchen, S. Brückner, and A. Steinfeld. “High-temperature thermal storage using a packed bed of rocks – Heat transfer analysis and experimental validation.” In: *Applied Thermal Engineering* 31.10 (2011), pages 1798–1806.
- [75] P. Hartlieb, M. Toifl, F. Kuchar, R. Meisels, and T. Antretter. “Thermo-physical properties of selected hard rocks and their relation to microwave-assisted comminution.” In: *Minerals Engineering* 91 (2016), pages 34–41.
- [76] Heat Roadmap Europe. *2015 Final Heating & Cooling Demand in Germany*. 2017. URL: [https://heatroadmap.eu/wp-content/uploads/2018/11/HRE4-Country\\_presentation-Germany.pdf](https://heatroadmap.eu/wp-content/uploads/2018/11/HRE4-Country_presentation-Germany.pdf).
- [77] H. Herwig, Y. Jin, and M.F. Uth. “Turbulent flow in the micro structure of porous media.” In: *Proceedings of the 13th International Conference on Nanochannels, Microchannels, and Minichannels* (2015).
- [78] H. Hesse, M. Schimpe, D. Kucevic, and A. Jossen. “Lithium-Ion Battery Storage for the Grid—A Review of Stationary Battery Storage System Design Tailored for Applications in Modern Power Grids.” In: *Energies* 10.12 (2017), page 2107.
- [79] Highview Power. *Homepage*. 17.07.2020. URL: <https://highviewpower.com/>.
- [80] N. Hoivik, C. Greiner, J. Barragan, A. C. Iniesta, G. Skeie, P. Bergan, P. Blanco-Rodriguez, and N. Calvet. “Long-term performance results of concrete-based modular thermal energy storage system.” In: *Journal of Energy Storage* 24 (2019), page 100735.
- [81] J. Howes. “Concept and Development of a Pumped Heat Electricity Storage Device.” In: *Proceedings of the Institute of Electrical and Electronics Engineers* 100.2 (2012), pages 493–503.
- [82] M. Hradisky and P.J. Smith. *Development of CFD-Based Simulation Tools for in Situ Thermal Processing of Oil Shale/Sands*. 2012.
- [83] H. Ibrahim, A. Ilinca, and J. Perron. “Energy storage systems—Characteristics and comparisons.” In: *Renewable and Sustainable Energy Reviews* 12.5 (2008), pages 1221–1250.

- [84] A. Immendoerfer, I. Tietze, H. Hottenroth, and T. Viere. "Life-cycle impacts of pumped hydropower storage and battery storage." In: *International Journal of Energy and Environmental Engineering* 8.3 (2017), pages 231–245.
- [85] International Energy Agency. *Technology Collaboration Programme Task 36: Carnot Batteries*. 16.03.2021. URL: <https://www.eces-a36.org/>.
- [86] International Energy Agency. *Tracking Clean Energy Progress*. 3.12.2020. URL: <https://www.iea.org/reports/energy-storage>.
- [87] International Renewable Energy Agency. *Electricity storage and renewables: Costs and markets to 2030*. Edited by International Renewable Energy Agency. Abu Dhabi, 2017.
- [88] International Renewable Energy Agency. *Innovation Landscape Brief: Utility-Scale Batteries*. Abu Dhabi, 2019.
- [89] International Renewable Energy Agency. *Renewable Energy Capacity Statistics*. 2021. URL: <https://www.irena.org/publications/2021/March/Renewable-Capacity-Statistics-2021>.
- [90] K.A.R. Ismail and R. Stuginsky Jr. "A parametric study on possible fixed bed models for pcm and sensible heat storage." In: *Applied Thermal Engineering* 19.7 (1999), pages 757–788.
- [91] A. Jafari, P. Zamankhan, S. M. Mousavi, and K. Pietarinen. "Modeling and CFD simulation of flow behavior and dispersivity through randomly packed bed reactors." In: *Chemical Engineering Journal* 144.3 (2008), pages 476–482.
- [92] J.-Y. Jang and Y.-W. Chiu. "3-D Transient conjugated heat transfer and fluid flow analysis for the cooling process of sintered bed." In: *Applied Thermal Engineering* 29.14-15 (2009), pages 2895–2903.
- [93] Y. Jin and A. V. Kuznetsov. "Turbulence modeling for flows in wall bounded porous media: An analysis based on direct numerical simulations." In: *Physics of Fluids* 29.4 (2017), page 045102.
- [94] V. Jülch. "Comparison of electricity storage options using leveled cost of storage (LCOS) method." In: *Applied Energy* 183 (2016), pages 1594–1606.

- [95] M. Kaltschmitt, W. Streicher, and A. Wiese. *Erneuerbare Energien: Systemtechnik, Wirtschaftlichkeit, Umweltaspekte : mit 83 Tabellen*. 4. aktualisierte, korrigierte und ergänzte Auflage. Berlin, Heidelberg: Springer-Verlag Berlin Heidelberg, 2006.
- [96] M. M. Kenisarin. "High-temperature phase change materials for thermal energy storage." In: *Renewable and Sustainable Energy Reviews* 14.3 (2010), pages 955–970.
- [97] P. Klein, T. H. Roos, and T. J. Sheer. "Experimental Investigation into a Packed Bed Thermal Storage Solution for Solar Gas Turbine Systems." In: *Energy Procedia* 49 (2014), pages 840–849.
- [98] A. König-Haagen, S. Höhle, and D. Brüggemann. "Detailed exergetic analysis of a packed bed thermal energy storage unit in combination with an Organic Rankine Cycle." In: *Applied Thermal Engineering* 165 (2020), page 114583.
- [99] C. Kost, S. Shammugam, V. Jülch, H. Nguyen, and T. Schlegel. *Stromgestehungskosten erneuerbare Energien*. Edited by Fraunhofer ISE. 2018.
- [100] O. Krischer. *Die wissenschaftlichen Grundlagen der Trocknungstechnik*. Berlin, Heidelberg and s.l.: Springer Berlin Heidelberg, 1956.
- [101] M. Krüger, J. Haunstetter, P. Knödler, and S. Zunft. "Slag as Inventory Material for a Thermal Energy Storage (TES): Material investigation and thermo-mechanical consideration." In: *Energy Procedia* 155 (2018), pages 454–463.
- [102] H. Kruggel-Emden, S. Rickelt, S. Wirtz, and V. Scherer. "A study on the validity of the multi-sphere Discrete Element Method." In: *Powder Technology* 188.2 (2008), pages 153–165.
- [103] A. Kunwar, M. Kumar, A. Gupta, C. K. Mangrulkar, and S. Chamoli. "Experimental investigation of a packed-bed thermal energy storage system fitted with perforated cylindrical elements." In: *Heat and Mass Transfer* 55.10 (2019), pages 2723–2737.
- [104] S. Kuravi, J. Trahan, Y. Goswami, C. Jotshi, E. Stefanakos, and N. Goel. "Investigation of a High-Temperature Packed-Bed Sensible Heat Thermal Energy Storage System With Large-Sized Elements." In: *Journal of Solar Energy Engineering* 135.4 (2013).

- [105] J.-F. P. La Pitot de Beaujardiere, T. W. von Backström, and H. C.R. Reuter. "Applicability of the local thermal equilibrium assumption in the performance modelling of CSP plant rock bed thermal energy storage systems." In: *Journal of Energy Storage* 15 (2018), pages 39–56.
- [106] J.-P. Latham, A. Munjiza, X. Garcia, J. Xiang, and R. Guises. "Three-dimensional particle shape acquisition and use of shape library for DEM and FEM/DEM simulation." In: *Minerals Engineering* 21.11 (2008), pages 797–805.
- [107] J.-P. Latham, A. Munjiza, and Y. Lu. "On the prediction of void porosity and packing of rock particulates." In: *Powder Technology* 125.1 (2002), pages 10–27.
- [108] T. Laube, L. Marocco, K. Niedermeier, J. Pacio, and T. Wetzel. "Thermodynamic Analysis of High-Temperature Energy Storage Concepts Based on Liquid Metal Technology." In: *Energy Technology* 8.3 (2020), page 1900908.
- [109] H. F. Laubscher, T. W. von Backström, and F. Dinter. "Developing a cost effective rock bed thermal energy storage system: Design and modelling." In: *American Institute of Physics Conference Proceedings* 1850 (2017).
- [110] R. B. Laughlin. "Pumped thermal grid storage with heat exchange." In: *Journal of Renewable and Sustainable Energy* 9.4 (2017), page 044103.
- [111] M. J. S. de Lemos. *Turbulence in Porous Media: Modeling and Applications*. Elsevier, 2012.
- [112] M. Liu, N. H. Steven Tay, S. Bell, M. Belusko, R. Jacob, G. Will, W. Saman, and F. Bruno. "Review on concentrating solar power plants and new developments in high temperature thermal energy storage technologies." In: *Renewable and Sustainable Energy Reviews* 53 (2016), pages 1411–1432.
- [113] Lumenion. *Homepage*. 2020. URL: <https://lumenion.com/>.
- [114] S. Lupi. *Fundamentals of Electroheat*. Cham: Springer International Publishing, 2017.
- [115] I. F. Macdonald, M. S. El-Sayed, K. Mow, and F. A. L. Dullien. "Flow through Porous Media—the Ergun Equation Revisited." In: *Industrial & Engineering Chemistry Fundamentals* 18.3 (1979), pages 199–208.

- [116] C. G. Maier and K. K. Kelley. "An equation for the representation of high-temperature heat content data."  
In: *American Chemical Society Journal* 54.8 (1932), pages 3243–3246.
- [117] F. Marongiu, S. Soprani, and K. Engelbrecht.  
"Modeling of high temperature thermal energy storage in rock beds – Experimental comparison and parametric study."  
In: *Applied Thermal Engineering* 163 (2019), page 114355.
- [118] J. Marti, L. Geissbühler, V. Becattini, A. Haselbacher, and A. Steinfeld.  
"Constrained multi-objective optimization of thermocline packed-bed thermal-energy storage."  
In: *Applied Energy* 216 (2018), pages 694–708.
- [119] Mathworks. *Matlab*. 2020.  
URL: <https://de.mathworks.com/products/matlab.html>.
- [120] T. Mayyas, M. F. Ruth, B. S. Pivovar, G. Bender, and K. B. Wipke.  
*Manufacturing Cost Analysis for Proton Exchange Membrane Water Electrolyzers*. 2019.
- [121] J. D. McTigue, C. N. Markides, and A. J. White.  
"Performance response of packed-bed thermal storage to cycle duration perturbations."  
In: *Journal of Energy Storage* 19 (2018), pages 379–392.
- [122] A. Meier, C. Winkler, and D. Wuillemin.  
"Experiment for modelling high temperature rock bed storage."  
In: *Solar Energy Materials* 1991.24 (1991), pages 255–264.
- [123] M. Memmler, T. Lauf, and S. Schneider. *Emissionsbilanz erneuerbarer Energieträger: Bestimmung der vermiedenen Emissionen im Jahr 2017*. Edited by Umwelt Bundesamt. 2018.
- [124] M. Mercangöz, J. Hemrle, L. Kaufmann, A. Z'Graggen, and C. Ohler.  
"Electrothermal energy storage with transcritical CO<sub>2</sub> cycles."  
In: *Energy* 45.1 (2012), pages 407–415.
- [125] N. Mertens, F. Alobaid, L. Frigge, and B. Epple.  
"Dynamic simulation of integrated rock-bed thermocline storage for concentrated solar power." In: *Solar Energy* 110 (2014), pages 830–842.
- [126] Modelica Association. *Homepage*. 2020. URL: [modelica.org](http://modelica.org).
- [127] Modelica Association. *Modelica Standard Library Repository*. 2020.  
URL: <https://github.com/modelica/ModelicaStandardLibrary>.

- [128] R. Morgan, S. Nemes, E. Gibson, and G. Brett.  
 “Liquid air energy storage – Analysis and first results from a pilot scale demonstration plant.”  
 In: *Applied Energy* 137 (2015), pages 845–853.
- [129] A. Motlagh, H. Ahmadi, and S. H. Hashemabadi.  
 “3D CFD simulation and experimental validation of particle-to-fluid heat transfer in a randomly packed bed of cylindrical particles.”  
 In: *International Communications in Heat and Mass Transfer* 35.9 (2008), pages 1183–1189.
- [130] D. Mottaghy, H.-D. Vosteen, and R. Schellschmidt.  
 “Temperature dependence of the relationship of thermal diffusivity versus thermal conductivity for crystalline rocks.”  
 In: *International Journal of Earth Sciences* 97.2 (2008), pages 435–442.
- [131] S. M. Mousavi G, F. Faraji, A. Majazi, and K. Al-Haddad.  
 “A comprehensive review of Flywheel Energy Storage System technology.”  
 In: *Renewable and Sustainable Energy Reviews* 67 (2017), pages 477–490.
- [132] T. Nahhas, X. Py, and N. Sadiki.  
 “Experimental investigation of basalt rocks as storage material for high-temperature concentrated solar power plants.” In: *Renewable and Sustainable Energy Reviews* 110 (2019), pages 226–235.
- [133] D. A. Nield and A. Bejan. *Convection in porous media*. 4th ed. New York: Springer, 2013.
- [134] M. Nilles. *Wärmeübertragung an der Wand durchströmter Schüttungsrohre*. Volume 264. VDI Fortschrittsberichte 3. 1991.
- [135] C. Odenthal, W.-D. Steinmann, and M. Eck. “The CellFlux Storage Concept for Increased Flexibility in Sensible Heat Storage.”  
 In: *Energy Procedia* 73 (2015), pages 244–253.
- [136] C. Odenthal, W.-D. Steinmann, and S. Zunft.  
 “Analysis of a horizontal flow closed loop thermal energy storage system in pilot scale for high temperature applications – Part I: Experimental investigation of the plant.”  
 In: *Applied Energy* 263 (2020), page 114573.
- [137] N. Ohlendorf and W.-P. Schill.  
 “Frequency and duration of low-wind-power events in Germany.”  
 In: *Environmental Research Letters* 15.8 (2020), page 084045.

- [138] OpenModelica. *Homepage*. 16.03.2021.  
URL: <https://www.openmodelica.org/>.
- [139] E. Oró, A. Castell, J. Chiu, V. Martin, and L. F. Cabeza. "Stratification analysis in packed bed thermal energy storage systems." In: *Applied Energy* 109 (2013), pages 476–487.
- [140] I. Ortega–Fernández, I. Uriz, A. Ortuondo, A. B. Hernández, A. Faik, I. Loroño, and J. Rodríguez–Aseguinolaza. "Operation strategies guideline for packed bed thermal energy storage systems." In: *International Journal of Energy Research* 43.12 (2019), pages 6211–6221.
- [141] R. K. Pachauri, L. Mayer, and IPCC SYR TSU, editors. *Climate change 2014: Synthesis report*. Geneva, Switzerland: Intergovernmental Panel on Climate Change, 2015.
- [142] J. E. Pacheco, S. K. Showalter, and W. J. Kolb. "Development of a Molten-Salt Thermocline Thermal Storage System for Parabolic Trough Plants." In: *Journal of Solar Energy Engineering* 124.2 (2002), pages 153–159.
- [143] P. Pardo, A. Deydier, Z. Anxionnaz-Minvielle, S. Rougé, M. Cabassud, and P. Cognet. "A review on high temperature thermochemical heat energy storage." In: *Renewable and Sustainable Energy Reviews* 32 (2014), pages 591–610.
- [144] A. Pedersen, K. Egelbrecht, S. Sopriani, M. Wichmann, and J. Borchsenius. "High-Temperature Thermal Energy Storage for electrification and district heating." In: *1st Latin American Conference on Sustainable Development of Energy, Water and Environment Systems* (2018).
- [145] R. Pfeffer. "Heat and Mass Transport in Multiparticle Systems." In: *Industrial & Engineering Chemistry Fundamentals* 3 (1964), pages 380–383.
- [146] M. Prenzel. "Scale-up of horizontal packed bed thermal energy storage units: An in-depth experimental and numerical investigation." Dissertation. Erlangen-Nürnberg: Friedrich-Alexander-Universität, 2020.
- [147] M. Prenzel, V. Danov, S. Will, L. Zigan, T. Barmeier, and J. Schäfer. "Thermo-fluid dynamic model for horizontal packed bed thermal energy storages." In: *Energy Procedia* 135 (2017), pages 51–61.

- [148] S. A. Rackley. *Power generation fundamentals: in Carbon Capture and Storage (Second Edition)*. Elsevier, 2107.
- [149] S. Rehman, L. M. Al-Hadhrami, and Md. M. Alam. "Pumped hydro energy storage system: A technological review." In: *Renewable and Sustainable Energy Reviews* 44 (2015), pages 586–598.
- [150] W. M. Rohsenow and H. Y. Choi. "Heat, Mass and Momentum Transfer." In: *Prentice-Hall, Englewood Cliffs, NJ.* (1961).
- [151] SaltX. *Homepage*. 2020. URL: <https://saltxtechnology.com/>.
- [152] N. Sassine, F.-V. Donzé, A. Bruch, and B. Harthong. "Rock-bed thermocline storage: A numerical analysis of granular bed behavior and interaction with storage tank." In: *American Institute of Physics Conference Proceedings 1850* (2017).
- [153] D. Scharrer, B. Eppinger, P. Bazan, L. Zigan, S. Will, and R. German. "A model for triple generation of cooling, heating and electrical power with a seasonal pumped thermal energy storage." In: *Applied Energy Symposium 2020: Low carbon cities and urban energy systems* (2020).
- [154] D. Scharrer, B. Eppinger, P. Schmitt, J. Zenk, P. Bazan, J. Karl, S. Will, M. Pruckner, and R. German. "Life Cycle Assessment of a Reversible Heat Pump–Organic Rankine Cycle–Heat Storage System with Geothermal Heat Supply." In: *Energies* 13.12 (2020), page 3253.
- [155] D. Schlipf, E. Faust, G. Schneider, and H. Maier. "First operational results of a high temperature energy storage with packed bed and integration potential in CSP plants." In: *American Institute of Physics Conference Proceedings 1850* (2017), page 080024.
- [156] E. U. Schlünder. "Heat transfer to packed and stirred beds from the surface of immersed bodies." In: *Chemical Engineering and Processing* 18 (1984), pages 31–53.
- [157] O. Schmidt, S. Melchior, A. Hawkes, and I. Staffell. "Projecting the Future Levelized Cost of Electricity Storage Technologies." In: *Joule* 3.1 (2019), pages 81–100.
- [158] G. Schmitz. *Technische Thermodynamik: Grundlagen - Anwendungen - Prozesse*. 10. Auflage. 2020.

- [159] A. Shibli and J. Ford. "Damage to coal power plants due to cyclic operation." In: *Coal Power Plant Materials and Life Assessment* (2014), pages 333–357.
- [160] Siemens Gamesa Renewable Energy. *Electric Thermal Energy Storage*. URL: <https://www.siemensgamesa.com/products-and-services/hybrid-and-storage/thermal-energy-storage-with-etes>.
- [161] Siemens Gamesa Renewable Energy. *Press Release*. 16.04.2021. URL: <https://www.siemensgamesa.com/newsroom/2019/06/190612-siemens-gamesa-inauguration-energy-system-thermal>.
- [162] Siemens PLM Software. *STAR-CCM+*. URL: <http://mdx.plm.automation.siemens.com/star-ccm-plus>.
- [163] Siemens PLM Software. *STAR-CCM+ Documentation*. 2020.
- [164] S. Singh, K. Sørensen, T. Condra, S. S. Batz, and K. Kristensen. "Investigation on transient performance of a large-scale packed-bed thermal energy storage." In: *Applied Energy* 239 (2019), pages 1114–1129.
- [165] S. Solomon, G.-K. Plattner, R. Knutti, and P. Friedlingstein. "Irreversible climate change due to carbon dioxide emissions." In: *Proceeding of the National Academy of Sciences* 106 (2009), pages 1704–1709.
- [166] S. Soprani, F. Marongiu, L. Christensen, O. Alm, K. D. Petersen, T. Ulrich, and K. Engelbrecht. "Design and testing of a horizontal rock bed for high temperature thermal energy storage." In: *Applied Energy* 251 (2019), page 113345.
- [167] H. Spliethoff. *Power Generation from Solid Fuels*. Berlin, Heidelberg: Springer, 2010.
- [168] W.-D. Steinmann. "The CHEST (Compressed Heat Energy Storage) concept for facility scale thermo mechanical energy storage." In: *Energy* 69 (2014), pages 543–552.
- [169] W.-D. Steinmann. "Thermo-mechanical concepts for bulk energy storage." In: *Renewable and Sustainable Energy Reviews* 75 (2017), pages 205–219.
- [170] W.-D. Steinmann, H. Jockenhöfer, and D. Bauer. "Thermodynamic Analysis of High-Temperature Carnot Battery Concepts." In: *Energy Technology* 8.3 (2020), page 1900895.

- [171] M. Sterner and I. Stadler. *Handbook of Energy Storage*. Berlin, Heidelberg: Springer Berlin Heidelberg, 2019.
- [172] B. Stuke. "Berechnung des Wärmeaustausches in Regeneratoren mit zylindrischem und kugelförmigem Füllmaterial." In: *Angewandte Chemie* 20.10 (1948), pages 262–268.
- [173] M. V. Tabib, S. T. Johansen, and S. Amini. "A 3D CFD-DEM Methodology for Simulating Industrial Scale Packed Bed Chemical Looping Combustion Reactors." In: *Industrial and Engineering Chemistry Research* 52 (2013), pages 12041–12058.
- [174] A. Thess. "Thermodynamic efficiency of pumped heat electricity storage." In: *Physical review letters* 111 (2013), page 110602.
- [175] R. Tiskatine, R. Oaddi, R. Ait El Cadi, A. Bazgaou, L. Bouirden, A. Aharoune, and A. Ihlal. "Suitability and characteristics of rocks for sensible heat storage in CSP plants." In: *Solar Energy Materials and Solar Cells* 169 (2017), pages 245–257.
- [176] TLK-Thermo GmbH. *TIL Media Library*. 12.05.2021.  
URL: <https://www.tlk-thermo.com/index.php/de/tilmedia-suite>.
- [177] T. Tsory, N. Ben-Jacob, T. Brosh, and A. Levy. "Thermal DEM-CFD modeling and simulation of heat transfer through packed bed." In: *Powder Technology* 244 (2013), pages 52–60.
- [178] M. v.d. Heyde, L. Andresen, and G. Schmitz. "Thermodynamic Model for Heat Pump Energy Storage." In: *Proceedings of the Conference on Sustainable Energy Supply and Energy Storage Systems* (2014).
- [179] M. v.d. Heyde and G. Schmitz. *Joint Research Project Future Energy Solution: Final Report of TUHH: BMWI 03ET6072C*. TIB Hannover, 2021.
- [180] E. K. Vakkilainen. "Boiler Processes." In: *Steam generation from biomass*. Edited by Esa Kari Vakkilainen. Amsterdam, Boston, and Heidelberg: Butterworth-Heinemann an imprint of Elsevier, 2017, pages 57–86.
- [181] W. van Antwerpen, C. G. Du Toit, and P. G. Rousseau. "A review of correlations to model the packing structure and effective thermal conductivity in packed beds of mono-sized spherical particles." In: *Nuclear Engineering and Design* 240.7 (2010), pages 1803–1818.

- [182] D. Vortmeyer and R. J. Schaefer. "Equivalence of one- and two-phase models for heat transfer in packed beds: one dimensional theory." In: *Chemical Engineering Science* 29 (1974), pages 485–491.
- [183] H. Wadell. "Volume, Shape, and Roundness of Quartz Particles." In: *The Journal of Geology* 43:3 (1935), pages 250–280.
- [184] N. Wakao, S. Kaguai, and T. Funazkri. "Effect of fluid dispersion coefficients on particle to fluid heat transfer coefficients in packed beds." In: *Chemical Engineering Science* 34 (1978), pages 325–336.
- [185] N. Wakao and S. Kaguei. *Heat and Mass Transfer in Packed Beds*. University of Stellenbosch: Gordon and Breach Science Publishers, 1982.
- [186] O. Walter, A. Tremel, M. Prenzel, S. Becker, and J. Schaefer. "Techno-economic analysis of hybrid energy storage concepts via flowsheet simulations, cost modeling and energy system design." In: *Energy Conversion and Management* 218 (2020), page 112955.
- [187] L. Wang, X. Lin, L. Chai, L. Peng, D. Yu, J. Liu, and H. Chen. "Unbalanced mass flow rate of packed bed thermal energy storage and its influence on the Joule-Brayton based Pumped Thermal Electricity Storage." In: *Energy Conversion and Management* 185 (2019), pages 593–602.
- [188] S. Wang, X. Zhang, L. Yang, Y. Zhou, and J. Wang. "Experimental study of compressed air energy storage system with thermal energy storage." In: *Energy* 103 (2016), pages 182–191.
- [189] D. W. Waples and J. S. Waples. "A Review and Evaluation of Specific Heat Capacities of Rocks, Minerals, and Subsurface Fluids. Part 1: Minerals and Nonporous Rocks." In: *Natural Resources Research* 13:2 (2004), pages 97–121.
- [190] J. Weber, M. Reyers, C. Beck, M. Timme, J. G. Pinto, D. Witthaut, and B. Schäfer. "Wind Power Persistence Characterized by Superstatistics." In: *Scientific reports* 9:1 (2019), page 19971.
- [191] G. Wei, G. Wang, C. Xu, X. Ju, L. Xing, X. Du, and Y. Yang. "Selection principles and thermophysical properties of high temperature phase change materials for thermal energy storage: A review." In: *Renewable and Sustainable Energy Reviews* 81 (2018), pages 1771–1786.

- [192] S. Weitemeyer, D. Kleinhans, T. Vogt, and C. Agert.  
“Integration of Renewable Energy Sources in Future Power Systems: The Role of Storage.” In: *Renewable Energy* 75 (2015), pages 14–20.
- [193] C. Y. Wu, Y. M. Ferng, C. C. Chieng, and C. C. Liu.  
“Investigating the advantages and disadvantages of realistic approach and porous approach for closely packed pebbles in CFD simulation.” In: *Nuclear Engineering and Design* 240.5 (2010), pages 1151–1159.
- [194] B. Xu, P.-W. Li, and C. L. Chan.  
“Extending the validity of lumped capacitance method for large Biot number in thermal storage application.”  
In: *Solar Energy* 86.6 (2012), pages 1709–1724.
- [195] S. Yagi and D. Kunii.  
“Studies on effective thermal conductivities in packed beds.”  
In: *American Institute of Chemical Engineers Journal* 3 (1957), pages 373–381.
- [196] S. Yagi, D. Kunii, and N. Wakao.  
“Studies on axial effective thermal conductivities in packed beds.”  
In: *American Institute of Chemical Engineers Journal* 6 (1960), pages 543–546.
- [197] G. Zanganeh, G. Ambrosetti, A. Pedretti, S. Zavattoni, M. Barbato, P. Good, A. Haselbacher, and A. Steinfeld. “A 3 MWth parabolic trough CSP plant operating with air at up to 650 °C.” In: *International Renewable and Sustainable Energy Conference* (2014), pages 108–113.
- [198] G. Zanganeh, A. Pedretti, S. Zavattoni, M. Barbato, and A. Steinfeld.  
“Packed-bed thermal storage for concentrated solar power – Pilot-scale demonstration and industrial-scale design.”  
In: *Solar Energy* 86.10 (2012), pages 3084–3098.
- [199] S. Zavattoni, M. C. Barbato, A. Pedretti, and G. Zanganeh.  
“Evaluation of Thermal Stratification of an Air-Based Thermocline TES with Low-cost Filler Material.”  
In: *Energy Procedia* 73 (2015), pages 289–296.
- [200] P. Zehner and E. U. Schlünder.  
“Wärmeleitfähigkeit von Schüttungen bei mäßigen Temperaturen.”  
In: *Chemie Ingenieur Technik* 42.14 (1970), pages 933–941.

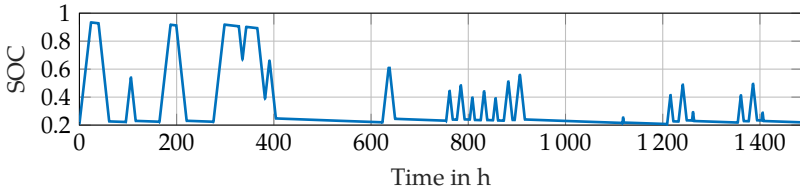
- [201] S. Zunft, M. Hänel, M. Krüger, V. Dreißigacker, F. Göhring, and E. Wahl. "Jülich Solar Power Tower—Experimental Evaluation of the Storage Subsystem and Performance Calculation." In: *Journal of Solar Energy Engineering* 133.3 (2011).

# Appendix

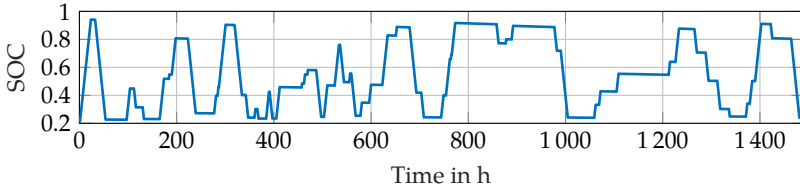
**Table A.1** / Parameters of the air cycle system simulation model, as used for the results of this work. If different, the parameters for the 5 MW- and 30 MW unit scale are shown as □/□ .

Parameter	Value
Nominal air mass flow rate	10 kg/s / 50 kg/s
Electric standby demand	50 kW / 100 kW
Packed-Bed Storage:	
Pressure loss of in- and outlet section at $T_{\text{nom,c}}$ and $\dot{m}_{\text{air,nom}}$	500 Pa
Inner insulation layer thermal conductivity	0.13 W/(m K)
Inner insulation layer density	400 kg/m <sup>3</sup>
Inner insulation layer specific heat capacity	1 kJ/(kg K)
Outer insulation layer thermal conductivity	0.39 W/(m K)
Outer insulation layer density	800 kg/m <sup>3</sup>
Outer insulation layer specific heat capacity	1 kJ/(kg K)
Heat transfer coefficient at outer surface	20 W/(m <sup>2</sup> K)
Electric Heater:	
Nominal power	5 MW / 30 MW
Efficiency	0.98
Pressure loss on air-side at $T_{\text{nom,c}}$ and $\dot{m}_{\text{air,nom}}$	500 Pa
Time constant	180 s
Fan with Motor:	
Polytropic efficiency	0.85
Mechanical efficiency	0.95

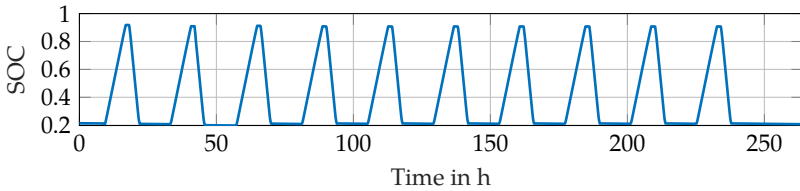
Electrical efficiency	0.9
Time constant	60 s
<hr/>	
Heat Recovery Steam Generator:	
Nominal rate of heat transfer	5 MW / 30 MW
Pinch point temperature difference	10 K
Approach point temperature difference	5 K
Pressure loss on air-side at $T_{\text{nom,c}}$ and $\dot{m}_{\text{air,nom}}$	500 Pa
Max. allowed air inlet temperature	600 °C
Max. allowed air inlet temperature gradient	10 K/min
<hr/>	
High-temperature piping:	
Overall length	30 m / 60 m
Diameter	1 m / 1.5 m
Number of parallel pipes	1 / 4
Insulation thickness	0.4 m / 0.6 m
Thermal conductivity of insulation material	0.05 W/(m K)
<hr/>	
Low-temperature piping:	
Overall length	90 m / 160 m
Diameter	1.5 m
Number of parallel pipes	1 / 2
Insulation thickness	0.2 m
Thermal conductivity of insulation material	0.05 W/(m K)
<hr/>	



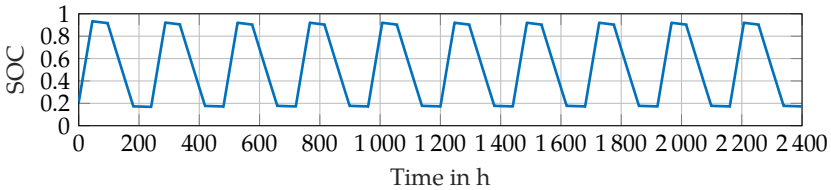
**a** / Schedule based on residual load time series data.



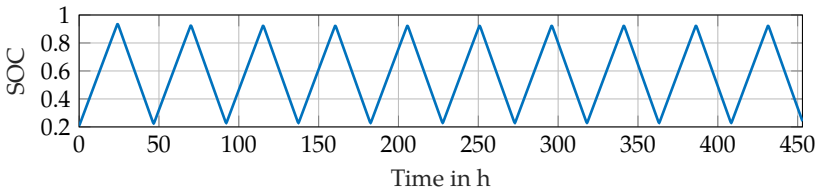
**b** / Schedule based on wholesale electricity price time series data.



**c** / Solar-based operational schedule according to the *California Duck Curve*.



**d** / Wind-based operational schedule.



**e** / Cyclic full charge and discharge operation.

**Figure A.1** / Packed-bed storage state of charge resulting from the five tested operational schedules according to Section 6.1 in power-to-power operation.



# Curriculum Vitae

## Personal Data

Name Michael von der Heyde  
Birth 28. Januar 1986 in Kiel

## Work Experience

since 06/21 Development Engineer at Siemens Gamesa Renewable Energy  
11/15 – 04/21 Scientific Associate at Institute of Engineering Thermodynamics at Hamburg University of Technology (TUHH)  
08/14 – 10/15 Scientific Associate at Institute of Electric Power Systems and Automation at TUHH

## University Education

10/11 – 07/14 M.Sc. in Theoretical Mechanical Engineering at TUHH  
08/12 – 02/13 Semester at the University of California at Berkeley  
09/08 – 09/11 B.Sc. in Mechanical Engineering at TUHH

## Professional Training

07/05 – 01/08 Ship Mechanic at Hapag-Lloyd Container Line

## School Education

06/96 – 06/05 Theodor Heuss Schule, Pinneberg